Title
Developmental origins of heterogeneity in melanocytes and implications for melanoma

Author
Samuel, Ryan Matthew

Publication Date
2023

Peer reviewed|Thesis/dissertation

Developmental origins of heterogeneity in melanocytes and implications for melanoma

by
Ryan Samuel

DISSERTATION
Submitted in partial satisfaction of the requirements for degree of
DOCTOR OF PHILOSOPHY

in

Developmental and Stem Cell Biology

in the

GRADUATE DIVISION
of the
UNIVERSITY OF CALIFORNIA, SAN FRANCISCO

Approved:

DocuSigned by:
Licia Selleri
C310C42C7D294CB...

Licia Selleri
Chair

DocuSigned by:
Faranak Fattahi
D7C8B...

Faranak Fattahi

DocuSigned by:
Jeffrey Bush
B0C6B...

Jeffrey Bush

DocuSigned by:
Hani Goodarzi
B0D4B...

Hani Goodarzi

DocuSigned by:
Alex Pollen
2102D531BF2D416...

Alex Pollen
Committee Members

Dedication

I dedicate this dissertation to my parents, Marianne E. and Steven P. Samuel, who unsuspectingly brought their second child into the world with a neurocristopathy. I'm sure it did not seem like it during the hospital visits, the colostomy bag changes, or while pleading with me to take Kondremul, but Hirschsprung's disease was a blessing in disguise to which I attribute my passion for science, development, genetics, and the neural crest. Words cannot express how lucky I was then and how thankful I am now to have you as my parents.

Acknowledgments

First, I would like to thank my Ph.D. advisor, Dr. Faranak Fattahi. In a lab built for drug discovery, you let me pursue my basic development-focused passion projects with uncompromising support. Your enthusiasm for the science, empathy for the Ph.D. process, and relentless confidence fostered an environment which made a challenging journey much easier. I couldn't have asked for a better professional and personal mentor.

Thank you to the entire Fattahi lab, which has nearly tripled in size since I first joined in 2018. It is an honor to be part of such a welcoming and caring lab family which supports not only the science we all are doing but everyone's well-being first and foremost. A special thank you to Dr. Mikayla Richter, my lab Ph.D. buddy from whom I learned most everything about graduate school (including how to write a thesis and graduate) by watching her do it first.

I would also like to acknowledge my thesis committee members. Thank you Dr. Licia Selleri for serving as my committee chair, for your breadth of knowledge of the neural crest field, and for your constant words of support and affirmation. Thank you Dr. Jeff Bush for serving not only as a committee member but also as my secondary mentor. Your thoughtful questions during our meetings always guided and focused my research in new and exciting directions. Thank you Dr. Alex Pollen for serving both as a thesis committee member and as my qualifying exam committee chair. Your experience and expertise in the stem cell field guided me through one of the more difficult moments in my graduate career. Thank you to Dr. Hani Goodarzi for being both a thesis committee member and a

close collaborator. Your willingness to share your lab's space and knowledge to teach me new techniques as well as acting as a sounding board for my bioinformatics ideas and training were instrumental in my and my project's success.

I want to thank both the Developmental and Stem Cell Biology program and the student cohort. It is amazing to see how dramatically the program has changed over the course of my graduate training thanks to the program's commitment to its students, effort to listen to student feedback, and willingness to implement meaningful change. To the DSCB students in my cohort, I am so thankful to have been a part of such a diverse and welcoming group; I could not have made it through the first two years without everyone's support. To the entire DSCB student body, I can't imagine this experience without the friendships I found within the program. Thank you for constantly normalizing and validating my graduate experience and helping me to have some fun during the process.

I would like to acknowledge my family and the families I have gained during this experience. To my mom, dad, brother, nephew, grandparents, aunts, uncles and cousins, thank you for everything you all have done to help me along this lifelong journey and for always showing interest in my research, even if you had no clue what I was talking about. To my in-laws, Dorothy, John, and Allie Gaylord, thank you for the frequent visits and for unconditionally loving and supporting me as if I were your own. To my "adopted" family, Linda and Vince Foecke, thank you for opening up your home to me, for feeding me a homecooked meal pretty much every single week, and for providing a loving family environment during my time apart from my own family. To my best friends, Mariko Foecke

and Alex Duncan, thank you for being there for me during some of the most difficult times of this journey, and especially for letting me third wheel on all the ski trips.

I would like to thank my cat, Rosebud, for being a constant source of joy and companionship during both my undergraduate and graduate careers. Thank you for accepting me as your companion, and, despite going blind, for always finding your way into my lap.

Last, but not least, I thank my wife, Eliza Gaylord. To fully thank you for all the ways that you have helped me would require as many pages as this thesis. Thank you for packing up your life and moving across the country with me to let me pursue my passions. You helped me celebrate my successes, shrug off some failures, and had my back no matter what this life has thrown at me. I truly could not have made it through these last five years without you. I am so grateful to have you as my wife and cannot wait to take on the future with you.

Contributions

Chapter 2 of this dissertation contains material under review at a peer-reviewed journal. Therefore, the content here may differ from the final published form. Albertas Navickas, PhD assisted and supervised the generation of all melanoma CRISPR interference lines, generation of the CRISPR guide RNA library, the *in vivo* CRISPR interference screen and performed bulk RNA sequencing library preparations. Ashley Maynard performed 10X library preparations for single cell RNA sequencing and assisted with single cell RNA sequencing data processing and analysis. Eliza Gaylord performed dissection, sectioning, immunofluorescent staining and imaging of mouse embryos. Kristle Garcia performed injections for mouse experiments, assisted with luciferase imaging of CRISPR interference screen, and performed mouse tissue collection and processing. Homa Majd, PhD and Mikayla Richter, PhD assisted with *in vitro* sample collection. Nicholas Elder assisted with figure generation and design. Daniel Le assisted with single cell RNA sequencing data processing and analysis. Phi Nguyen assisted with the *in vitro* arm of CRIPSR interference screen, assisted with CRISPR interference line validation. Bradley Shibata performed transmission electron microscopy sample preparation and supervised transmission electron microscopy imaging. Marta Losa Llabata, PhD performed mouse husbandry, breeding, and embryo collection. Licia Selleri, PhD supervised mouse husbandry, breeding, and embryo collection. Diana Laird, PhD supervised mouse embryonic tissue staining and imaging. Spyros Darmanis, PhD supervised 10X single cell RNA sequencing sample collection and sequencing. Hani Goodarzi supervised all CRISPRi experiments, supervised and performed mouse injections, and performed bulk RNA sequencing spliceoform analysis.

Developmental origins of heterogeneity in melanocytes and implications for melanoma

Ryan M. Samuel

Abstract

Owing to advances in single cell and omics level profiling methodologies, nuances of cell identity and characterization of novel sub populations has become an active research area for many tissues and organs. However, utilization of these techniques for similar discoveries in the neural crest field have been limited due to technical challenges associated with collecting a transient and highly migratory cell type. Recent advances in human pluripotent stem cell models of neural crest differentiation, allowing for spatial and temporal patterning of neural crest identity, offer an attractive alternative due to their reproducibility, scalability, and availability. Utilization of these systems for omics level experiments with subsequent validation in *in vivo* models offers a novel approach for advancing the understanding of neural crest identity and fate competency.

This dissertation begins with a history and overview of the works describing neural crest development, identity, and potency, eventually focusing on the melanocyte lineage and how neural crest heterogeneity presents in melanoma. Applications for stem cell-based models to advance these areas of research are also discussed. Stemming from these points, I utilize a stem cell-based model of temporal neural crest patterning to characterize

the heterogeneity among temporally distinct neural crest populations and focus in on how temporal patterning affects the melanocyte lineage and melanoma.

To characterize heterogeneity, I employ single cell RNA sequencing with comprehensive downstream expression and lineage analysis to reveal temporally and transcriptionally distinct trajectories of melanocyte specification. I develop a new protocol to differentiate melanocytes from human pluripotent stem cell-derived Schwann cell precursors to perform the first functional and transcriptional comparison of melanocytes derived from temporally distinct progenitor populations. Finally, I leverage data from the cancer genome atlas and an *in vivo* CRISPR interference screen to reveal that melanoma cases with transcriptional signatures similar to Schwann cell precursor-derived melanocytes display higher rates of metastasis.

Altogether, this work identifies a temporal switch in melanocyte sub population competency in human neural crest cells and systematically characterizes this developmental origin of heterogeneity in melanocyte populations and melanoma. Moreover, it highlights the utility of stem cell-based models of neural crest patterning for novel discovery and lays a framework for future complementary analysis focusing on additional aspects of neural crest spatiotemporal identity or other neural crest lineages.

Table of Contents

List of Figures

List of Tables

List of Abbreviations

ACE2: angiotensin converting enzyme 2

AM: Acral melanoma

BAP1: ubiquitin carboxyl-terminal hydrolase

BMP: bone morphogenic protein

cAMP: cyclic AMP

CCND1: cyclin D1

CDK4: cyclin dependent kinase 4

CDKN2A: cyclin dependent kinase inhibitor 2A

CM: Cutaneous melanoma

CNS: central nervous system

CRISPRi: CRISPR interference

dCT: adaptively-thresholded low rank approximation

dCT: delta CT

dCT: Delta delta CT

DCT: dopachrome tautomerase

DHH: desert hedgehog

ECAD: epithelial-cadherin

EDN3: endothelin 3

EDNRB: endothelin receptor type B

ERBB3: Erb-b2 receptor tyrosine kinase 3

FACS: fluorescence activated cell sorting

FGF: fibroblast growth factor

FOXD3: forkhead box D3

FUCCI: fluorescent ubiquination-based cell cycle indicator

GFD11: growth differentiation factor 11

GNA11: guanine nucleotide-binding protein subunit alpha-11

GNAQ: guanine nucleotide-binding protein G(q)

gRNA: guide RNA

GSEA: gene set enrichment analysis

HOX: homeobox

HOX: Schwann Cell Precursor

hPSC: human pluripotent stem cell

IGF: insulin-like growth factor

LRP: Ligand-receptor pair

LRP: mutual nearest neighbors

MAPK: mitogen-activated protein kinase

MEK: mitogen-activated protein kinase kinase

MIM: melanocyte induction media

MITF: MicropthalmiaMicrophthalmia-associated transcription factor

MLANA: melan-A

MM: Mucosal melanoma

MPM: melanocyte priming media

NC-C: neural crest maintenance media

NC: neural crest

NCC: neural crest cell

NF1: neurofibromatosis type 1

NMF: nonnegative matrix factorization

NNE: non-neural ectoderm

NSG: NOD scid gamma

PAK1: p21-activating kinase

PAX3: paired box gene 3

PCA: Principal component analysis

PDGF: platelet-derived growth factor

PI: propidium iodide

PI3K/AKT: phosphatidylinositol 3-kinase and protein kinase B

PLP1: proteolipid protein 1

PMEL: premelanosome protein

PO: poly-L-ornithine

PTEN: phosphatase and TENsin homolog

RA: and retinoic acid

ROI: region of interest

S1-S5: stages 1-5

SC: Schwann Cells

SCENIC: single-cell regulatory network inference and clustering

SCM: Schwann Cell Medium

SCPDs: SCP derivatives

scRNAseq: single cell RNA sequencing

sNN: Shared nearest-neighbor

SOX10: SRY-Box transcription factor 10

SOX2: SRY-Box transcription factor 2

STK11: serine/threonine kinase 11

SWNE: similarity weighted non-negative embedding

T1: trajectory 1

T1P1: Path 1 of T1 differentiation

T1P2: Path 2 of T1 differentiation

T2: trajectory 2

T2P1: Path 1 of T2 differentiation

T2P2: Path 2 of T2 differentiation

TCGA: the cancer genome atlas

TEM: transmission electron microscopy

TERT: telomerase reverse transcriptase

TFs: transcription factors

TWT: triple wild-type

TYR: tyrosinase

TYRP1: tyrosinase-related protein 1

UMAP: Uniform manifold approximation and projection

UV: Ultraviolet

UV: Uveal melanoma

WNT: wingless/integrated

Chapter 1 Stem cell-based models for studying neural crest fate decisions, competency, and fate restriction

1.1 Introduction

The neural crest (NC) is a transient fetal cell population and is the source of tissues as diverse as neurons and bone. To date, studies of NC potency and fate decision have primarily been performed in vertebrate animal models such as mice, chick, frog, and zebrafish embryos. These studies provided the field with fundamental insights such as mapping out the core gene regulatory network essential for NC multipotency and identifying patterns of fate commitment by NC cells (NCC) during normal embryonic development. However, the studies performed in animal models have generated conflicting results when attempting to assess NC potency and generate models of NC fate decision. For example, some results indicate a NCC follows a branching fate decision tree, where the cell incrementally becomes restricted through a series of binary decisions. However, new evidence suggests a cyclical fate determination model, where all fates are accessible to the cell, but certain fates are more probable at different points in the cycle. These diverging results are largely due to the technical challenges inherent to studying a cell population that is highly migratory and diffuse throughout the developing embryo, especially when using modern omics techniques. To address these limitations, there is a need for a robust, scalable, reductionistic and easily manipulatable model of NC development and differentiation. Here, human pluripotent stem cell (hPSC) directed

differentiations are examined as tractable models for facilitating novel discoveries in NC development and potency.

1.2 Cell fate decisions in neural crest development

The NC is a vertebrate specific cell population specified along the entire anteroposterior border between the developing non-neural ectoderm and neural plate[1]. Upon neural plate invagination and subsequent neural tube closure, NCCs undergo an epithelial to mesenchymal transition to delaminate from the dorsal neural tube. Once delaminated, the NCCs will then migrate extensively throughout the developing embryonic tissue, ultimately colonizing many different organs and differentiating into a diverse array of specialized cell types.

As with all tissues, the proper development of NC lineages is orchestrated by a complex interplay between cell-extrinsic and cell-intrinsic determinants. For instance, NCCs located in different regions of the body will be exposed to unique chemokines and growth factors that will differentially influence migration patterns and lineage determinations. However, NCCs in the same region may differentially express receptors for these signals allowing NCCs to be differentially responsive to the same growth factors or chemokines. Thus, during normal development, the unique spatiotemporal identity ultimately determines the lineal fate of each NCC.

Efforts to generate a fate map for the NC are more than 100 years in the making. Early experimental embryologists, primarily utilizing amphibian models, used techniques such as dye labeling, cell ablation and grafting to determine which NC populations gave rise to certain tissues or cell types. Newer cellular labeling techniques, including dye microinjections, transgenic mouse lines, CRISPR and single cell RNA sequencing (snRNAseq), have allowed for the tracking of individual NCCs. These new techniques validated the findings of early experiments while allowing for finer resolution tracing of NC migration, proliferation, and lineage potential at the single cell level. Altogether, these experiments have generated a fate map that revealed differences in fate acquisition based on the axial identity and delamination/migration time of a NCC.

1.2.1 Axial Patterning

Anteroposterior patterning of vertebrate embryos coincides with gastrulation and neurulation. These patterning events are orchestrated by overlapping gradients of wingless/integrated (WNT), bone morphogenic protein (BMP), fibroblast growth factor (FGF), and retinoic acid (RA) signaling agonists and antagonists[2,3]. These signaling events play numerous roles such as WNT and FGF coordinating axial elongation at the posterior end of the embryo while the intersecting RA promotes somite formation and segmentation[4,5]. The competing RA and WNT/FGF gradients also initiate and coordinate the expression of homeobox (HOX) transcription factors[6–8]. Paralogous groups from a total of 39 different mammalian HOX genes are expressed in tightly regulated anterior to posterior domains to induce axial level specific gene expression that is critical for proper

development[9]. These signaling gradients similarly affect the developing NC populations resulting in four axially distinct sub populations: cranial, vagal, trunk and sacral[10].

The cranial NC spans from the most anterior forebrain region to the sixth rhombomere of the hindbrain and lacks HOX gene expression due to the presence of RA antagonists released by the forebrain[11]. Fate mapping in the cranial NC is further subdivided based on anteroposterior positioning within the cranial region[12,13]. NCCs delaminating from the forebrain and midbrain regions migrate dorsolaterally and anteriorly to form bone and cartilage in the developing fronto-nasal structures[14,15]. In the hindbrain region, which is segmented into seven rhombomeres, NCCs migrate laterally and ventrally in three streams adjacent to the rhombomeres to reach the three pharyngeal arches[13,16–18]. The first stream is comprised of NCCS from the midbrain and rhombomeres one and two and colonizes pharyngeal arch one to give rise to the malleus and incus bones of the inner ear as well as bones in the jaw. The second stream at rhombomere four is destined for pharyngeal arch two to produce the hyoid and stapes bones in the ear. Finally, the third stream from rhombomeres six and seven migrates to pharyngeal arch three to contribute specialized cell types to the thyroid and parathyroid glands. Along with differentiating into cranial bone and cartilage, these hindbrain NCCs also give rise to cranial and jugular sensory, and autonomic parasympathetic neurons and glia as well as epidermal melanocytes[19].

The vagal NC is located posteriorly to the hindbrain from somites one to seven and expresses HOX gene homologs one through four[6,20]. Vagal crest cells that migrate

dorsolaterally along somites one to three contribute smooth muscle cells to the heart, outflow tract, great vessels and pharyngeal aches three to six[21–23]. NCCs arising from this same location also differentiate into melanocytes[24]. The vagal NCCs that migrate ventrally from somites one to three, as well as from somites four to six, invade the developing foregut[25]. Once in the gut, these NCCs undergo extensive migration, proliferation and differentiation to give rise to the enteric neurons and glia throughout the entire gastrointestinal tract[26]. A subset of the ventrally migrating vagal NC from somites one to two also give rise to parasympathetic ganglia[20]. The vagal NCCs adjacent to somite seven form melanocytes and the most anterior sensory neuron dorsal root ganglion[27].

The trunk NC spans a large region from somites eight to twenty-eight and expresses HOX gene homologs five through eleven[9,16]. Fate determination in the trunk is demarcated by which of the three main migration pathways a NCC takes[28–31]. Ventrally migrating trunk NC give rise to the sensory dorsal root ganglia and autonomic sympathetic neuron chains[32,33]. Trunk NCCs taking a ventral path also differentiate into non neuronal derivatives such as glia, endoneurial fibroblasts, and chromaffin cells in developing adrenal glands[32]. Finally, dorsolaterally migrating trunk NCCs contribute to the epidermal melanocyte population in the trunk[27,34].

The most posterior crest, the sacral NC, are positioned at somites twenty-nine and beyond and express HOX gene homologs twelve and thirteen[9,33]. Sacral NCCs primarily give rise to enteric neuronal lineages[25,35]. While vagal NCCs migrating through the gastrointestinal tract reach the hindgut and form enteric neurons, sacral NCCs directly

invade the hindgut to contribute to the enteric neuron population[36]. Mounting evidence suggests that the enteric neurons derived from vagal and sacral NCCs are unique, noninterchangeable neuronal populations[35,37].

Overall, the axial location of a NCC plays a critical role in the fate determination of the cell. Signaling cues guide different NC populations along diverse migration paths to generate specialized cell types unique to each anatomical location, such as craniofacial bone and cartilage, cardiac and enteric derivatives, and sympathoadrenal cell types[19,21,22,25,26,32,35]. While these lineages are uniquely derived from different NC populations, other mature lineages that exist throughout the body are derived from multiple axial populations, such as sensory and autonomic neurons and melanocytes[24,27,34]. However, as recently demonstrated by the differing vagal and sacral enteric neuron populations, profiling of similar derivative cell types from different axial NC populations will be necessary to determine how anatomical location and progenitor identity affects mature cell identity[37].

1.2.2 Temporal Patterning

The process of NC delamination and migration initiation occurs over roughly two days in mice and around 4 days in humans[38,39]. Over the course of the delamination event, the developing embryo undergoes dramatic changes such that, even at the same axial position, the first migrating NCC and the last migrating NCC enter unique environments.

Together with taking different migration pathways, this continuum of delamination and migration allows NCCs from the same axial region to give rise to diverse cell types.

Broadly categorized as either early migratory or late migratory NCCs, delamination timing dictates lineage commitment throughout the developing NC populations. For example, in the cranial region, the earliest migrating NCCs traverse long distances to colonize the fronto-nasal region and pharyngeal arches and generate much of the craniofacial bone and cartilage[14,40]. Later migratory cranial NC, however, settle close to the neural tube to give rise to the cranial sensory and autonomic ganglia[18,40]. Similarly, early migratory anterior vagal NC contributes to cardiac tissue, while later migratory NC from the same region give rise to parasympathetic ganglia[21,22,41].

Initial development of the peripheral nervous system, in part by earlier migrating NC, is crucial for the development of later migrating NC derivatives. Observed in all axial populations, late NCCs delaminate and associate with nerve fibers close to the neural tube[42]. Upon becoming nerve-associated, these late NCCs adopt a new identity known as a Schwann Cell Precursor (SCP). SCPs can form directly, when a NCC adheres to an axon and begins to migrate, or indirectly, if a NCC first becomes a boundary cap cell[43]. Boundary cap cells are NC derived cells that cluster on the neural tube around the future entry/exit points of motor and sensory neurons of the central nervous system and function to prevent neuronal cell bodies from detaching from the neural tube during axon extension[44–46]. Boundary cap cells can then transition into SCPs and migrate along the nerve fibers[47].

SCPs are so named because Schwann Cells (SC), the myelinating or non-myelinating glial cells of the peripheral nervous system, were initially believed to be the sole derivative of SCPs[42,48,49]. Just in the last two decades, however, lineage tracing of SCPs has revealed that SCPs are not just a precursor to a single lineage. Instead, SCPs represent a still multipotent, NC-like progenitor population[50]. These progenitors maintain expression of the core NC gene regulatory network but adopt a unique transcriptional identity upon nerve association, allowing SCPs to be distinguished from migratory crest[51]. This NC intermediate cell type is thus defined by nerve association, which imparts a unique transcriptional identity and facilitates migration to target tissues to give rise to diverse derivatives.

The first indication of this multipotency was observed in sciatic ganglia when tracing of SCPs revealed a substantial contribution to the endoneurial fibroblast population, a cell population that serves as structural support within a ganglion[52]. Next, SCPs were found to contribute to the melanocyte population. Historically, melanocytes were understood to be a derivative of early migratory crest cells, derived from the NCCs following a dorsolateral migration route at most axial positions in the embryo[53]. However, tracing of SCPs revealed SCP-derived melanocytes in the limbs as well as in the dorsal and lateral body walls[54]. Similarly, the adrenal chromaffin cells were originally thought to be derived directly from early migratory NC[55]. Tracing of SCPs into the adrenal gland, however, revealed that 80% of chromaffin cells are derived from later migrating SCPs[56]. It has also been demonstrated that SCPs maintain broad neurogenic potential. Cranial and vagal

SCPs have been shown to be the progenitor for parasympathetic neurons, while SCPs in the trunk have been shown to invade the gastrointestinal tract to contribute to enteric neurons in both the mucosal and muscle layers[57–59]. Most recently, it has been shown that SCPs also contribute to mesenchymal derivatives. Cranial SCPs have been traced into cranial cartilage as well as into the dental pulp and odontoblast layers of mouse incisors[60,61]. Surprisingly, SCPs in the trunk have also been observed to contribute to cartilage and bone in the scapula and ribs, tissues originally believed to be solely mesoderm derived[60,62].

Most recently, scRNAseq has been used to extensively profile SCPs and their differentiation towards discrete lineages. The integration of cells of the NC lineage from multiple embryonic ages and tissue types revealed a transition of cranial and trunk NCCs into a common differentiation “hub” state[51]. Despite sharing the expression of many marker genes, this hub state appears to be comprised of sub populations of SCPs which group partially based on the tissue origin of the SCP. Enteric SCPs group together and are inferred to only give rise to enteric neurons and glia[51]. Sympathoadrenal SCP form another group which is inferred to give rise to chromaffin cells[51]. A third group, which is inferred to give rise to diverse glial derivatives, is comprised of SCPs from the limbs and trunk as well as enteric and sympathoadrenal SCPs[51].

These experiments have set the groundwork for a still ongoing paradigm shift in NC development research as new technologies continue to facilitate the generation of an increasingly high-resolution NC fate map. Already, these methods have rewritten the

identity of a temporally distinct NC cell type once believed to be a precursor to only glial lineages[43,50,63,64]. As insight into the temporal nuances of NC development continue to be uncovered, it will be of particular importance to discern how the axial and temporal components of NC patterning intersect and give rise to sub populations of NC and SCPs. Identification and characterization of these NC sub populations will require systematic profiling of the transcriptomic and epigenomic aspects of cell identity. Importantly, as more cell types are revealed to be derivates of both axially and/or temporally distinct progenitor populations, it will be imperative to elucidate how the identity of spatially or temporally distinct progenitors affect the identity of the derivative cell type.

1.3 Competency and fate restriction in the neural crest (The Great Fate Debate)

Parallel to the efforts of generating a map of NC fate has been the construction of a related, but fundamentally different, map of NC potency. Numerous lineage tracing experiments have systematically described the fates acquired by NCCs of different spatiotemporal identity during normal development[65]. These experiments generated two important observations. First, a similar cell population could generate a plethora of cell types throughout the embryo. Second, while some cell types, such as melanocytes, were derived from neural crest of all spatiotemporal identities, other cell types, such as adrenal chromaffin cells, were only derived from singular spatiotemporal identities[24,27,34,55,56]. These observations could potentially be explained by two entirely different models reliant solely on cell-intrinsic or cell-extrinsic determinants. At the single cell level, the NC population could be comprised of pre-committed precursors, cell-intrinsically

predetermined to give rise to a single cell type from the moment of specification. Alternatively, each NCC could possess the potential to differentiate into any NC derivative, but extrinsic factors unique to the environment of each cell instructs differentiation towards different lineages.

Assessing the potency of a NCC to validate one of these models requires the manipulation of normal development, thus testing the capability of a NCC to give rise to cell types outside of what is typically observed. Ultimately, potency can only ever be determined at the population level as multiple experiments are required to test differentiation potential towards all lineages. Specifically, as it is not currently possible to perform repeated differentiation experiments on a single NCC, potency can only be a prediction based on the results of separate experiments performed on similar NC populations. However, in a cell type and developmental process as dynamic as the NC, competency is likely linked to the exact spatiotemporal identity of a cell.

For example, a cell that is multipotent at the instance of delamination will quickly begin to respond to extracellular signals. These signals may instruct the cell down a particular migratory pathway while simultaneously inducing changes in gene expression to begin lineage specification. While this process is essential for reinforcing cellular behavior and ensuring robust differentiation, tissue formation, and successful development of the embryo, it has confounded the results of NC competency experiments. Typically, as a cell responds to growth factors and becomes more differentiated, competency is reduced as the fate of that cell becomes restricted towards a particular lineage. However, the point

during differentiation at which competency for other lineages is lost has been technically challenging to decipher using *in vivo* models. This necessity, marred by technical ability, to perform parallel potency experiments on spatiotemporally identical NC populations has generated conflicting results surrounding NC potency and fate restriction models. Here, the history and current status of these results and models will be discussed.

The very first experiments to address NC potency quickly disproved both aforementioned models. *In vitro* clonal culture and differentiation of quail NCCs resulted in both homogenous and heterogenous progeny populations, where some clones differentiated into either melanocytes or neurons while other clones gave rise to both[66–68]. These results, instead, supported a combinatorial third model where the NC is comprised of heterogenous sub population with differing potency. Indeed, the results of subsequent clonogenic culture experiments supported and expanded this model by testing other axial identities and adding lineage specific growth factors to influence differentiation[69–75]. With this model, the fate acquisition of a NCC would be dependent on a combination of cell-intrinsic and cell-extrinsic factors.

To understand if the spatial identity of a NC population alters the potency of that population, researchers utilized heterochronic quail to chicken grafting experiments. Grafts from the dorsal neural tube area of quail embryos were dissected from specific axial locations and were transplanted into chicken embryos at differing axial positions. Transplanting cranial NC into the trunk revealed the formation of trunk specific derivatives such as sympathetic neurons and adrenal chromaffin cells from the cranial NCCs[76].

Despite this observed potency at the population level, these experiments also revealed fate restriction in a cranial sub population as ectopic cartilage was produced, suggesting these cells were pre-committed to a mesenchymal lineage[18,76,77]. Converse experiments placing trunk NC in the cranial region showed the ability to contribute to cranial neurons, glia, connective tissue and pericytes, but no contribution to cartilage or bone[78–80]. Similar results were observed when transplanting cardiac NC in the cranium, suggesting the potential to produce mesenchymal derivatives was unique to the cranial NC population[80]. This axial level specific potency was also observed for the vagal NC. Transplantation of cranial or trunk NC into the vagal region failed to produce the necessary cardiac derivatives[81]. However, plasticity does exist within the vagal region, as swapping the anterior and posterior vagal NC resulted in normal cardiac and enteric development[81].

Similar heterochronic quail-chick grafts were preformed to investigate how delamination and migration time affect NC potency. Grafts from the dorsal neural tube area of quail embryos were dissected from specific developmental time windows and were transplanted into chicken embryos at the corresponding axial level but of differing developmental age. In the cranial region, transplantation of early migratory NC into later stage recipient embryos, and vice versa, revealed that the cranial NC maintain potency throughout delamination and migration and can give rise to all derivatives of the complementary migratory staged population[40]. This data alone would suggest that cranial NCCs maintain a high potency and rely heavily on environmental signals to dictate lineage specification. However, the transplantation of these cells back into an environment where chondrogenic specification is expected masks the observation of

unipotent chondrogenic precursors that was observed when cranial NC was transplanted into the trunk. Interestingly, potency was not conserved across temporally distinct trunk NC populations as late migratory trunk NC was unable to give rise to adrenergic chromaffin cells when placed in a younger recipient embryo[32].

While these grafting experiments provided considerable insight into the potency of NC populations, the nature of these experiments were biased towards positive results. Researchers were only able to observe contributions to lineages for which they labeled, and cells that may have migrated to inappropriate locations were missed. Additionally, cells that may have undergone apoptosis due to a complete inability to adapt to a new environment could not be accounted for with these techniques. To address some of these limitations, methods were developed to label and follow a single NCC as it differentiates.

Microinjections of vital dyes into individual pre-migratory or migratory NCCs facilitated the first *in vivo* clonal lineage analysis. Labeling pre-migratory NCCs in the dorsal neural tube at varying stages of development showed that lineage contribution varied over time[17,34,82–85]. Similar experiments repeated with more modern techniques showed similar results and prompted researchers to claim that pre-migratory NCCs were fate restricted prior to migration[86]. However, tracing of migratory NC populations using a variety of old and new techniques have demonstrated the competency of a single NCC to give rise to multiple daughter cells of different lineages[87–91]. These same experiments do, however, provide evidence for sub populations of lineage restricted NC that only give rise to daughter cells of a single lineage[87–91].

Taken all together, researchers have proposed differing models for NC lineage restriction and commitment due to the presence of unipotent and multipotent NC sub populations. One possibility is direct fate restriction, where a multipotent NCC directly converts to a committed precursor for a single lineage. However, many scRNAseq experiments support a model of sequential fate bifurcations[51,92–94]. In this model, a multipotent NC progenitor activates transcription of two conflicting fate specification gene networks. These two transcriptional networks compete intrinsically in the cell until the expression of one network overpowers the other, perhaps biased by external cues reinforcing the expression of the network. The transcription of the other network subsequently turns off as the progenitor cells commits toward the winning lineage. These bifurcations are predicted to happen progressively to incrementally restrict a progenitor toward a single lineage. Most recently, a novel cyclical fate restriction model has been proposed which seeks to account for the observation of potent and restricted NCCs[95]. In this model, multipotent neural crest cells maintain a low basal expression of all lineage specification programs but cycle asynchronously through sub-states when one of the fate programs is more highly expressed. Subsequent fate specification from this cycle would be dependent on the time a cell spends in a sub-state which can be influenced by exogenous signals.

Resolution of these models will require additional experiments and potentially the development of new technologies. Nanostring sequencing of purified NCCs can provide insight into the expression of lowly expressed fate modules[96]. However, validation of such a cycling event *in vivo* will require the development of a fluorescent reporter system for

these fate modules reminiscent of the fluorescent ubiquination-based cell cycle indicator (FUCCI) reporter system for cell cycle stage[97]. Additionally, readouts of fate restriction may need to be expanded beyond the expression of fate specific transcription factors to include receptors of migratory cues. For example, NCCs of the same spatiotemporal population may lack heterogeneity in the expression of fate modules but could differentially express receptors that prompt subpopulations of NCCs to follow different migration paths. In this way, the cells have not begun to differentiate, but the unique migration paths have altered the differentiation signals these cells will ultimately receive.

1.4 Development and disease of the melanocyte lineage

Ultraviolet (UV) radiation is a potent mutagen emitted by the sun and poses serious health risks by causing DNA damage in the skin[98]. Melanin is a macromolecule synthesized from tyrosine which functions to absorb UV radiation and protect against UV-induced DNA damage[99]. In vertebrates, melanin is synthesized by melanocytes, a highly specialized population of NC-derived cells. In mammals, mature melanocytes reside in the skin epidermis and hair follicles[100]. Melanocytes synthesize melanin inside specialized organelles called melanosomes which are transferred to the surrounding epidermal or cortical keratinocytes of the skin or hair bulb, respectively[100].

The proper development of melanocytes is a complex process of simultaneous migration and differentiation. Additionally, the function of mature melanocytes is reliant on the expression of many genes unique to the melanocyte lineage. This complexity and

specialization mean that there are many opportunities for melanocyte development and function to go awry. As such there are over 100 human disorders which affect melanocytes or pigmentation[101]. Additionally, even if the melanocyte population develops and functions normally, melanin absorption of UV radiation is not 100% efficient which puts melanocytes at high risk for oncogenic transformation[101]. Here, the status of melanocyte development research and diseases affecting the melanocyte lineage will be discussed.

1.4.1 Development

There have been two pivotal experiments which defined new eras of melanocyte development research. In the late 1800's, skin transplantation experiments led researcher to believe that melanocytes were of epidermal origin[102]. Despite the first observation of the NC occurring decades prior to these experiments, it was not until the mid 1900's that the NC was decisively identified as the origin of melanocytes by dorsal neural tube transplant experiments described above[103,104]. Furthermore, the subsequent fate mapping experiments revealed that melanocytes in the skin were derived from the NC at all axial levels[19,27,34].

Tracing of migrating NC populations showed that, regardless of anteroposterior positioning, NCCs that followed a dorsolateral migration path between the non-neural ectoderm and the somites became melanocytes[105]. The *in vitro* clonal analysis of quail NC showed heterogeneity among clones. Roughly 66% of observed clones gave rise

solely to pigmented melanocytes, while 30% and 4% gave rise to entirely non-pigmented or mixed progeny, respectively[66]. These proportions did not change in the presence of neurotrophic factors, suggesting that the majority of clones collected during this period of delamination and migration had already become fate restricted and committed to the melanocyte lineage[34,66]. Indeed, later experiments in the chick and mice showed that migration of NC into the dorsolateral path initiates 24 hours after ventral migration[28,106–108]. Interestingly, the already delaminated NCCs were observed to pause migration before entrance into the dorsolateral path[109–111]. Further experiments uncovered that pre-commitment to the melanocyte lineage, referred to as a melanoblast identity, is required for dorsolateral migration to initiate[105]. Melanoblasts differentiate in response to WNT signaling to activate the expression of endothelin receptor type B (EDNRB), epithelial-cadherin (ECAD), and the receptor tyrosine kinase KIT to successfully utilize the dorsolateral migration path[112–117].

It would take another half decade and the utilization of modern transgenic lineage tracing tools to reveal that some ventrally migrating NCCs ultimately also differentiate into melanocytes. Fluorescently labeling based on expression of proteolipid protein 1 (PLP1) by SCPs showed for the first time that SCPs are a novel cellular origin of epidermal melanocytes[54]. While technically still a NC derivative, it is now appreciated that SCPs represent a temporally and transcriptionally unique intermediate for many NC lineages including melanocytes[50,51,64]. These SCPs migrate ventrally along preexisting nerve projections to the dermal tissue and ultimately give rise to an estimated 65% of the melanocyte population[54]. Neuregulin provided by the nerve fibers activate the Erb-b2

receptor tyrosine kinase 3 (ERBB3) receptor of SCPs to maintain SCP identity during migration[54,118]. Subsequent loss of nerve contact by the SCP in combination with insulin-like growth factor (IGF), platelet-derived growth factor (PDGF) and WNT signaling promotes the differentiation of melanocytes from SCPs[54]. Interestingly, the decision of a SCP to give rise to a melanocyte or a SC appears to be closely linked to nerve association as even mature myelinating SCs maintain potency to differentiate into a melanocyte after loss of nerve contact[54].

Further tracing of SCPs in chick showed a dorsoventral segregation in the epidermal locations of NC- and SCP-derived melanocytes. Dorsolaterally migrating melanoblasts were seen to be restricted to the epaxial domain while SCP-derived melanocytes primarily settled in the hypaxial region[119]. In mice, the use of both PLP1 and desert hedgehog (DHH) dependent transgenic lineage tracing strategies revealed that SCPs also give rise to extracutaneous melanocytes[120,121]. SCP-derived melanocytes are found throughout cardiac tissue where they have been described to play roles in valve stiffness, reactive oxygen species management and atrial arrhythmia triggering[122–124]. Development of the stria vascularis in the inner ear is also dependent on SCP-derived melanocytes[125–127]. While pigmentation of the SCP-derived melanocytes is not necessary for the function of the inner ear, it has been suggested that pigmentation may protect against hearing loss[128]. Additionally, SCP-derived melanocytes were found to colonize the brain meninges and the supraorbital spaces between the brain and eyes; however, the function of melanocytes in these locations is not yet known[120,129].

Regardless of the temporally distinct progenitor identity of a melanocyte, the transcriptional regulation governing melanocyte specification appears to share many commonalities. Microphthalmia-associated transcription factor (MITF) acts as a master regulator of melanocyte differentiation and identity[130–133]. MITF expression is controlled by WNT/ß-catenin dependent activity of NC transcription factors SRY-Box transcription factor 10 (SOX10) and paired box gene 3 (PAX3)[116,117,134–136]. The expression of these two NC transcription factors is maintained even in mature melanocytes. Glial lineages similarly utilize PAX3 and maintain SOX10 expression in mature derivatives. Fate commitment between glia and melanocytes is orchestrated by a cross-repressive transcription factor network involving forkhead box D3 (FOXD3) and SRY-Box transcription factor 2 (SOX2)[118]. FOXD3 expression is necessary for glial differentiation and has been shown to actively repress MITF expression[137]. Similarly, SOX2 appears to maintain SCP identity and inhibit MITF transcription[118]. Thus, melanocyte differentiation is dependent on the downregulation of FOXD3 and SOX2 to allow for MITF expression.

Once expressed, MITF induces the expression of many target genes. Proteins necessary for the synthesis of melanin, such as tyrosinase (TYR), tyrosinase-related protein 1 (TYRP1), dopachrome tautomerase (DCT), premelanosome protein (PMEL) and melan-A (MLANA), are known transcriptional targets of MITF[130,133,138]. Additionally, MITF also promotes the expression of genes important for melanocyte proliferation and survival[138]. Due to the shared expression of MITF, neural crest and SCP-derived melanocytes share the expression of many genes. However, technical limitations of *in vivo* methodologies have prevented the collection and profiling of pure NC- or SCP-derived melanocyte

populations. As such, the consequences of differentiating from a temporally distinct progenitor state on the transcriptional identity of a melanocyte have yet to be determined, despite the mounting evidence supporting heterogeneity among adult melanocyte populations[139,140].

1.4.2 Disease

To date, researchers have identified nearly 700 genes that are involved in melanocyte development, pigmentation, and function[141]. Mutation or other dysfunction in these gene products are responsible for a suite of disorders classified as pigmentation disorders. These disorders are subdivided into categories where the dysfunction results in either hyperpigmentation, hypopigmentation, or a mixed phenotype, and the pathogenesis of these disorders can either be congenital or acquired from environmental insults[101]. Diagnosis is dependent on many factors including the location of the mis-pigmented lesion as well as the size and morphology of the lesion[142].

The specific gene or aspect of pigmentation that is affected greatly alters the phenotype and clinical presentations of the disorder. Mutations that disrupt function of melanocyte specific genes involved in melanosome formation or melanin synthesis, such as TYR, PMEL or DCT, solely affect pigmentation. However, phenotypes can range from complete albinisms to more subtle, and sometimes location specific, loss or change of pigment appearance[143–145]. Mutations in the same genes that cause over activity of melanin production or that result in abnormal melanocyte proliferation result in widespread areas

of increased pigmentation, called lentigines, or isolated areas of hyperpigmentation, called a nevus[101]. The most common acquired pigmentation disorder is vitiligo, characterized as an auto-immune disorder in which a patient's immune system attacks and destroys melanocytes resulting in spots of hypopigmentation[146]. These disorders are largely benign, causing solely a cosmetic phenotype. However, patients affected by albinism and vitiligo are at higher risks for skin damage from UV radiation, and vitiligo patients often experience harmful inflammation in the inner ear and at other sights of extracutaneous melanocyte populations[147,148]. Additionally, patients affected by pigmentation disorders often experience anxiety due to abnormal cosmetic appearance[147,148].

Many cell types use the same genes in a cell type specific manner to achieve proper development, and the melanocyte lineage is no exception. Because of this, pigmentation phenotypes are often associated with larger syndromic disorders, affecting many tissues in the body. Dysregulation of melanocyte migration by mutations in serine/threonine kinase 11 (STK11) causes Peutz-Jeghers syndrome, characterized by ectopic pigmentation in the lips, palms of hands and soles of feet, as well as polyp formation in the gastrointestinal tract[149]. More obvious risk alleles include SOX10 and MITF, mutations in which cause Waardenburg syndrome characterized by numerous neural crest related defects including abnormal pigmentation[150,151]. Mutations in genes such as EDNRB and KIT, which are critical for the migration and survival of melanocyte progenitors as well as enteric nervous system progenitors from the vagal neural crest, result in Piebaldism and syndromic Hirschprung's disease[152–155]. Other syndromes such as LEOPARD syndrome,

Waardenburg-Shah syndrome, Alezzandrini syndrome, Tietz syndrome, and ABCD syndrome present with cardiac abnormalities and arrythmia and/or hearing loss or deafness[124,151,156–160]. Mutations causing these syndromes therefore affect the extracutaneous SCP-derived melanocyte populations and cause improper development and/or function in the respective tissues.

Current treatment of pigmentation disorders broadly follows two methods depending on the correction of hyperpigmentation or hypopigmentation. Hyperpigmentation is most frequently corrected by the topical application of a triple combination drug cream to the hyperpigmented area[161]. The mechanism of action of the cream is to promote shedding of the current hyperpigmented epidermal layer and restrict new melanin synthesis by inhibiting TYR function to prevent hyperpigmentation of the new epidermal layer[162]. Other options for treatment include chemical peels, light or laser therapies or surgical excision of the lesion[161]. Correction of hypopigmentation typically utilizes the application of corticosteroid creams to promote proliferation and migration of surrounding melanocytes into the unpigmented area to initiate repigmentation[163,164]. Other options include cellular replacement therapies, where a skin graft is taken from an area of normal pigmentation from the patient, dissociated, and applied with dermabrasion to the unpigmented skin area to reestablish the epidermal melanocyte population[165–167]. These cell transplantation therapies, however, are not ideal for diseases such as vitiligo, as initiation of depigmentation is believed to be triggered by stress, injury, or inflammation[148]. As such, depigmentation may initiate at the site of graft collection, or quickly reoccur at the graft location due to invasiveness of the procedure.

Oncogenic transformation of melanocytes results in one of the most metastatic and therefore deadly forms of skin cancer, melanoma. Transformation often results from a combination of somatic mutations from UV radiation or other injury as well as from congenital risk factors[168]. Somatic mutations in the gene BRAF, which functions to regulate cell cycle progression, are the most common cause of oncogenic transformation in melanocytes[169]. However, the same genes responsible for the above-mentioned syndromes, such as LEAPORD syndrome, also increase a patient's risk for melanoma[170]. For instance, genetic mutations which alter melanocyte migration results in melanocytes in atypical signaling environments, potentially causing abnormal proliferation, survival and/or further migration. While the melanoma tumors that form in the skin are relatively harmless, the health risk come from the high propensity for melanoma to metastasize to other organs.

Mounting evidence in almost all fields of cancer biology has shown that transformed cell populations frequently undergo dedifferentiation, reverting to a more progenitor like identity[171]. In the case of melanoma, as well as other NC lineage derived tumors like glioblastoma, dedifferentiation is especially problematic due to the high migratory potential of melanoblasts and NCCs. Concurrently, researchers have found many examples of melanoma cells reactivating gene networks important for NC and melanocyte development[172,173]. Some of these genes, such as SOX10, are to be expected due to their continued expression in mature melanocytes. Unexpectedly, recent experiments in a zebrafish model of melanoma initiation revealed that oncogenic transformation coincided

with the reactivation of a development specific NC gene, crestin, and epigenetic signatures normally made inaccessible in the mature melanocyte[174]. This experiment suggests that dedifferentiated melanoma cells revert to a progenitor state not only transcriptionally, but also epigenetically, allowing transcription factors to function in a developmental context.

The treatment option with the best survival outcome for melanoma patients is identification at stage 0 and excision of the benign tumor from the skin before it becomes metastatic. However, if metastasis has occurred at the point of diagnosis, standards of treatment depend on the extent of the melanoma malignancy. Non-melanoma specific treatments include radiation therapy or chemotherapy to directly kill the highly proliferative cancer cells, or immune checkpoint inhibitors that function to block evasion of the cancer cell from the immune system[175–177]. Targeted therapies for melanoma have also been developed, such as mitogen-activated protein kinase kinase (MEK) and BRAF inhibitors for melanomas arising from BRAF mutations or imatinib and nilotinib for melanomas with activating KIT mutations[178–180]. The rates of melanoma progression and the effectiveness of these targeted treatments varies between cases, often depending on the location of the primary tumor site[140,169,181]. This suggests diversity among melanoma cases, even those which arise from the same oncogenic transformation.

1.5 Heterogeneity in melanoma

Diversity and complexity among melanoma cases comes in many flavors. From patient to patient, primary melanoma tumors arise due to different underlying mutations, either congenital or somatic, and at different anatomical locations[169,181]. In the clinic, these two critical variables are correlated with prognosis due to differing rates of disease progression, metastasis, and response to therapeutics. Efforts to determine the underlying pathogenesis and etiology of melanoma variability has revealed differences in oncogenic driver mutations, mutation burden and bulk transcriptional identity based on anatomical location of the primary tumor: cutaneous, acral, uveal or mucosal[181,182]. Performing scRNAseq on melanoma tumors has additionally revealed intra-tumoral heterogeneity that exemplifies the dedifferentiation process[182].

Cutaneous melanoma (CM) is the most common subtype of melanoma. The prevalence of CM is owed to UV radiation being the main transformative driver of oncogenesis. This also results in CM tumors displaying the highest somatic mutational burden among the melanoma subtypes[169,183,184]. CM cases differ in presentation of oncogenic mutational drivers, with about half containing BRAF mutations, one third containing RAS mutations, one eighth containing neurofibromatosis type 1 (NF1) mutations and the remainder are triple wild-type (TWT) or KIT mutants[169,184]. Levels of MITF expression also vary among CM cases and appear to be correlated to progression and metastasis. Low MITF expression typically indicates a more dedifferentiated tumor with increased invasiveness and inherent mitogen-activated protein kinase (MAPK) inhibition resistance[185]. High MITF

expression is normally an indication for a favorable prognosis; however in some cases this phenotype confers drug resistance and promotes metastasis[186–188].

Of great interest to both researchers and clinicians is the identification of biomarkers for metastatic potential in CM. Independent categorization of CM cases based on transcriptional profiles and retrospective patient outcomes have identified four transcriptional features correlating to prognosis. As mentioned above, cases with low MITF expression and proliferative signatures were associated with poor prognosis. Conversely, cases with high immune response signatures, high MITF/pigmentation or keratin signatures all correlated with more favorable prognosis[184,187,189,190]. Thanks to these findings, clinical researchers have developed a gene expression profile test which measures the expression level of 31 different genes to help predict the likelihood of metastasis[191–198].

While the development of melanoma targeted therapies has greatly benefited most patients, 30% of CM cases with BRAF mutations show intrinsic resistance to BRAF inhibitor treatment[199]. The majority of BRAF resistant cases are due to parallel loss of the gene phosphatase and TENsin homolog (PTEN), resulting in constitutive activation of the phosphatidylinositol 3-kinase and protein kinase B (PI3K/AKT) proliferation and survival pathway[200]. Some studies also show that high MITF expression confers BRAF and MEK inhibitor resistance[201,202]. Conversely, a MITF low and receptor tyrosine kinase AXL high phenotype, indicative of a dedifferentiated and highly invasive state, similarly shows

BRAF resistance[185]. These results suggest differing functions of MITF in melanoma, dependent of the broader transcriptional, and likely epigenetic, state of the CM.

Acral melanoma (AM) is melanoma that arises on the palms of hands, soles of feet or nail beds. AMs display lower UV radiation derived point mutation but higher incidence of larger somatic mutations resulting in amplification or the loss of gene expression[169,203]. For example, roughly half of all profiled AM cases present with either BRAF, RAS or NF1 mutations, while the other half present with copy number gain or promoter activating mutations in the telomerase pathway gene, telomerase reverse transcriptase (TERT)[169,203,204]. KIT mutation and amplification are also more common drivers of AM transformation[203,205]. In addition to KIT and TERT, p21-activating kinase (PAK1), cyclin dependent kinase 4 (CDK4) and cyclin D1 (CCND1) are also frequently found to be amplified, while cyclin dependent kinase inhibitor 2A (CDKN2A), PTEN and NF1 are frequently deleted[203,206]. If a patient's AM does not present with BRAF or KIT mutations, these patients are unable to benefit from any currently available targeted treatments.

Uveal melanoma (UV), also called intraocular melanoma, has the lowest somatic mutation burden of all the anatomical melanoma subtypes[184]. However, roughly half of all UV cases present with an activating mutation in either guanine nucleotide-binding protein G(q) (GNAQ) or guanine nucleotide-binding protein subunit alpha-11 (GNA11), both effectors of the MAPK pathway[207,208]. In conjunction, four fifths of all UM cases present with mutated ubiquitin carboxyl-terminal hydrolase (BAP1), a gene involved in DNA damage response and proliferation[207,209–211]. UMs subtypes are also grouped based on

chromosomal copy number alterations. Deletion of a copy of chromosome 3 (Monosomy 3) and duplication of the long arm of chromosome 8 are both associated with high metastasis risk, though the underlying cause for this is still an area of active research[209,212–216]. UM case prognosis predictions are also informed from the same gene expression profiling performed for CM[191].

Mucosal melanoma (MM) is both the rarest and most aggressive anatomical subtype of melanoma[217,218]. MM cases also present with lower mutational burden and higher instances of chromosomal abnormalities[169,219]. MM has mostly been characterized by its similarities to other melanoma subtypes. MM cases share mutational drivers with UM such as activating GNAQ mutation, or loss of CDKN2A as seen in AM[169,205,206]. Like, AM, MM occasionally presents with activating KIT mutations, however, targeted KIT therapies are less effective in MM[220,221].

Recent work has presented convincing evidence that the root cause of anatomical site derived melanoma heterogeneity is due to the differing transcriptional identity of anatomical site-specific melanocyte sub populations. Comparison of cutaneous and acral melanocytes in zebrafish show that anatomical position identity explained the largest source of transcriptional variation behind only cell type identity[140]. Genes driving this variation were familiar axial identifiers such as HOX13[140]. Subsequent analysis of human AM cases similarly showed high expression of HOXA13, HOXB13 and HOXD13, both in primary and metastatic samples, indicating retention of anatomical identity in new tissue environments[140]. Similar studies analyzing volar and non-volar human melanocyte

populations across developmental time found unique transcriptional signatures for each population that were established early in development[139]. The volar melanocyte signature was subsequently shown to be enriched in AM cases compared to CM cases[139].

The advent of scRNAseq and its application to melanoma profiling has revealed substantial intra-tumor heterogeneity in melanoma. These datasets have allowed for a more thorough characterization of tumor immune infiltration and tumor-immune interactions[222–226]. For example, sequencing of primary and corresponding metastatic UM metastasis has shown the ability for an innate immune response in the primary tumor and antibody directed immune infiltration in the metastatic site[222]. Parallel profiling of human melanocyte development by scRNAseq has revealed that intra-tumor heterogeneity may correspond to different stages of dedifferentiation within a single tumor[139]. Interestingly, hierarchical clustering of tumor samples based on predicted dedifferentiation composition does not show any correlation to genetic driver or tumor site but was a significant predictor of patient survival[139].

Altogether, profiling of melanoma cases has revealed substantial heterogeneity[169,181,182]. Historical classification of melanoma is based on the anatomical site of the primary tumor, and different anatomical subtypes indeed show differences in clinical presentations[181]. However, more recent research suggests that, regardless of anatomic site, the dedifferentiation status of the tumor may be more predictive of prognosis[139]. Considered together, these observations raise important new points concerning the identity of melanocytes and subsequent transformation. Spatial distribution biases have been

observed between NC- and SCP-derived melanocytes, including enrichment of SCP-derived melanocytes in the limbs[54,119]. Additional work will be necessary to understand whether observed differences in spatially distinct melanocyte sub populations arise exclusively due to their locations or, perhaps, are influenced by progenitor identity[139,140]. Importantly, higher resolution profiling of NC- and SCP-derived melanocytes, and their respective intermediate progenitors, will be necessary to evaluate the full potential of melanoma dedifferentiation. Of particular interest will be whether tumors that arise from a SCP-derived melanocyte have exclusive access to an SCP-like dedifferentiation identity, and the consequences of this identity versus a NC-like identity[51,139].

1.6 Stem-cell based systems to model and progress neural crest development and lineage research

Findings derived from studying the developing frog, chick, mouse and zebrafish embryos have undisputedly provided the foundation of the field of NC biology[227]. Best said by Viktor Hamburger, “Our real teacher has been and still is the embryo – who is, incidentally, the only teacher who is always right.”[228] Hamburger did, however, forget to mention that some of the lessons from the embryo, like NC development, are incredibly complicated to dissect and understand. In fact, the most fascinating aspects of NC biology, such as the migratory ability and the transiency, are also the aspects that make the NC challenging to study *in vivo*.

In particular, the application of modern omics techniques to profile NC identity and development face many technical and conceptual challenges. Any omics technique, whether profiling a cell population in bulk or at single cell resolution, requires a high cell number at a high degree of purity for robust analysis. While many researchers have utilized transgenic models to label and purify NCCs, the yield from a single embryo is low and NCC preparations from multiple embryos must be pooled together[51,86,92,229–232]. Additionally, NCCs migrate into tissues with diverse adhesion properties. Protocols to dissociate whole embryos or tissues may result in incomplete dissociations and thus an incomplete sampling of the NC population. Additionally, due to the nature of embryonic elongation and neural tube formation, the timing of NC specification and migration occur at different developmental times at different axial levels[10]. This makes comparing NC populations across distant axial identities at the same stage of NC development, such as pre-migratory cranial and sacral populations, impossible in the same embryo. The use of single cell transcriptomic profiling to reconstruct pseudotime lineage specification relies on a continuum of multipotent to differentiated cells of the same lineage to be present in a dataset. Evidence for cell intrinsic differences in NCCs based on temporal identity complicates these assumptions[32,34,77]. Even in the same axial region, the late NCCs captured in a snapshot of embryonic development may be restricted or biased to produce lineages different from those derived from the earlier migrating NC and thus are not true progenitors to the differentiating cells captured in the dataset.

Human pluripotent stem cell differentiation models have provided access to tissues and cell types that are difficult to obtain from primary tissue, including the NC. On top of being

able to model biological processes in a human system, these stem cell derived cultures also simultaneously address the issues of tissue availability and cell number. NC differentiations are scalable and thus amenable to high throughput assays and screens that will be critical for the development of treatments for neurocristopathies and other NC related disorders. These cultures are also reproducible and reductionistic, key features for performing tests of NC competency. Modeling a developmental process in a dish also allows for the repeated observation of the same differentiating population over time.

NC differentiation protocols stem from protocols used to derive central nervous system derivatives through production of neural rosettes[233,234]. Like *in vivo*, NCCs become specified around the border of the neural ectoderm-like rosettes and the surrounding nonneural ectoderm like cells, and addition of growth factors like FGF, WNT and BMP increase neural crest population percentages[235]. Protocols using the embryoid body or rosette derivation method also rely on the migratory abilities of the NC for purification[236]. Subsequent iterations address problems with these protocols, such as undefined media conditions, long differentiation time and low yield, by using a SMAD inhibition approach for neuroectoderm differentiation[237]. Parallel WNT activation by the chemical GSK-3ß inhibitor, CHIR, further increases neural crest induction efficiency[238,239]. In addition to the increased efficacy, these differentiation methods are also “directed,” where the stem cells are guided through the same order of developmental progression observed *in vivo* to reach a NC fate.

The central concept of this fully defined, directed NC differentiation method has evolved into many subsequent protocol iterations which alter key aspects of NC identity. Axial patterning of NC identity was first shown by addition of RA. Standard differentiation conditions yielded HOX negative neural crest cells indicating a cranial spatial identity, while addition of RA during NC induction stimulated HOX gene expression indicative of the vagal identity[238,240]. Subsequent iterations have generated trunk NC through a neuro-mesodermal progenitor using high WNT and FGF activation[241]. Most recently, addition of growth differentiation factor 11 (GFD11) to the trunk NC protocol has been shown to produce sacral NCCs[242].

Using NCCs patterned to distinct axial identities as an intermediate, researchers have extended these protocols to generate methods for the *in vitro* derivation of many NC lineages. Mesenchymal derivatives can be produced by cultures of cranial NC treated with FGFs[243,244]. However, treatment of the same cells with neurotrophic factors yields cultures of sensory and sympathetic neurons[245–247]. Importantly, treatment of vagal NCCs with the same neurotrophic factors generates heterogenous cultures of enteric neurons[240]. Similarly, enteric neurons can be induced from sacral NC cultures[242]. Treatment of cranial NC cultures and posteriorized identities with endothelin 3 (EDN3) and BMP4 generate melanoblasts capable of maturing into pigmented melanocytes[238]. Most recently, hPSC-derived NCCs have also been shown to be amenable to temporal patterning. Prolonged maintenance of NC identity is required prior to neuregulin treatment to efficiently differentiate SCs or glial derivatives[248]. All together, these data indicate that

hPSC-derived NCCs can be spatiotemporally patterned to recapitulate *in vivo* lineage competence.

In addition to the benefit of scalability, the recapitulation of *in vivo* biology by directed stem cell differentiations facilitates the characterization of disease mechanisms and profoundly increases the potential for efficacious drug discovery. This utility was exemplified by drug discovery efforts for inhibiting SARS-CoV-2 infections. Early efforts utilized HEK293T cells transfected with angiotensin converting enzyme 2 (ACE2), which facilitated the discovery of molecules which interrupted the virus-receptor binding process[249–251]. However, as HEK293T cells do not endogenously express ACE2, these studies were unable to explain clinical observations like variability in disease severity and viral load. High throughput drug screens performed on hPSC-derived cardiomyocytes, a cell type that endogenously expressed ACE2, enabled the identification of drugs which modulate ACE2 expression by acting on the endogenous ACE2 gene regulatory network[252]. The gene targets of the identified drugs also gleaned insights into the observed clinical variability by implicating androgen signaling as a pathway upstream of ACE2 expression[252].

To date, stem cell derived NCCs and NC derivative cell types have been utilized to model and uncover potential therapies for multiple NC related disorders. Patient derived hPSCs containing pigmentation disorder causing mutations have been used to model defects in melanosome formation and trafficking in hPSC-derived melanocytes[238]. Similarly, hPSC-derived SCs recently permitted the modeling of diabetic peripheral neuropathy and the

identification of preventative therapeutic molecules[248]. The introduction of an EDNRB mutation in hPSCs has also enabled the discovery of molecules capable of compensating for EDNRB-mediated migration defects in vagal NCCs[253]. Utilizing a protocol to differentiate the vagal NCCs to enteric neurons, researchers have identified modulators of enteric neuron differentiation and activity, as well as a mechanism and therapeutic for chemotherapy induced enteric neuropathy[254–256]. Beyond drug discovery, these systems also show therapeutic potential as sources for cell replacement therapies. Amazingly, transplantation of vagal and sacral NCCs, as well as more differentiated vagal NCC-derived enteric neurons have shown extensive engraftment and incorporation into endogenous enteric neuron networks in mouse gastrointestinal tracts[242,253,255].

These methods to pattern and differentiate NCCs *in vitro* offer a unique model to assess NC population and clonal potency, and profile hard-to-collect NCCs and their derivatives with omics methods[257]. Of particular interest will be the use of these differentiation models to understand how the unique spatiotemporal identity of a NCC alters the identity of the daughter cell type. For my dissertation work in Chapter 2, I use hPSC-derived models of NC temporal patterning to characterize heterogeneity in temporally distinct NC populations. I then develop a protocol for the derivation of melanocytes from a SCP intermediate, compare these to melanocytes derived from the temporally distinct NC progenitor, and validate these findings *in vivo*. Finally, I relate the transcriptional differences between these melanocytes to observed melanoma heterogeneity. This work advances our understanding of developmental sources of heterogeneity in melanocytes

and in melanoma, while simultaneously highlighting the utility of directed stem cell differentiations for making novel discoveries about development.

Chapter 2 Generation of Schwann cell derived melanocytes from hPSCs identifies pro-metastatic factors in melanoma

2.1 Abstract

The NC is highly multipotent and generates diverse lineages in the developing embryo. However, spatiotemporally distinct NC populations display differences in fate potential, such as increased gliogenic and parasympathetic potential from later migrating, nerve-associated SCPs. Interestingly, while melanogenic potential is shared by both early migrating NC and SCPs, differences in melanocyte identity resulting from differentiation through these temporally distinct progenitors have not been determined. Here, we leverage a human pluripotent stem cell model of NC temporal patterning to comprehensively characterize human NC heterogeneity, fate bias, and lineage development. We captured the transition of NC differentiation between temporally and transcriptionally distinct melanogenic progenitors and identified modules of candidate transcription factor and signaling activity associated with this transition. For the first time, we established a protocol for the directed differentiation of melanocytes from hPSCs through a SCP intermediate, termed trajectory 2 (T2) melanocytes. Leveraging an existing protocol for differentiating early NC-derived melanocytes, termed trajectory 1 (T1), we performed the first comprehensive comparison of transcriptional and functional differences between these distinct melanocyte populations, revealing differences in pigmentation and unique expression of transcription factors, ligands, receptors and surface markers. We found a significant link between the T2 melanocyte transcriptional

signature and decreased survival in melanoma patients in the cancer genome atlas (TCGA). We performed an *in vivo* CRISPRi screen of T1 and T2 melanocyte signature genes in a human melanoma cell line and discovered several T2-specific markers that promote lung metastasis in mice. We further demonstrated that one of these factors, SNRPB, regulates the splicing of transcripts involved in metastasis relevant functions such as migration, cell adhesion and proliferation. Overall, this study identifies distinct developmental trajectories as a source of diversity in melanocytes and implicates the unique molecular signature of SCP-derived melanocytes in metastatic melanoma.

2.2 Introduction

The NC is a transient, multipotent, fetal cell population specified along the dorsal neural tube that gives rise to diverse cell types, such as peripheral neurons and glia, melanocytes, cranial osteoblasts and chondrocytes[1]. During normal development, diversification of potency throughout the NC population remains a topic of extensive research[258]. Lineage tracing, chimeric grafts and explant experiments have provided compelling evidence that NC fate potential is both regionally and temporally restricted during normal development. The combination of a NCC's position along the rostrocaudal axis and duration of migration determines its lineage options[69,71,87–89,259,260]. This points to cell-intrinsic differences in spatiotemporally distinct NCCs[34,261,262].

Understanding the molecular programs underlying NC lineage potential and restriction has implications in basic stem cell and developmental biology as well as for the

development of therapies for numerous neurocristopathies. However, the transient and migratory nature of NCCs pose challenges in tissue accessibility and scalability necessary for -omics level studies and high-throughput molecular perturbations, especially from human tissue. Established strategies for differentiating NCCs from hPSCs have provided an alternative model system with the ability to pattern into cranial, vagal, trunk and sacral regional identities. Recently, Majd et al. demonstrated temporal patterning of hPSC-NCCs with prolonged culture of 3D spheroids resulting in more efficient differentiation to glial lineages, mimicking the *in vivo* shift to gliogenesis in late-migrating NCCs[242,248,253,263,264]. This differentiation system enables the study of temporal fate restriction in NCCs, and promises access to lineages that emerge from late-migrating NCCs, such as parasympathetic neurons[57,58]. Interestingly, the melanocyte lineage is uniquely accessible to both early and late migratory NCCs[54,119]. However, further characterizations are needed to determine how temporally distinct differentiation trajectories affect melanocyte identity and function.

In this study, we characterized the temporal changes in hPSC-NCC populations using single cell transcriptomics, revealing changes in glial propensity and temporarily distinct melanogenic progenitors with unique transcription factor and signaling activity. Building on the protocol described by Majd et al., we developed a strategy for the directed differentiation of melanocytes from hPSCs through a SCP intermediate, and molecularly and functionally compared them to hPSC-derived melanocytes differentiated through an early NC intermediate[238]. Further, we demonstrated that the transcriptional signature of SCP-derived melanocytes is linked to differences in survival outcomes in melanoma.

Finally, by performing a CRISPR screen using an *in vivo* metastasis model, we identified SCP-derived melanocyte transcripts that promote metastasis in melanoma.

2.3 Results

2.3.1 Emergence of heterogeneity in fate potential during neural crest lineage progression

To systematically characterize how hPSC-NCC populations change over time, we performed scRNAseq at five stages (S1-S5) of our previously established SC differentiation[248]. The timepoints sequenced were chosen to capture different stages of NCC specification and maturation: the earliest emergence of SOX10+ NCCs during the induction phase, an early, intermediate, and late stage of neural crest progression, and an early stage of glial induction (Figure 2.1A-B). Each timepoint was clustered and analyzed separately to preserve real-time information (Figure 2.1C), and clusters were annotated by the expression of established lineage markers (Figure 2.2A).

On day 6 (D6) of the NC induction, pseudotime analysis revealed that the cell-type composition of the cultures closely resembles the developing neural plate, containing PAX6+/EMX2+ central nervous system (CNS) precursors, GATA3+/CDH1+ non-neural ectoderm (NNE), PAX3+/WNT1+ pre-migratory NCCs, and SOX10+/SNAI2+ stage 1 NCCs emerging from the pre-migratory NCC clusters (Figure 2.2B). Studies in animal models have identified a complex network of WNT, FGF, and BMP signaling required to

pattern the neural plate and for NCCs to develop along the neural plate border[117,265]. Interestingly, the prediction of ligand-receptor interactions using CellChat analysis[266] suggests these signaling networks establish themselves in human cells *in vitro* at stage 1 of differentiation (Figure 2.2C). Importantly, the CNS precursor population also scored highly for the expression of negative WNT and BMP gene modules (Figure 2.2D). Taken together, these data suggest that our directed NC differentiation strategy generates cultures reminiscent of the developing neural plate border to facilitate the signaling necessary for efficient specification/generation of NCCs from hPSCs. This NCC induction strategy resulted in heterogeneous cultures at D15 containing CNS precursors, non-neural ectoderm, SIX1+/POU4F1+ placode, and TWIST1+ mesenchymal cells. These "off-target" but developmentally relevant cell-types were then selected against during the 3D neural crest progression phase, where NCCs selectively aggregated with other NCCs until D30, yielding cultures of >75% SOX10+ cells by day 22 (Figure 2.1C, 2.2E).

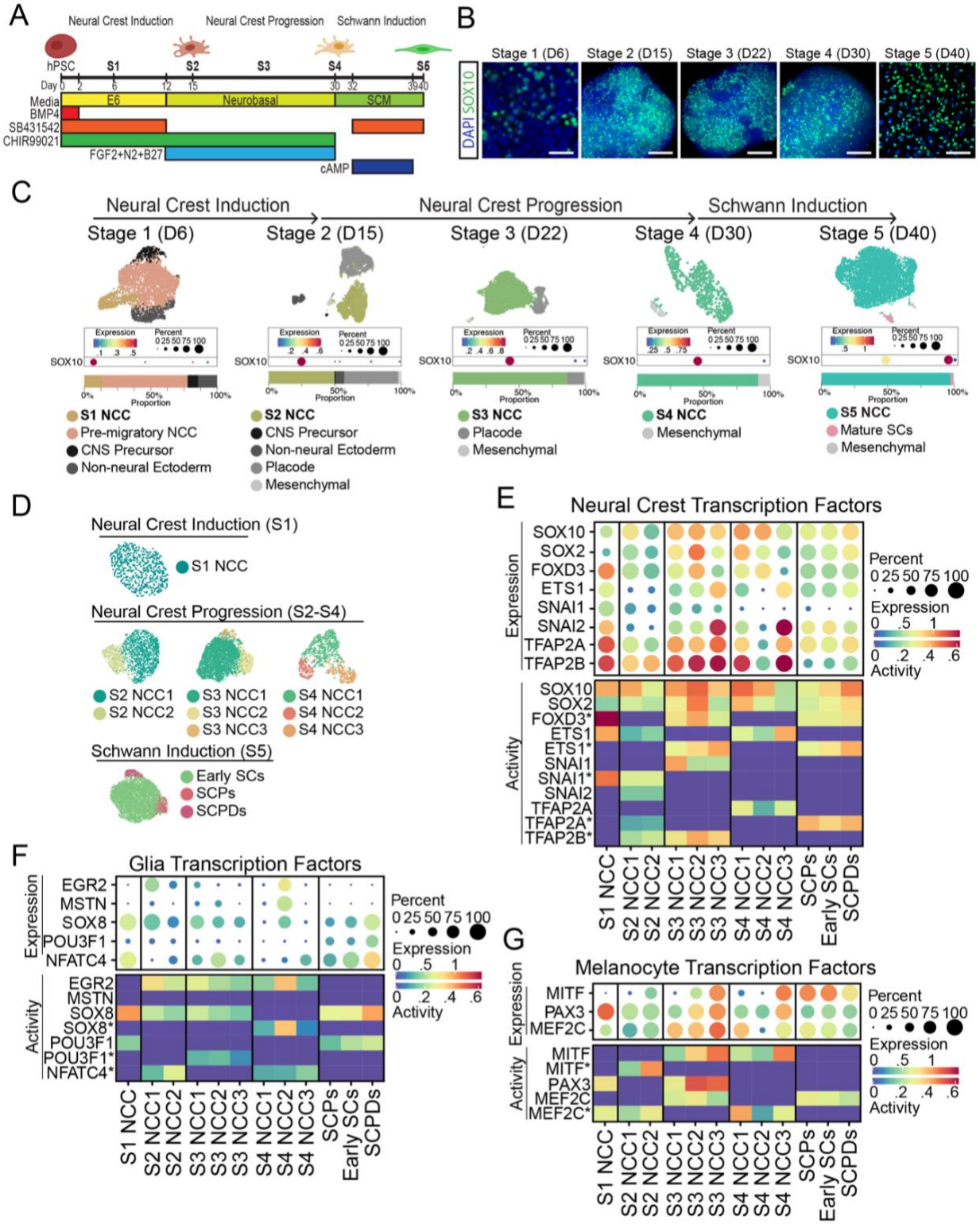

Figure 2.1: Melanogenic NCCs emerge during hPSC differentiation towards Schwann cells
A) Schematic of directed differentiation protocol to differentiate human pluripotent stem cells to Schwann cell precursors with defined media conditions. The protocol consists of three phases:

neural crest induction, neural crest progression and finally Schwann induction. Abbreviations: E6 = Essential 6, SCM = Schwann Cell Media.
B) Representative SOX10 expression (green) in hPSC-derived NCCs in stage 1 monolayer neural crest induction, stage 2-4 crestospheres and stage 5 SCP induction. Scale bar represents 100um.
C) UMAP embedding, SOX10 expression, cluster proportions, and cluster annotation of stages 1-5 of hPSC neural crest induction, progression, and Schwann induction.
D) UMAP embeddings and subclustering of stages 1-5 SOX10+ clusters.
E) Expression (top) and predicted activity (bottom) of canonical neural crest transcription factors in stage 1-5 NCC and Schwann subclusters. Asterisks represent TF activity predicted from lower confidence motif annotations.
F) Expression (top) and predicted activity (bottom) of canonical glial transcription factors in stage 1-5 NCC and Schwann subclusters. Asterisks represent TF activity predicted from lower confidence motif annotations.
G) Expression (top) and predicted activity (bottom) of canonical melanocyte transcription factors in stage 1-5 NCC and Schwann subclusters. Asterisks represent TF activity predicted from lower confidence motif annotations.

To characterize the transcriptional changes in our NCCs as they progress through differentiation, we next aimed to analyze the heterogeneity of the SOX10+ NCC clusters across the time points (Figure 2.1C). The emerging S1 NCCs were homogenous, remaining as a single cluster, while S2, S3, and S4 NCCs contained two, three, and three subclusters, respectively (Figure 2.1D). Stage 5 NCCs also contained three subclusters (Figure 2.1D), which were annotated by comparison to our previously published[248] Schwann cell dataset from a similar differentiation stage. For this comparison we used similarity weighted non-negative embedding (SWNE)[267]. We generated the dimensionally reduced SWNE space based on the published dataset and the stage 5 NCCs were subsequently projected into the same SWNE dimensions, such that transcriptionally similar cells were plotted in the same coordinates (Figure 2.2F). All subclusters expressed canonical NC transcription factors (TFs) SOX10, SOX2, FOXD3, TFAP2A/B, and SNAI1 or SNAI2, with expression levels varying between clusters but not correlating directly to SOX10 expression (Figure 2.1E, top).

A new model of NCC fate determination describes the co-activation of competing lineage modules which resolve into fate-biased and then fate-committed NCCs[92]. To determine if hPSC-derived NCC populations exhibit differences in fate potential, we examined both the expression of transcription factors involved in early neuronal (sensory and autonomic), melanogenic, gliogenic, and mesenchymal fate specification, as well as their predicted activity using single-cell regulatory network inference and clustering (SCENIC) analysis[268]. While SOX10 is predicted to be active in all SOX10+ subclusters, with activity level correlating to expression level, other TFs like SNAI2 in S3 and S4 NCCs, TFAP2A in S3 NCCs, and TFAP2B in S4 NCCs showed no predicted activity despite high expression levels (Figure 2.1E, bottom). The results highlight the importance of considering activity as well as expression for predicting fate potential.

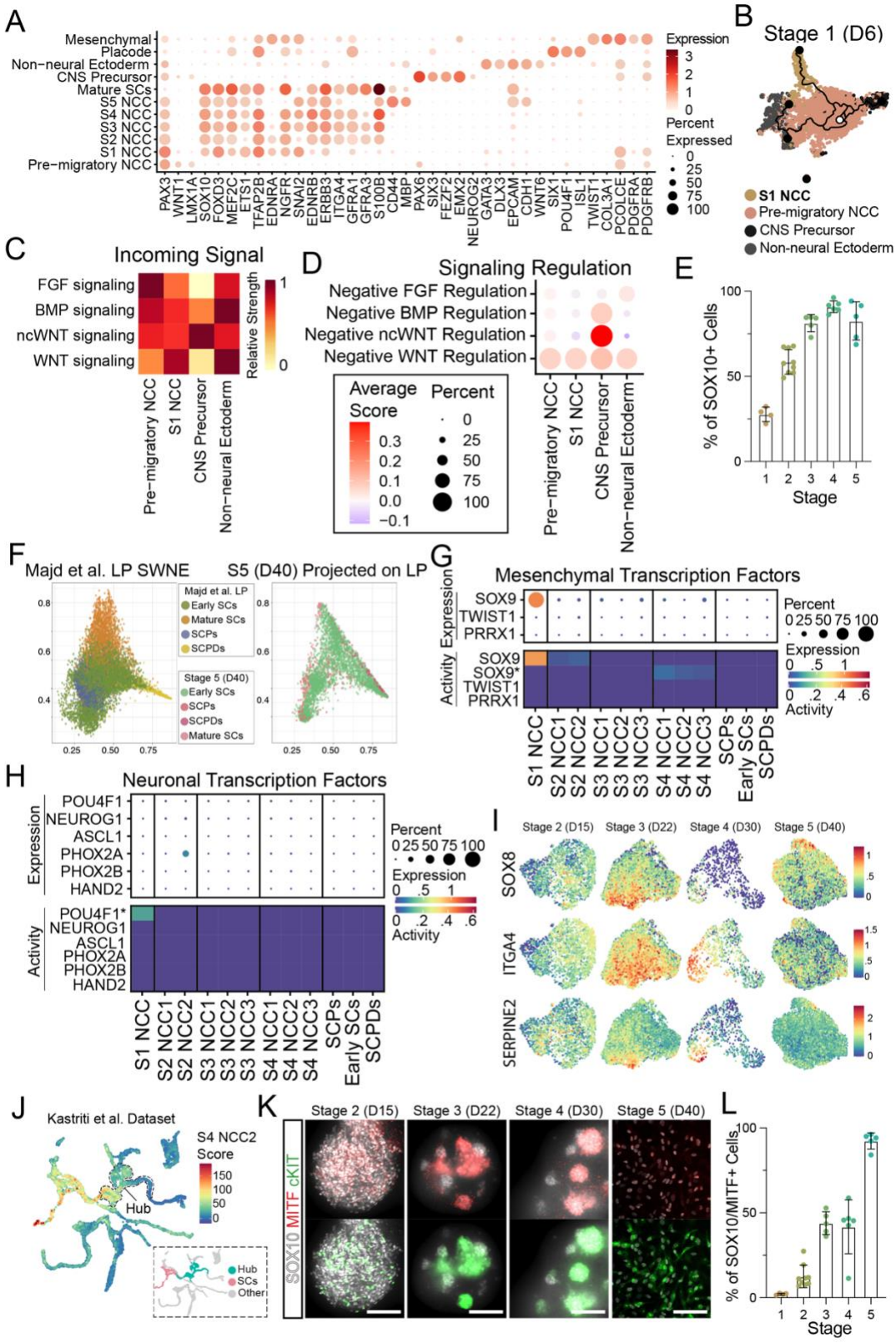
A
Mesenchymal
Placode
Non−neural Ectoderm
CNS Precursor
Mature SCs
S5 NCC
S4 NCC
S3 NCC
S2 NCC
S1 NCC
Pre−migratory NCC
PAX3 WNT1 LMX1A SOX10 FOXD3 MEF2C ETS1 TFAP2B EDNRA NGFR SNAI2 EDNRB ERBB3 ITGA4 GFRA1 GFRA3 S100B CD44 MBP PAX6 SIX3 FEZF2 EMX2 NEUROG2 GATA3 DLX3 EPCAM CDH1 WNT6 SIX1 POU4F1 ISL1 TWIST1 COL3A1 PCOLCE PDGFRA PDGFRB
Expression
Percent Expressed
B
Stage 1 (D6)
S1 NCC
Pre-migratory NCC
CNS Precursor
Non-neural Ectoderm
C
Incoming Signal
FGF signaling
BMP signaling
ncWNT signaling
WNT signaling
Relative Strength
Pre−migratory NCC
S1 NCC
CNS Precursor
Non−neural Ectoderm
D
Signaling Regulation
Negative FGF Regulation
Negative BMP Regulation
Negative ncWNT Regulation
Negative WNT Regulation
Average Score
Percent
E
% of SOX10+ Cells
Stage
F
Majd et al. LP SWNE
S5 (D40) Projected on LP
Majd et al. LP
Early SCs
Mature SCs
SCPs
SCPDs
Stage 5 (D40)
G
Mesenchymal Transcription Factors
Expression
SOX9
TWIST1
PRRX1
Activity
SOX9
SOX9*
TWIST1
PRRX1
S1 NCC S2 NCC1 S2 NCC2 S3 NCC1 S3 NCC2 S3 NCC3 S4 NCC1 S4 NCC2 S4 NCC3 SCPs Early SCs SCPDs
H
Neuronal Transcription Factors
POU4F1
NEUROG1
ASCL1
PHOX2A
PHOX2B
HAND2
POU4F1*
I
Stage 2 (D15) Stage 3 (D22) Stage 4 (D30) Stage 5 (D40)
SOX8
ITGA4
SERPINE2
J
Kastriti et al. Dataset
S4 NCC2 Score
Hub
Hub
SCs
Other
K
Stage 2 (D15) Stage 3 (D22) Stage 4 (D30) Stage 5 (D40)
SOX10 MITF cKIT
L
% of SOX10/MITF+ Cells
Stage

Figure 2.2: Differentiation of hPSCs toward NCC and Schwann cells yields heterogeneous populations with different lineage potentials
A) Expression of canonical cell type markers in stage 1-5 clusters used for cell type annotation.
B) Pseudotime lineage prediction of stage 1 neural crest induction. Cells (points) are colored by cell type cluster. Black lines follow predicted paths of transcriptional change from selected starting nodes (white circle) to terminal nodes (black circle).
C) Predicted relative strength of cell type response to incoming signaling pathways necessary for neural plate patterning.
D) Modules scoring of gene ontology gene lists for negative regulation of neural plate patterning signals.
E) Flow cytometry-based quantification of SOX10 positive populations in stage 1-4 crestospheres and stage 5 SCP induction. Error bars represent standard deviation, S1 n = 4, S2 n = 9, S3 n = 5, S4 n = 6, S5 n = 5.
F) Projection of stage 5 Schwann subclusters and cell types into the SWNE embeddings of the "low passage" Schwann induction dataset published in Majd et al. Cells (points) with similar SWNE coordinates are transcriptionally similar to one another. Abbreviations: SCs = Schwann Cells, SCPs = Schwann Cell Precursors, SCPDs = Schwann Cell Precursor Derivatives.
G) Expression (top) and predicted activity (bottom) of canonical mesenchymal transcription factors in stage 1-5 NCC and Schwann subclusters. Asterisks represent TF activity predicted from lower confidence motif annotations.
H) Expression (top) and predicted activity (bottom) of canonical sensory and autonomic neural transcription factors in stage 1-5 NCC and Schwann subclusters. Asterisks represent TF activity predicted from lower confidence motif annotations.
I) Feature plots of normalized expression for hub markers SOX8 (top), ITGA4 (middle) and SERPINE2 (bottom) in stage 2-5 NCC and Schwann subclusters.
J) Feature plot Kastriti et al. dataset colored by module score for S4 NCC2 top 100 marker genes. Dotted line outlines the cells annotated as "Hub" by the original authors. UMAP inlay colored by author annotations for the Hub and SC cells.
K) SOX10 (white), MITF (red) and cKIT (green) expression in stage 2-4 crestospheres and stage 5 SCP induction. Scale bar represents 100um.
L) Flow cytometry-based quantification of SOX10 positive and SOX10/MITF double positive populations in stage 1-4 crestospheres and stage 5 SCP induction. Error bars represent standard deviation, S1 n = 4, S2 n = 9, S3 n = 5, S4 n = 6, S5 n = 5.

Notably, mesenchymal lineage markers showed minimal expression and activity throughout NCC progression, apart from SOX9 in emerging S1 NCCs (Figure 2.2G). As well, NCC populations showed no bias toward neuronal fates based on neuronal transcription factor expression or activity during any stage of differentiation (Figure 2.2H). These results suggest that under our Schwann cell differentiation conditions, NCCs do not activate these developmental programs in the absence of exogenous signals for induction of mesenchymal and neuronal fates.

In agreement with our previous findings[248], the Schwann cell master regulator EGR2 showed the highest level of expression and activity in S4 NCC2 compared to earlier S1-S3 populations and other S4 NCC subtypes (Figure 2.1F). Interestingly, S4 NCC2 also expressed MSTN and SOX8 with high predicted SOX8 activity, both markers of NCCs transitioning to a SCP or “hub” transcriptional state recently described by Adameyko and colleagues[51,92] (Figure 2.1F). “Hub” cells are multipotent late-stage progenitors in the NC lineage that are primed toward Schwann cells and other late-emerging fates. To further characterize the emergence of the “hub” state in our differentiations, we next examined the expression of the “hub” markers SOX8, ITGA4 and SERPINE2 during NC rogression and Schwann induction (Figure 2.2I). In addition to SOX8 expression, NCC2 showed the highest expression of ITGA4 and SERPINE2 among S4 NCCs, while expression of all three markers was homogeneous among S5 NCC subtypes (Figure 2.2I). Interestingly, while S2 NCCs showed moderate to low expression of these markers, we observed a high co-expression of all three markers in a subset of S3 NCCs (Figure 2.2I). Importantly, scoring the dataset published by Adameyko and colleagues[51] for the top 100 markers of S4 NCC2 showed cells in the “hub” and the Schwann cell branch to be the most transcriptionally similar populations (Figure 2.2J). At stage 5, all NCC subtypes, SCPs, Early SCs and SCP derivatives (SCPDs), maintain SOX10, FOXD3, and TFAP2A, as well as gain expression and activity of the key Schwann cell master regulator POU3F1 (OCT6) (Figure 2.1E-F). Taken together, this data suggests that *in vitro* derived NCCs transition through a “hub”-like transcriptional state over the course of Schwann cell differentiation and recapitulate the temporal progression of the NC lineage *in vivo.*

Intriguingly, we found NCC subclusters with expression and activity of the melanocyte master regulator MITF throughout NCC progression (Figure 2.1G). We identified a single melanogenic cluster at S2 (S2 NCC2), two melanogenic clusters at S3 (S2 NCC2 and 3), and one melanogenic cluster at S4 (S4 NCC3) (Figure 2.1G). We validated the emergence of SOX10+/MITF+ cells during NCC progression using immunofluorescence staining (Figure 2.2K-L). Notably, S5 NCC subclusters also showed high MITF expression, however, MITF activity is inhibited likely due to their exposure to the exogenous NRG1 in the Schwann cell culture media which is known to block melanocyte differentiation (Figure 2.1G, 2.2K-L)[269]. The largest subclusters of NCCs during NCC progression, NCC1 of S2, S3 and S4 appear to be uncommitted, showing minimal bias toward specific NC derivatives based on expression or activity of lineage-specific transcription factors (Figure 2.1E-G, 2.2G-H). Taken together, these results indicate that subsets of hPSC-derived NCCs progress toward glial bias/competency but show melanogenic potential throughout NCC progression. This observation falls in line with lineage tracing experiments demonstrating that late migrating NCCs/SCPs also contribute to melanocytes in the skin during development[54]. However, it remains unclear if melanocytes that emerge during NCC progression are transcriptionally or functionally distinct.

2.3.2 Developing NCCs give rise to transcriptionally distinct melanogenic progenitors

We hypothesized that the presence of two S3 NCC subclusters with MITF activity could either represent different levels of melanocyte maturation of the same melanocytic lineage, or the emergence and specification of a distinct melanocytic lineage. We therefore aimed to determine the lineage relationships between NCC subclusters and identify features involved in melanogenic differentiation (Figure 2.3A). We first used Monocle pseudotime analysis[270–272] to predict lineage progression between NCCs at each stage (Figure 2.3B, 2.4A). At D15, uncommitted S2 NCC1 was predicted to transition to melanogenic S2 NCC2. Interestingly at D22, pseudotime predicted a branch point within the uncommitted S3 NCC1 with the melanogenic S3 NCC2 and NCC3 populations at separate ending nodes suggesting divergent specification of these two clusters. Finally, at D30, uncommitted S4 NCC1 is predicted to transition to melanogenic S4 NCC3, as well as gliogenic S4 NCC2, suggesting S4 NCCs retain multipotency towards expected lineages.

As there was only a single melanogenic cluster at D30, we next asked which one of the two melanogenic cluster at D22 was maintained through D30. To answer this, we employed two different methods to identify the most transcriptionally similar NCC subclusters between the S2, S3, and S4 NCC subclusters. First, we again utilized SWNE to create a dimensionally reduced space based on the S3 NCC dataset. We then projected S2 and S4 NCC populations into the S3 NCC space, such that transcriptionally

similar cells would be plotted in the same coordinates (Figure 2.3C). Next, we used separate S3 NCC2 and NCC3 transcriptional signatures consisting of the top 100 most significantly differentially expressed genes of each cluster to module score the NCCs of the S2 and S4 samples (Figure 2.4B). The results from both analyses suggested that the melanogenic S2 NCC2 cluster is closely related to S3 NCC2, while the melanogenic S4 NCC3 cluster was similar to S3 NCC3. Taken together, these data suggest that uncommitted NCCs undergo a temporal transition of differentiating into distinct trajectories of melanogenic progenitors, with S2 NCC2 and S3 NCC2 belonging to trajectory 1 (T1) and S3 NCC3 and S4 NCC3 belonging to trajectory 2 (T2).

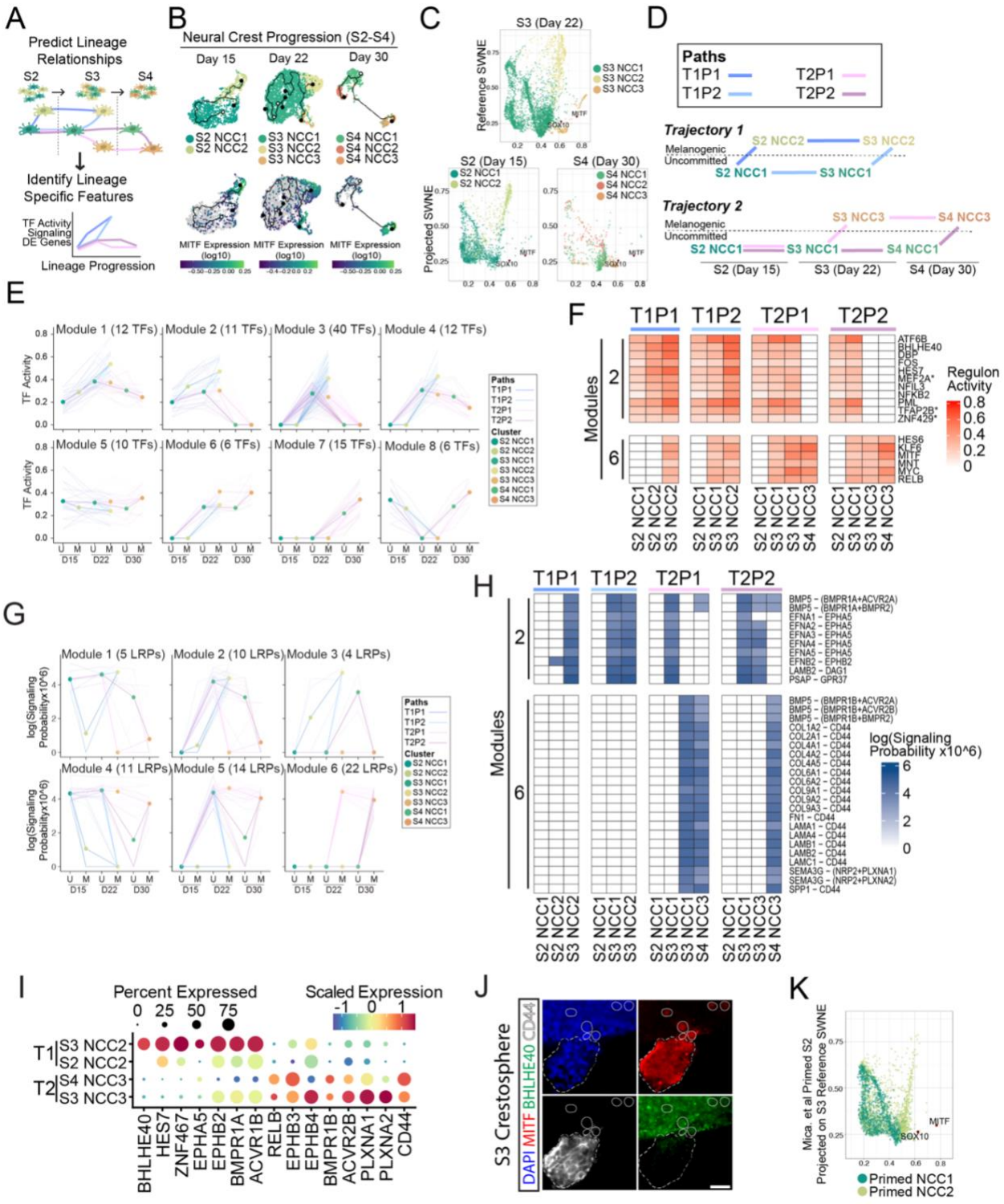

Figure 2.3: Melanogenic NCCs are predicted to emerge in two distinct trajectories
A) Schematic illustration of melanogenic lineage predictions within hPSC-derived NCC populations and their characterization.

B) Top: Pseudotime lineage reconstruction of stage 2-4 neural crest subtypes. Cells (points) are colored by subtype cluster. Black lines follow predicted paths of transcriptional change from selected starting nodes (white circle) to terminal nodes (black circle). Bottom: Log10 MITF expression of stage 2-4 neural crest subtype cells. Grey points represent cells with no detected MITF expression.
C) Projection of stage 2 and stage 4 neural crest subclusters onto the SWNE embeddings of stage 3 neural crest subclusters. Cells (points) with similar SWNE coordinates are transcriptionally similar to one another. SOX10 and MITF are projected in the SWNE embedding to show their influence on the cell embeddings.
D) Proposed model of lineage "paths" as neural crest subtypes commit to one of two melanocyte differentiation "trajectories." Trajectory 1 (top) melanogenic NCCs specify from stage 2 or 3 NCCs, while trajectory 2 (bottom) melanogenic NCCs specify from stage 3 or 4 NCCs. Legend abbreviations: T = Trajectory, P = Path.
E) Predicted activity of transcription factors along the proposed lineage trajectories and paths. Transcription factors were grouped into 8 modules based on similarity in activity patterns. Modules 1-4 contain transcription factors with higher activity in trajectory 1 melanogenic subtypes, while modules 5-8 contain transcription factors with higher activity in trajectory 2 melanogenic subtypes. Lines are colored by path. Points colored by NC subtype represent the average activity of all transcription factors in the module for that subtype with connected opaque lines to show the average activity pattern. Transparent lines show individual activity patterns for all transcription factors in the module.
F) Heatmap of predicted transcription factor activity per stage 2-4 NC subtypes for transcription factor modules 2 and 6. NC subtypes are grouped by proposed lineage path progressions.
G) Predicted activity of ligand receptor pairs along the proposed lineage trajectories and paths. Ligand receptor pairs were grouped into 6 modules based on similarity in activity patterns. Modules 1-3 contain ligand receptor pairs with higher activity in trajectory 1 melanogenic subtypes, while modules 4-6 contain ligand receptor pairs with higher activity in trajectory 2 melanogenic subtypes. Lines are colored by path. Points colored by NC subtype represent the average activity of all ligand receptor pairs in the module for that subtype with connected opaque lines to show the average activity pattern. Transparent lines show individual activity patterns for all ligand receptor pairs in the module.
H) Heatmap of predicted ligand receptor pair activity per stage 2-4 NC subtypes for ligand receptor pair modules 2 and 6. NC subtypes are grouped by proposed lineage path progressions.
I) Scaled expression of trajectory enriched transcription factors and receptors in melanogenic NC subtypes.
J) Expression of MITF (red) with T1 progenitor marker BHLHE40 (green) and T2 progenitor marker CD44 (grey) in stage 3 crestospheres. Scale bars represent 25um.
K) Projection of stage 2 neural crest subclusters differentiated from the protocol described by Mica et al. onto the SWNE embeddings of stage 3 neural crest subclusters. Cells (points) with similar SWNE coordinates are transcriptionally similar to one another. SOX10 and MITF are projected in the SWNE embedding to show their influence on the cell embeddings.

Importantly, the pseudotime data showed the potential for the uncommitted NCCs at each given stage to become melanogenic, and the SWNE data suggests that different melanogenic clusters arise from and progress in distinct trajectories. Thus, we propose a

model where two paths exist for the differentiation of both T1 and T2 melanogenic progenitors in our culture system. Path 1 of T1 differentiation (T1P1) occurs if uncommitted S2 NCC1 cells differentiate to melanogenic S2 NCC2 which continue to mature directly into melanogenic S3 NCC2 cells by the intermediate time point (D22). Path 2 (T1P2) occurs if uncommitted S2 NCC1 cells maintain potency into the intermediate time point as uncommitted S3 NCC1 cells and then commit to the melanogenic S3 NCC2 identity (Figure 2.3D). For T2 progenitors, both paths require the uncommitted S2 NCC1 to remain uncommitted as S3 NCC1. Similar to T1, Path 1 of T2 (T2P1) differentiation occurs if uncommitted S3 NCC1 cells differentiate to melanogenic S3 NCC3 cells at D22, which continue to mature directly to melanogenic S4 NCC3 cells by D30. Path 2 of T2 (T2P2) occurs if uncommitted S3 NCC1 cells stay uncommitted until D30 as S4 NCC1 cells and then commit to the melanogenic S4 NCC3 identity (Figure 2.3D).

Using these predicted differentiation paths, we leveraged SCENIC and CellChat analyses to identify regulons and signaling pathways with differential activities along distinct trajectories. Based on pattern of activity along different paths, transcription factors were grouped into 8 modules (Figure 2.3E-F, 2.4C). Module 2 consists of T1 upregulated regulons including HES7 and BHLHE40, while regulons in module 6 such as RELB were upregulated in T2 (Figure 2.3F). CellChat predicted signaling pathways were grouped into 6 modules (Figure 2.3G-H, 2.4D). Interestingly, signaling pathways known to drive melanogenic differentiation such as BMP were shared between the two trajectories, but their activity was predicted to be mediated by different receptors (Figure 2.3H, 2.4D). For

example, BMP5 was predicted to signal through BMPR1A in T1 (module 2), and BMPR1B in T2 (module 6) (Figure 2.3H). Other pathways in module 6, like CD44 signaling through the ECM, were specific to T2 progenitors (Figure 2.3H). Based on these results, we identified a panel of transcription factors and receptors differentially expressed between T1 and T2 melanogenic progenitors (Figure 2.3I). To validate examples of these T1 and T2 specific markers, we performed immunofluorescent staining and found distinct populations of MITF+ NCCs showing mutually exclusive expression of BHLHE40 and CD44 at D22 (Figure 2.3J). These analyses revealed the emergence of different populations of progenitors with propensity towards melanocyte differentiation during NCC progression. This prompted us to assess their ability to generate fully differentiated and functional melanocytes.

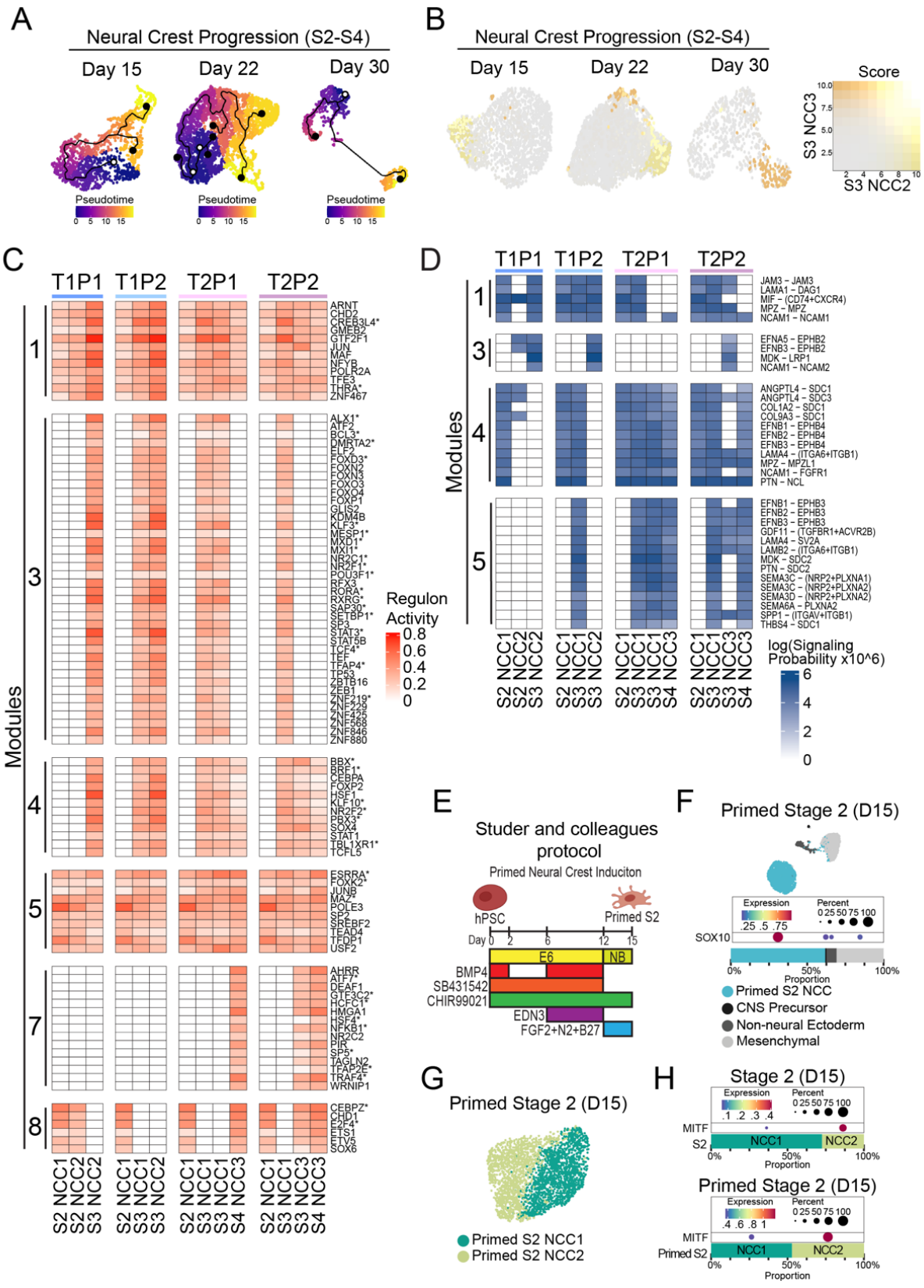
A
Neural Crest Progression (S2-S4)
Day 15
Day 22
Day 30
Pseudotime
B
Neural Crest Progression (S2-S4)
Day 15
Day 22
Day 30
Score
S3 NCC3
S3 NCC2
C
T1P1
T1P2
T2P1
T2P2
Modules
Regulon Activity
S2 NCC1
S2 NCC2
S3 NCC2
S3 NCC1
S3 NCC3
S4 NCC3
D
T1P1
T1P2
T2P1
T2P2
Modules
JAM3 – JAM3
LAMA1 – DAG1
MIF – (CD74+CXCR4)
MPZ – MPZ
NCAM1 – NCAM1
EFNA5 – EPHB2
EFNB3 – EPHB2
MDK – LRP1
NCAM1 – NCAM2
ANGPTL4 – SDC1
ANGPTL4 – SDC3
COL1A2 – SDC1
COL9A3 – SDC1
EFNB1 – EPHB4
EFNB2 – EPHB4
EFNB3 – EPHB4
LAMA4 – (ITGA6+ITGB1)
MPZ – MPZL1
NCAM1 – FGFR1
PTN – NCL
EFNB1 – EPHB3
EFNB2 – EPHB3
EFNB3 – EPHB3
GDF11 – (TGFBR1+ACVR2B)
LAMA4 – SV2A
LAMB2 – (ITGA6+ITGB1)
MDK – SDC2
PTN – SDC2
SEMA3C – (NRP2+PLXNA1)
SEMA3C – (NRP2+PLXNA2)
SEMA3D – (NRP2+PLXNA2)
SEMA6A – PLXNA2
SPP1 – (ITGAV+ITGB1)
THBS4 – SDC1
log(Signaling Probability x10^6)
S2 NCC1
S2 NCC2
S3 NCC2
S3 NCC1
S3 NCC3
S4 NCC3
E
Studer and colleagues protocol
Primed Neural Crest Induciton
hPSC
Primed S2
Day 0 2 6 12 15
E6
NB
BMP4
SB431542
CHIR99021
EDN3
FGF2+N2+B27
F
Primed Stage 2 (D15)
Expression
Percent
SOX10
Proportion
Primed S2 NCC
CNS Precursor
Non-neural Ectoderm
Mesenchymal
G
Primed Stage 2 (D15)
Primed S2 NCC1
Primed S2 NCC2
H
Stage 2 (D15)
Expression
Percent
MITF
S2
NCC1
NCC2
Proportion
Primed Stage 2 (D15)
MITF
Primed S2
NCC1
NCC2
Proportion

Figure 2.4: Distinct melanogenic trajectories show different transcriptional and signaling programs
A) Pseudotime lineage reconstruction of stage 2-4 neural crest subtypes. Cells (points) are colored by pseudotime value. Black lines follow predicted paths of transcriptional change from selected starting nodes (white circle) to terminal nodes (black circle).
B) Feature plots of stage 2-4 NCCs colored by a blended module score for S3 NCC2 (yellow) and S3 NCC3 (orange) respective top 100 marker genes.
C) Heatmap of predicted transcription factor activity per stage 2-4 NC subtypes for transcription factor modules 1, 3, 4, 5, 7, and 8. NC subtypes are grouped by proposed lineage path progressions.
D) Heatmap of predicted ligand receptor pair activity per stage 2-4 NC subtypes for ligand receptor pair modules 1, 3, 4, and 4. NC subtypes are grouped by proposed lineage path progressions.
E) Schematic of directed differentiation protocol published by Studer and colleagues to differentiate human pluripotent stem cells to melanogenic primed stage 2 neural crest cells with defined media conditions. The protocol differs from the previously described protocol due to the addition of BMP4 and EDN3 during days 6-12 of neural crest induction.
F) UMAP embedding, SOX10 expression, cluster proportions, and cluster annotation of the primed stage 2 neural crest induction.
G) UMAP embeddings and subclustering of the primed stage 2 SOX10+ cluster.
H) MITF expression and cluster proportions of stage 2 and primed stage 2 NC subtypes.

Studer and colleagues previously established protocols to generate melanocytes from hPSC-derived NCCs utilizing the addition of exogenous BMP4 and EDN3 during the NCC induction phase to prime the early NCCs for melanocyte differentiation[238,273] (Figure 2.4E). Given the observation that a distinct melanogenic trajectory emerges from prolonged culture of hPSC-derived NCCs, we sought to compare how “primed” NCCs fit into our two-trajectory model. scRNAseq of the primed culture at S2 (D15) showed an altered cellular composition of off-target cell types, most notably a lack of placode and a larger mesenchymal population, while maintaining a similar percentage of SOX10+ NCCs to our S2 sample (Figure 2.4F). Similar to the S2 NCCs (D15), sub-clustering of the primed S2 NCCs revealed two subclusters but with a larger proportion of MITF+ cluster NCC2 (Figure 2.4G-H). Interestingly, when we projected primed S2 NCCs in S3 (D22) NCC SWNE space, we observed an overlap with the uncommitted and T1 melanogenic S3 NCC2 clusters, but not with the T2 progenitor cluster S2 NCC3 (Figure 2.3K). These

analyses suggests that priming increases the induction efficiency of melanogenic NCCs but only produces T1 progenitors. Using the differentiation and maturation conditions described by Studer and colleagues[238,273], we set out to derive melanocytes from T1 and T2 melanogenic NCC progenitors and compare their molecular and functional properties.

2.3.3 Early and late NCCs give rise to transcriptionally and functionally distinct melanocytes

Our two-trajectory progenitor model is compatible with the observations *in vivo* that melanocytes differentiate both from early delaminating NCCs as well as from later delaminating NCCs via the nerve-associated SCP intermediate[54,119]. However, early NCC-derived melanocytes and SCP-derived melanocytes are yet to be molecularly and functionally characterized. In order to compare the two populations in a human *in vitro* system, we first had to establish a new differentiation system for generating melanocytes from SCPs.

To achieve this, we subjected both our S5 cultures and primed S2 cultures to the melanocyte induction media developed by Studer and colleagues (Figure 2.5A). Melanocyte induction of S5 cultures resulted in pigmented cells, here termed T2 melanocytes, which express the canonical melanocyte markers SOX10, MITF, TYR, and PMEL, similar to the melanocytes derived from the primed S2 cultures, here termed T1 melanocytes (Figure 2.5B). Importantly, both protocols were highly efficient, yielding greater than 90% MITF+ cells (Figure 2.6A). The primary function of melanocytes is to

synthesize melanin within specialized organelles called melanosomes and transfer them to surrounding keratinocytes. We confirmed the ability of both T1 and T2 melanocytes to produce fully mature melanosomes using transmission electron microscopy (TEM) (Figure 2.5C). To assess melanosome transfer, we set up co-cultures primary human keratinocytes with either T1 or T2 melanocytes. We performed immunofluorescence and flow cytometry for PMEL, a melanosome transmembrane protein, and confirmed the presence of melanosomes in keratinocytes, indicating their successful transfer from both T1 and T2 melanocytes. However, we did not observe any significant differences in transfer kinetics between the two melanocyte populations (Figure 2.5D, 2.6B).

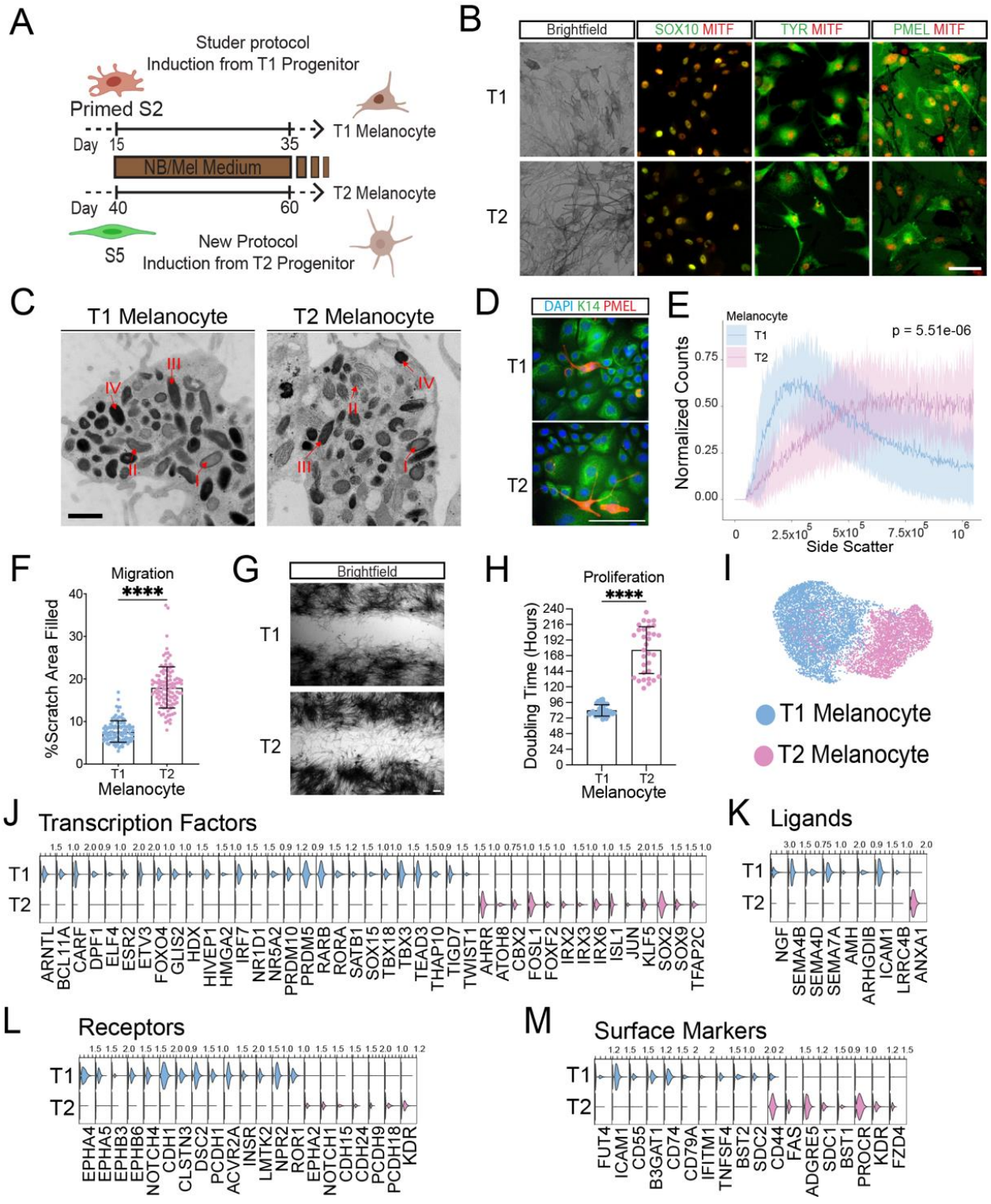

Figure 2.5: Temporally distinct melanogenic NCCs give rise to functionally and molecularly different melanocytes

A) Schematic of the directed differentiation of trajectory 1 and trajectory 2 melanocytes. Both T1 and T2 melanocytes are differentiated using the same defined medium but differ in that T1

melanocyte differentiation is induced from primed S2 NCCs while T2 melanocyte differentiation is induced from primed S5 SCPs.
B) Brightfield images (left) showing pigmentation and immunofluorescent images showing coexpression of MITF (red) with SOX10, TYR and PMEL (green, left to right) in T1 (top) and T2 (bottom) melanocyte cultures. Scale bar represents 100um.
C) Transmission electron micrographs of T1 (left) and T2 (right) melanocytes showing melanosome formation. Examples of melanosomes in different parts of the four stages of melanosome maturation are highlighted with red arrows. Scale bar represents 1um.
D) Co-culture of T1 (left) and T2 (right) melanocytes with primary human keratinocytes showing transfer of PMEL+ melanosomes (red) to K14+ keratinocytes (green). Scale bar represents 100um.
E) Flow cytometry-based quantification of pigmentation via side scatter value. Solid lines show the average distribution of side scatter values with transparent ribbons showing standard deviation (n=12).
F) Quantification of T1 and T2 melanocyte scratch assays. Y axis represents the percentage of the original scratch area now covered by melanocyte cell bodies. Points represent technical replicates from n=3. **** is $p<0.0001$ and error bars represent standard deviation.
G) Representative bright field images of T1 (top) and T2 (bottom) melanocyte scratch assays 72hr after scratch. Scale bar represents 100um.
H) Doubling time analysis of T1 and T2 melanocytes. Points represent technical replicates from n=3. **** is $p<0.0001$ and error bars represent standard deviation.
I) UMAP embedding of merged T1 and T2 melanocyte datasets.
J) Violin plots showing the expression of selected T1 and T2 melanocyte specific transcription factors.
K) Violin plots showing the expression of selected T1 and T2 melanocyte specific secreted ligands.
L) Violin plots showing the expression of selected T1 and T2 melanocyte specific receptors.
M) Violin plots showing the expression of selected T1 and T2 melanocyte specific surface markers.

Interestingly, the quantification of melanin content using flow cytometry and 475nm wavelength absorbance revealed that T2 melanocytes possessed higher pigmentation and melanosome numbers (Figure 2.5E, 2.6C). Scratch assays of T1 and T2 melanocytes revealed that T2 melanocytes are also more migratory than T1 melanocytes (Figure 2.5F-G). However, T1 melanocytes were more proliferative exhibiting a shorter doubling time than T2 melanocytes (Figure 2.5H). These data suggest that while T1 and T2 melanocytes similarly expressed the canonical melanocytic and pigmentation markers, they showed differences in their functional features.

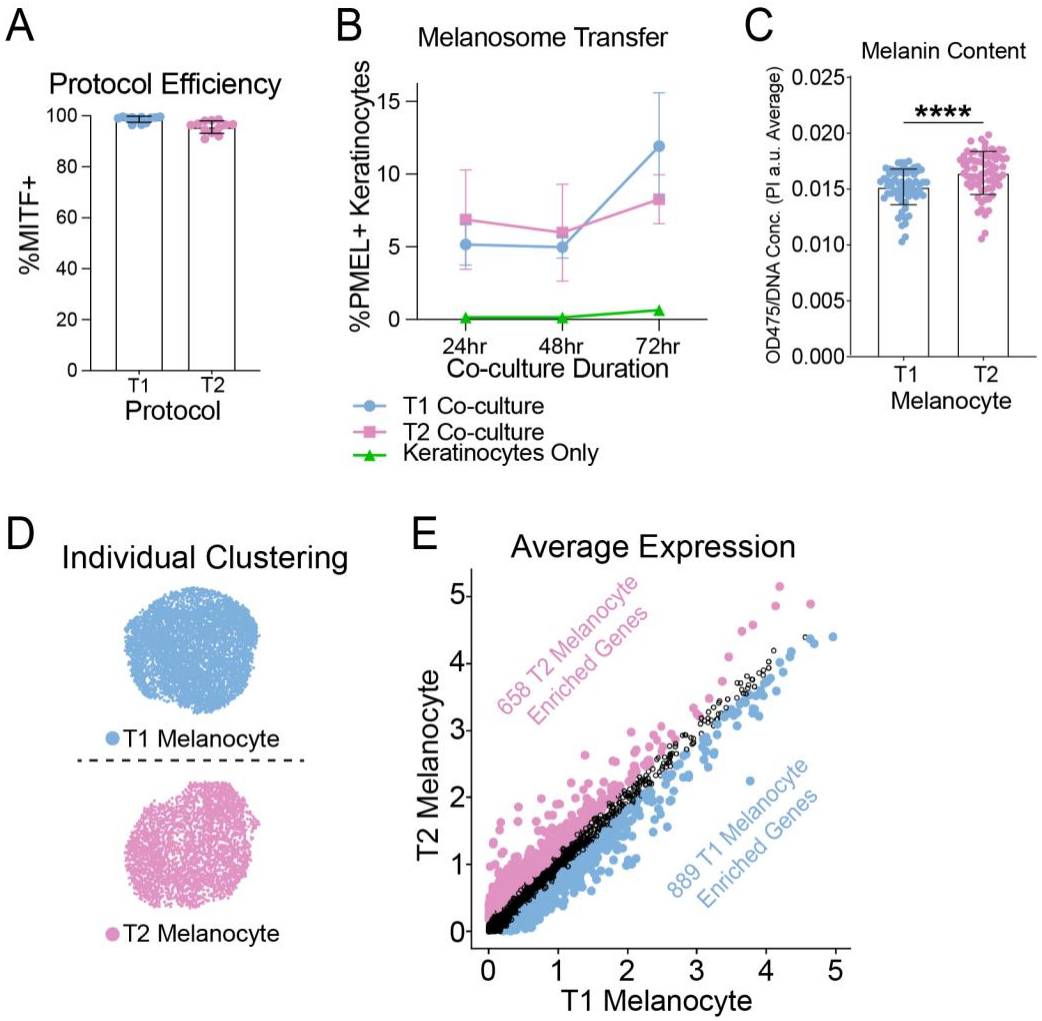

Figure 2.6: T1 and T2 melanocytes have different transcriptional signatures
A) Flow cytometry-based quantification of MITF+ cells resulting from the T1 and T2 melanocyte induction protocols (n=12). Error bars represent standard deviation.
B) Flow cytometry-based quantification of melanosome transfer from T1 or T2 melanocytes to primary keratinocytes after 24, 48 and 72hrs of co-culture or with keratinocytes alone. The y axis represents the percentage of K14+/PMEL+ keratinocytes. Error bars represent standard deviation of individual wells from 3 independent biological replicates.
C) Bulk culture pigmentation quantification based on optical density readings at 475nm normalized to DNA concentration based on propidium iodide fluorescence intensity. Points represent values from individual wells from 3 independent biological replicates. **** is $p<0.0001$ and error bars represent standard deviation.
D) UMAP embeddings of individually analyzed T1 (top) and T2 (bottom) melanocyte datasets.
E) Scatter plot of average expression of all detected genes in T1 and T2 melanocytes. Genes are colored by differential expression where genes in blue are significantly ($p < 0.05$) more highly expressed in T1 melanocytes by > 0.25 fold change while genes in pink are significantly ($p < 0.05$) more highly expressed in T2 melanocytes by > 0.25 fold change. Genes represented by black outlines are not significantly differentially expressed.

Given the functional differences between T1 and T2 melanocytes, we next sought to characterize the underlying transcriptional differences by performing scRNAseq on T1 and T2 melanocytes. The two populations were processed and sequenced in a single batch and were age matched based on the time they were cultured in melanocyte induction media. Analysis of both melanocytes individually revealed very homogenous populations, however, integration of these samples results in minimal overlap indicating they are transcriptionally distinct (Figure 2.6D, 2.5I). Differential gene expression testing indeed revealed 1557 differentially expressed genes, with 658 genes enriched in T2 melanocytes versus 889 genes enriched in T1 melanocytes (Figure 2.6E). Of these DE genes, we identified many transcription factors specific to each population, such as the cell cycle regulators FOXO4 and ETV3 in T1 melanocytes and SOX2, SOX9 and TFAP2C in T2 melanocytes (Figure 2.5J). Interestingly T1 melanocytes exclusively expressed neurogenic factors such as NGF, SEMA4B/D and ICAM1 (Figure 2.5K). Similar to their distinct progenitor stages, T1 and T2 melanocytes expressed unique receptors from the same receptor families, such as EPHA4/5, EPHB3/6, NOTCH4 and CDH1 in T1 melanocytes and EPHA2, NOTCH1 and CDH15/24 in T2 melanocytes (Figure 2.5L). Importantly, many surface markers are also enriched in each melanocyte population, such as CD44 in T2 melanocytes, offering potential tools for their prospective isolation using fluorescence activated cell sorting (FACS) (Figure 2.5M).

2.3.4 Early and late signatures are expressed in different populations of melanocytes *in vivo*

We next sought to leverage published single cell transcriptomics datasets and embryonic mouse tissue to identify the T1 and T2 molecular signatures in primary melanocytes (Figure 2.7A). We first integrated the annotated melanocyte clusters from eight datasets collected from multiple developmental stages and anatomical locations[139,274–280] (Figure 2.8A). Scoring the primary melanocyte dataset with separate T1 and T2 melanocyte transcriptional signatures consisting of their top 100 significantly differentially expressed genes showed that the majority of primary melanocytes score highly for one signature or the other (Figure 2.7B). We annotated the primary melanocytes based on having a higher T1 or T2 melanocyte scoreed and quantified the proportions of T1-like versus T2-like melanocytes in different tissue samples. We found that T1 and T2-like melanocytes were present in all developmental stages (Figure 2.7C). Interestingly, grouping samples by their anatomical location along the anterior-posterior axis suggested an enrichment of T2-like melanocytes in the anterior and T1-like melanocytes in the posterior regions (Figure 2.7C).

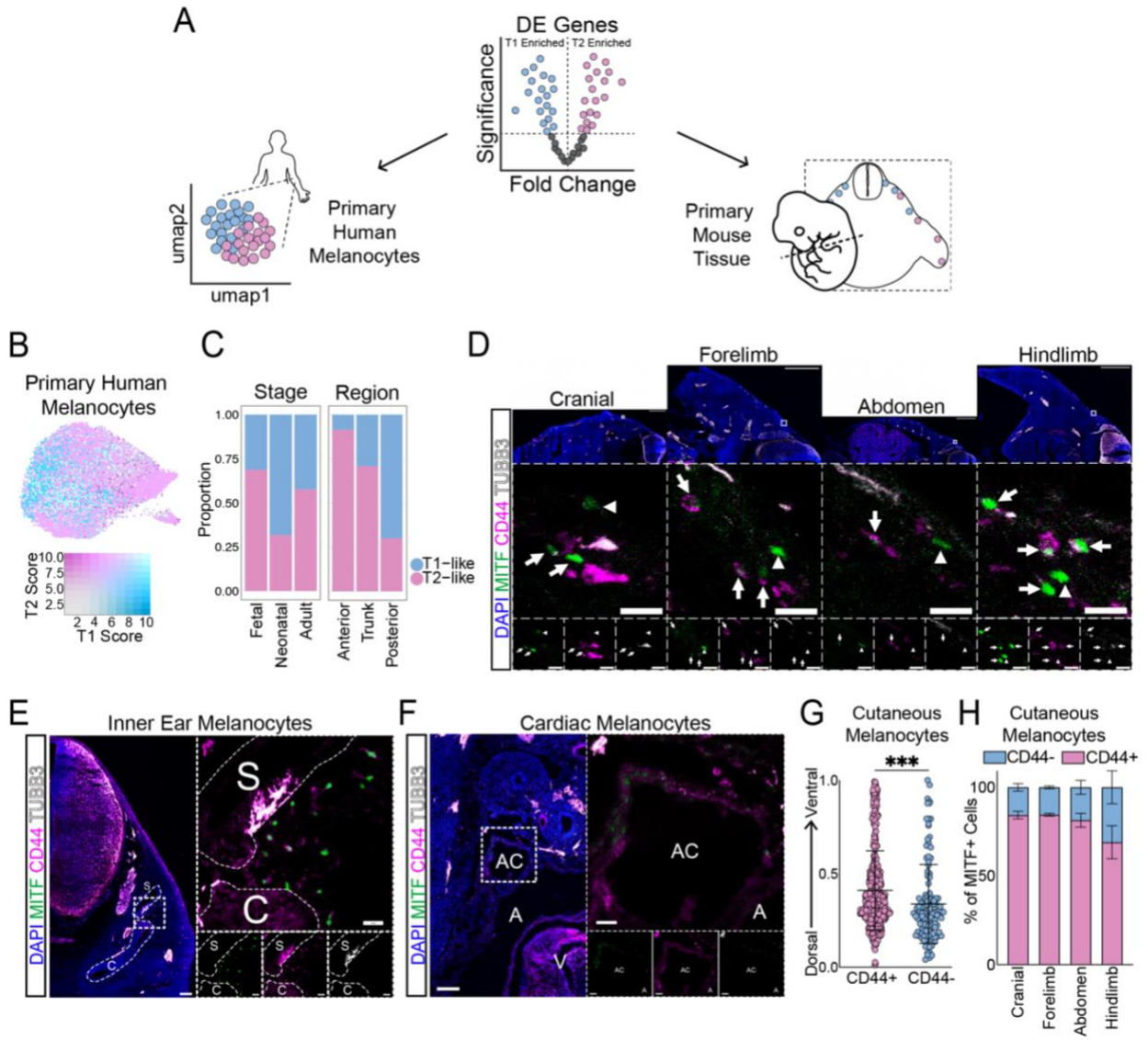

Figure 2.7: Markers of temporally distinct hPSC-derived melanocytes are expressed by different populations of primary mouse and human melanocytes

A) Schematic illustration of validation of T1 and T2 signature marker in human and mouse primary melanocytes.

B) Feature plot of integrated primary melanocytes colored by blended module score for T1 (blue) and T2 (pink) hPSC-derived melanocyte respective top 100 marker genes.

C) Bar plots showing the proportion of T1-like and T2-like primary melanocytes grouped by the developmental stage (left) and anterior to posterior anatomical position (right) of the primary melanocytes.

D) E12.5 mouse cranial, front limb, abdominal and hind limb sections showing nuclei (blue), melanocytes (MITF, green) neurons (TUBB3, grey) and the T2 melanocyte surface marker CD44 (magenta). Arrows point to CD44+ melanocytes and arrowheads point to CD44- melanocytes. Tile scan scale bars represent 500um, zoomed inlay scale bars represent 25um.

E) E12.5 mouse cranial section showing nuclei (blue), melanocytes (MITF, green) neurons (TUBB3, grey) and the T2 melanocyte surface marker CD44 (magenta) around developing inner

ear structures (c = cochlea, s = saccule). Tile scan scale bar represents 100um, zoomed inlay scale bars represent 25um.
F) E12.5 front limb section showing nuclei (blue), melanocytes (MITF, green) neurons (TUBB3, grey) and the T2 melanocyte surface marker CD44 (magenta) in the developing heart (ac = anterior cardinal vein, a = atrium). Tile scan scale bar represents 100um, zoomed inlay scale bars represent 25um.
G) Normalized dorsoventral axis location of CD44- and CD44+ cutaneous melanocytes*** is $p<0.001$ and error bars represent standard deviation. Points represent location values of individual melanocytes across 3 embryos.
H) Bar plots showing the proportion of CD44- and CD44+ cutaneous melanocytes grouped by the anterior to posterior anatomical location in sections. Error bars represent standard deviation across 3 embryos.

Co-staining of MITF with the T2 melanocyte lineage marker CD44 in embryonic day 12.5 mouse cranial, front limb, abdominal and hind limb tissue sections, revealed intermixed populations of CD44+ (T2-like) and CD44- (T1-like) MITF+ cells in all tissue regions (Figure 2.7D, 2.8B). In line with observations from SCP-derived melanocyte lineage tracing, we also observed CD44+ MITF+ cells in extracutaneous regions such as the inner ear and heart (Figure 2.7E-F)[120]. Similar lineage tracing of early NC-derived melanocytes and SCP-derived melanocytes also described a dorsoventral bias, such that SCP-derived melanocytes colonize more ventral tissues[54,119]. Quantification of the relative dorsoventral position of all cutaneous melanocytes across the cranial to hind limb sections similarly showed a significant bias of CD44+ melanocytes to be located more ventral or further from the dorsal neural tube (Figure 2.7G). To validate the observation of the anteroposterior bias observed in the human primary scRNAseq datasets (Figure 2.7C), we similarly quantified the number of cutaneous CD44+/MITF+ and CD44-/MITF+ melanocytes across each region and observed a similar trend of a higher proportion of CD44- (T1-like) melanocytes in more posterior tissue (Figure 2.7H). Taken together, these data provide strong evidence that alternative differentiation trajectories yield distinct melanocyte populations that recapitulate the heterogeneity of melanocytes *in vivo*. Our

finding identifies novel markers that enable the isolation and further characterization of these developmentally distinct populations from both mouse and human tissues.

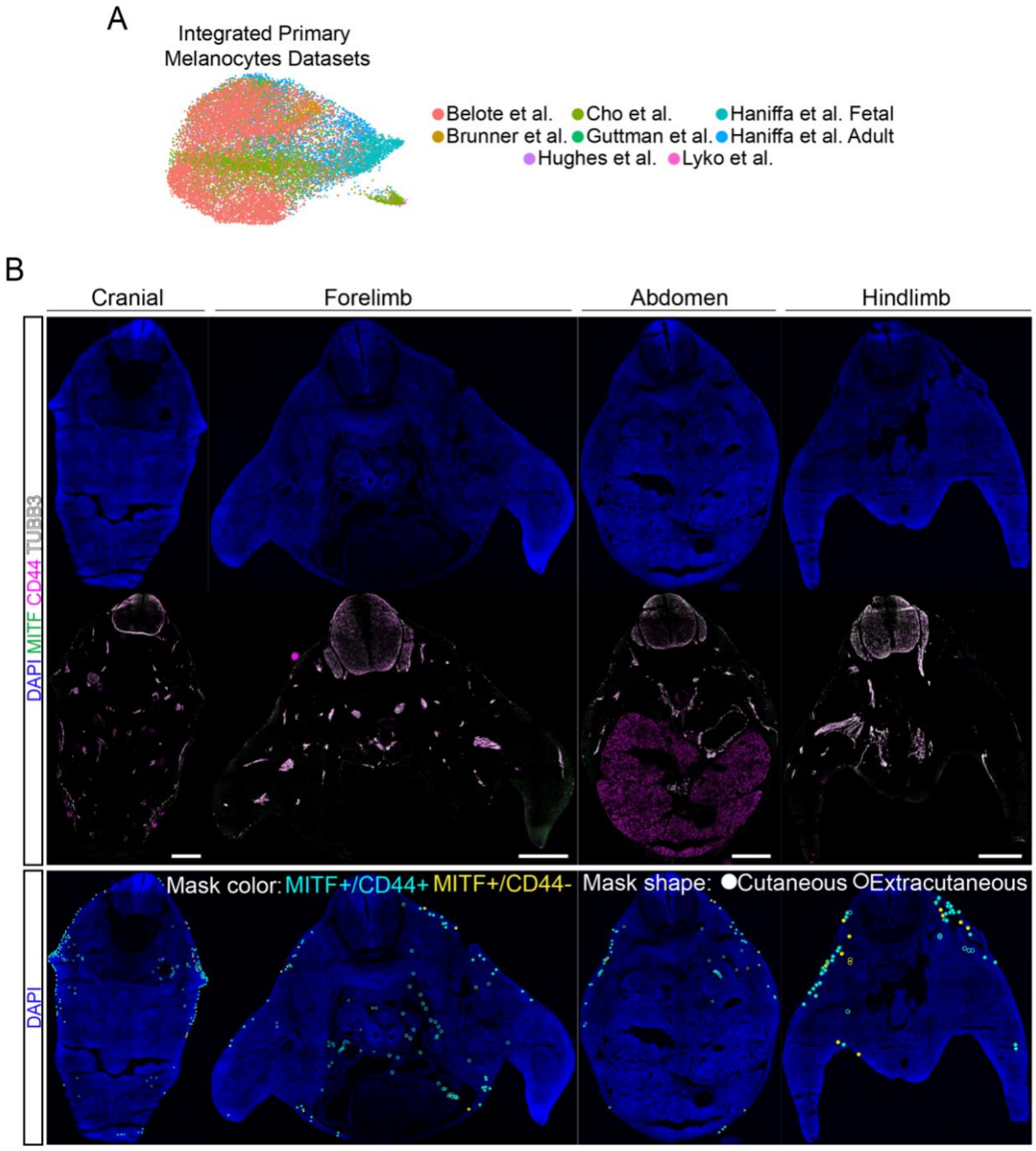

Figure 2.8: Evaluation of T1 and T2 markers in human adult and mouse fetal primary melanocytes

A) UMAP embedding of eight integrated primary human melanocyte datasets colored by the dataset's original publication identifier.

B) Top panel: Representative immunofluorescent images of E12.5 mouse cranial, front limb, abdominal and hind limb sections showing nuclei (blue), melanocytes (MITF, green) neurons (TUBB3, grey) and the T2 melanocyte surface marker CD44 (magenta).

Bottom panel: Representative E12.5 mouse cranial, front limb, abdominal and hind limb sections showing nuclei (blue) and region of interest masks marking all observed MITF+ cells. Masks are colored based on CD44 expression (CD44+ = cyan, CD44- = yellow) and shaped based on anatomical position (closed circle = cutaneous, circle outline = extracutaneous). Scale bars represent 500um.

2.3.5 Signature transcripts of SCP-derived melanocytes promotes metastasis in melanoma

As our data confirmed that T1 and T2 markers were expressed in different subsets of adult melanocytes, we next aimed to understand the implication of the T1 or T2 transcriptional states in melanoma pathogenesis. Based on the functional differences between the two types of melanocytes, we hypothesized that melanomas with a T2-like state may be more migratory and exhibit higher rates of metastasis compared to T1-like melanomas. To test this, we gathered the bulk RNAseq datasets from melanoma samples available on TCGA and used the T1 and T2 melanocyte transcriptional signatures to perform gene set enrichment analysis (GSEA) and identify melanoma samples with significantly enriched or reduced expression of these signatures (Figure 2.9A, 2.10A). We found that the survival probability of patients with a melanoma enriched for the T2 melanocyte signature was significantly lower than patients with a melanoma reduced for this signature (Figure 2.9B, top). Conversely, patients with a melanoma enriched for the T1 signature showed higher survival probability compared to those reduced for the T1 signature, although this difference was not statistically significant (Figure 2.10B). Importantly, direct comparison of patients with a T1-like versus T2-like melanoma showed significantly worse outcomes for T2-like melanoma patients (Figure 2.9B, bottom).

Mortality in melanoma is closely linked to the degree of metastasis. To determine whether T2 melanocyte markers lead to higher metastasis and poor survival, we performed an *in vivo* loss of function screen. For this purpose, we used the MeWo melanoma cell line, which is also significantly enriched for a T2 melanocyte transcriptional signature (Normalized enrichment score = 1.25, adjusted p-value = 0.0018). We used a previously established CRISPR interference (CRISPRi) system[281] for targeted gene knockdowns, employing a pool of guide RNAs (gRNAs) targeting the 100 genes that make up the T2 signature, as well as the 100 T1 genes as a control set. We transduced MeWo cells that constitutively express dCas9-KRAB and luciferase with the gRNA-expressing lentiviruses in a pooled fashion and injected them into the tail veins of NSG (NOD scid gamma) mice for lung colonization assays. At the experimental endpoint, we isolated the melanoma tumors formed in lungs and sequenced their genomic DNA to determine their gRNA pool. We compared the gRNA abundance in the tumors with transduced MeWo cells grown in parallel *in vitro*, reasoning that any gRNA significantly depleted in the melanoma tumors *in vivo* is likely to target a gene essential for the metastatic process (Figure 2.9C). In total, gRNAs targeting 39 genes were significantly depleted in lung tumors, of which 66% targeted T2 signature genes (Figure 2.10C-D).

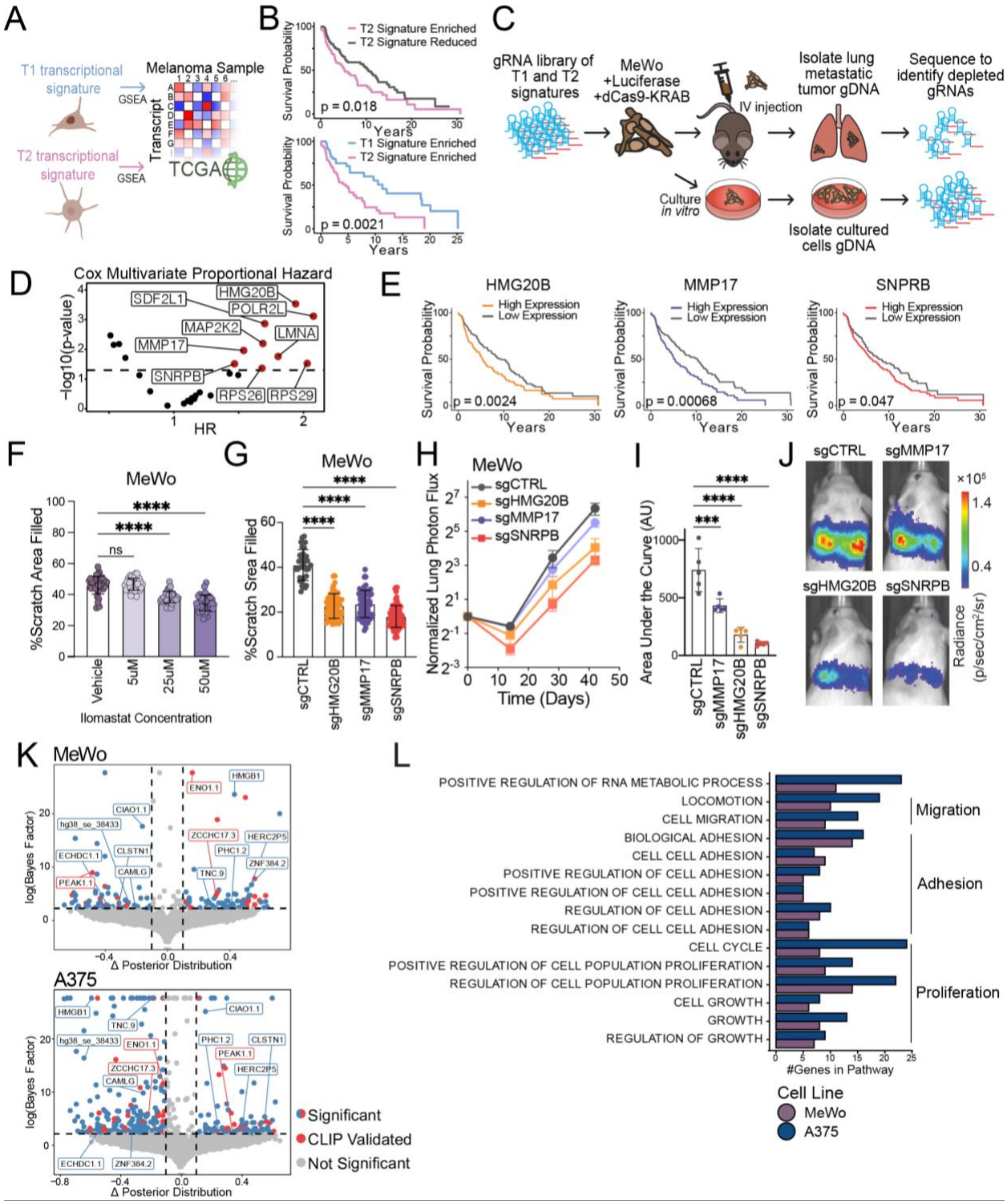

Figure 2.9: Transcripts enriched in SCP-derived melanocytes promote migration and metastasis in melanoma

A.) Schematic illustration of the analysis of 427 melanoma Bulk RNAseq samples from the cancer genome atlas to identify melanomas enriched for T1 and T2 melanocyte transcriptional signatures.

B) Top: Survival curves of melanoma patients with melanomas significantly enriched (pink) versus significantly reduced (grey) for the expression of the top 100 T2 melanocyte markers. Bottom: Survival curves of melanoma patients with melanomas significantly enriched for the expression of the top 100 T1 melanocyte markers (blue) versus significantly enriched for the expression of the top 100 T2 melanocyte markers (pink).
C) Schematic illustration of the CRISPRi screen for identification of T1 and T2 melanocyte marker genes involved in melanoma metastasis.
D) Volcano plot of multivariate Cox proportional hazard ratios versus p-values for CRISPRi hit genes from TCGA melanoma samples.
E) Survival curves of melanoma patients with melanomas that highly (colored) versus lowly (gray) express the nominated CRIPSRi hit gene.
F) Scratch assay quantification of MeWo cells treated with increasing concentrations of the MMP inhibitor ilamostat. Points represent values from individual wells from 3 independent biological replicates. p-values are: **** $p<0.0001$, ns not significant. Error bars represent standard deviation.
G) Scratch assay quantification of CRIPSRi MeWo cells transduced with gRNAs targeting the nominated genes versus a non-targeting control. Points represent values from individual wells from 3 independent biological replicates for 2 unique gRNAs. **** is $p<0.0001$ and error bars represent standard deviation.
H) Quantification of luciferase reporter radiance time course in lungs of mice tail vein-injected with CRIPSRi MeWo cells transduced with gRNAs targeting the nominated genes versus a non-targeting control (n=5). Error bars represent standard deviation from 5 independent biological replicates.
I) Area under the curve of luciferase-based lung colonization quantification of *in vivo* tail vein-injected MeWo cells transduced with gRNAs targeting the nominated genes and a non-targeting control for 5 independent biological replicates. p-values are: *** $p<0.001$, **** $p<0.0001$ and error bars represent standard deviation.
J) Representative endpoint images of luciferase reporter radiance in mice tail vein-injected with CRIPSRi MeWo cells transduced with gRNAs targeting the nominated genes versus a non-targeting control.
K) Volcano plot of differential splicing analysis between MeWo SNRPB KD cells and Control MeWo cells (top) and between A375 SNRPB KD cells and Control A375 cells (bottom). Solid points are significantly different splicing events (bayes factor >10, difference > .1 or <-.1). Red points are previously validated SNRPB bound transcripts in HEK293T cells.
L) Gene Ontology Enrichment analysis of significantly differentially spliced genes in MeWo and A375 SNRPB KD and controls shows enrichment of pathways related to migration and proliferation.

To prioritize genes for further characterization, we utilized the TCGA melanoma datasets to filter hits in two steps. We performed a multivariate Cox proportional hazard test which first determined whether the hit gene's expression level predicted a significant difference in survival probability. Then, we considered additional variables such as patient age, treatments received and stage at diagnosis to determine if the difference in survival probability based on the gene's expression levels remained significant. Nine genes

passed the criteria, and of these we selected HMG20B, MMP17, and SNRPB for further validation experiments (Figure 2.9D-E). While HMG20B and MMP17 have been shown to be highly expressed in melanomas[282], they have never directly been implicated in melanoma metastasis. However, both HMG20B, MMP17 and other members of these gene families have been implicated in metastasis in other cancers[283–290]. Similarly, SNRPB, a canonical subunit of the spliceosome, has not previously been identified as a melanoma risk factor, but has been implicated in the metastatic process of other cancers like glioblastoma, cervical and non-small cell lung cancer[291–293].

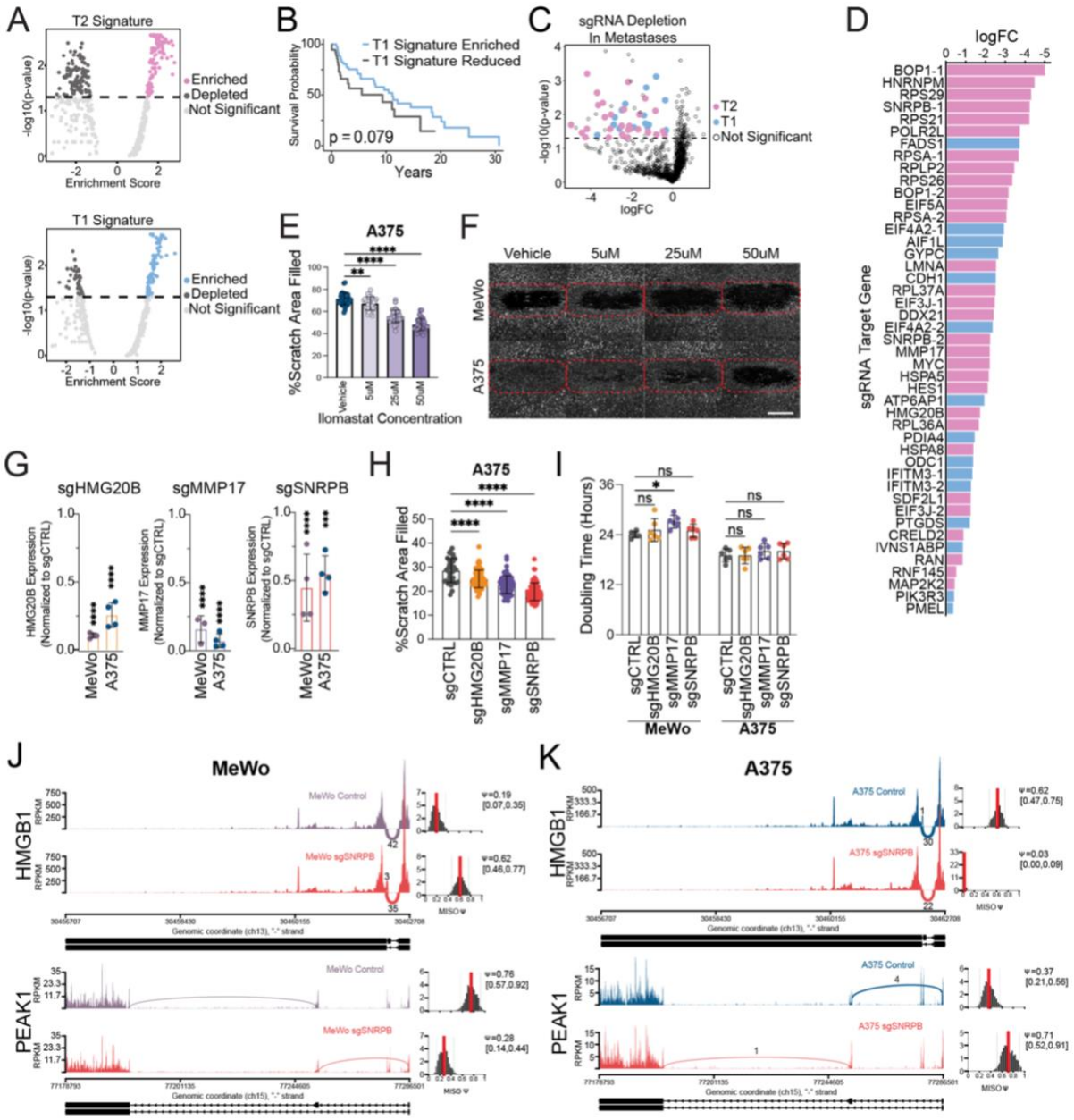

Figure 2.10: Functional roles of T1 and T2 melanocyte markers in melanoma

A) Gene set enrichment analysis of 471 Bulk RNAseq melanoma samples for the respective top 100 T2 (top) and T1 (bottom) marker genes. Melanoma samples are colored by their significant enrichment (pink/blue) or reduction (dark gray) for the gene sets, or light gray for non-significant.

B) Survival curves of melanoma patients with melanomas significantly enriched (blue) versus significantly reduced (grey) for the expression of the top 100 T1 melanocyte markers.

C) Volcano plot of gRNA enrichment or depletion in sequenced lung metastases compared to the culture prior to injection. gRNAs labeled in color are significantly depleted in the lung metastases but not significantly depleted the *in vitro* cultured pool.

D) Bar chart of fold change of significantly depleted gRNAs in lung metastasis compared to starting abundance. Bars are colored by gRNA target of a T1 marker gene (blue) or T2 marker gene (pink).
E) Scratch assay quantification of A375 cells treated with increasing concentrations of the MMP inhibitor ilamostat. Points represent values from individual wells from 3 independent biological replicates. p-values are: ** p<0.01, **** p<0.0001 and error bars represent standard deviation.
F) Representative images of scratch assays of MeWo (top) and A375 (bottom) cells treated with increasing concentrations of the MMP inhibitor ilamostat. Scale bar represents 1000um.
G) qPCR determined fold change expression of CRISPRi hit genes in stable MeWo and A375 KD lines after CRISPRi targeting normalized to non-targeting gene expression. p-values are: *** p<0.001, **** p<0.0001 and error bars represent standard deviation. Points represent values from 2 independent biological replicates for 2 unique gRNAs.
H) Scratch assay quantification of CRIPSRi A375 cells transduced with gRNAs targeting the nominated genes versus a non-targeting control. Points represent values from individual wells from 3 independent biological replicates for 2 unique gRNAs. **** p<0.0001 and error bars represent standard deviation.
I) Doubling rate analysis of CRISPRi MeWo and A375 cells transduced with gRNAs targeting the nominated genes versus a non-targeting control. Points represent values from 3 independent biological replicates for 2 unique gRNAs. p-values are: * p<0.05, ns not significant and error bars represent standard deviation.
J) Sashimi plots showing the differential splicing patterns of migration related genes HMGB1 and PEAK1 in non-targeted versus SNRPB KD MeWO melanoma cell lines.
K) Sashimi plots showing the differential splicing patterns of migration related genes HMGB1 and PEAK1 in non-targeted versus SNRPB KD A375 melanoma cell lines.

To validate the role of these genes in melanoma metastasis we used a combination of genetic and pharmacological approaches in both the MeWo and A375 cell lines. A375 is another melanoma cell line enriched for the T2 signature (Normalized enrichment score = 1.33, adjusted p-value = 1.99e-05). MMPs are a druggable protein family, and MMP17 is a predicted target of the broad spectrum MMP inhibitor ilamostat. Scratch assays of MeWo and A375 cells treated with increasing concentrations of ilamostat showed a dose dependent decrease in cell migration highlighting the promigratory role of MMPs (Figure 2.9F and 2.10E-F). We next generated stable knockdown cell lines using CRISPRi, targeting HMG20B, MMP17 and SNRPB in both MeWo and A375 cells to evaluate the effect on migration and proliferation (Figure 2.10G). Knockdown of all three genes significantly decreased cell migration, while only knockdown of MMP17 in MeWo cells

significantly increased the doubling rate by 3 hours (Figure 2.9G, 2.10H-I). Importantly, tail vein injections of MeWo cell lines with stable knockdown of all three genes showed a significant reduction in formation of lung tumors (Figure 2.9H-J). Notably, the effect sizes of the lung colonization assay matched with the effect size of the *in vitro* migration assay.

As the knockdown of the splicing factor SNRPB resulted in the greatest delay in lung colonization *in vivo* (Figure 2.9H-J), we next sought to determine the spliceosome network regulated by SNRPB in melanoma. We performed paired end bulk RNAseq on control and SNRPB knockdown MeWo and A375 cells to identify differentially spliced transcripts. Interestingly, only 13 transcripts were identified as shared differential splicing events in both MeWo and A375 SNRPB knockdown cells (Figure 2.9K). Notably, many unique differential splicing events were validated as SNRPB targets in a CLIP dataset generated in HEK293T cells (Figure 2.9K). Intriguingly, some of the differentially spliced transcripts in both MeWo and A375, such as HMGB1 and PEAK1, showed opposite trends in transcript isoform abundance (Figure 2.10K-L). Importantly, despite the minimal overlap in differentially spliced transcripts, gene ontology analysis of all differentially spliced genes in both the MeWo and A375 lines revealed that these genes belong to many shared biological process pathways relevant to cell migration, adhesion and proliferation (Figure 2.9L). Taken together, these data suggest that both the transcript targets of SNRPB and the isoform prevalence altered by SNRPB were cell line specific. However, in a melanoma background SNRPB collectively influenced metastasis through the alternative splicing of transcripts involved in migration, adhesion and proliferation.

2.4 Tables

Table 2.1 Antibodies and dilutions used for immunofluorescent staining

antibody	Host Species	dilution	vendor	cat#
SOX10	Mouse	1:500	Proteintech	66786-1-Ig
MITF	Goat	1:100	R&D Systems	AF5769
CKIT	Mouse	1:100	Abcam	ab216450
CD44	Mouse	1:500	Cell Signaling	156-3C11
CD44-AF647	Rat	1:500	Biolegends	103018
BHLHE40	Rabbit	1:500	Novus Biologicals	NB100-1800
TYR	Rabbit	1:100	Abcam	ab180753
PMEL	Mouse	1:200	Fisher Scientific	MA5-13232
K14	Mouse	1:100	Fisher Scientific	MA5-11599
TUBB3	Rabbit	1:500	Biolegends	PRB-435P

Table 2.2 scRNAseq dataset quality control filtering metrics

Dataset	nFeatures greater than	nFeatures less than	nCounts greater than
D6	1500	6000	4500
D15	1500	7500	6000
D22	1500	6000	6000
D30	1500	6000	6000
D40	1500	6000	6000
primed_D15	1500	6000	5000
D35_T1mel	2000	6500	7000
D60_T2mel	3000	7000	8000

Table 2.3 scRNAseq dataset clustering parameters

Dataset	Subset	Integration Method	# PCs (SNN and UMAP)	# PCs (Monocle3 Preprocessing)	Clustering Resolution	Cluster(s) removed and re-clustered? (Reason)
D6	N/A	N/A	17	45	0.2	N/A
D6	SOX10+	N/A	26	N/A	0.2	N/A
D15	N/A	N/A	25	N/A	0.2	N/A
D15	SOX10+	N/A	36	23	0.2	cluster 2 (trigeminal markers)
D22	N/A	N/A	19	N/A	0.15	
D22	SOX10+	N/A	17	13	0.15	at resolution 0.1: cluster 2 (trigeminal markers), cluster 4 (mesenchymal markers)
D30	N/A	N/A	15		0.1	N/A
D30	SOX10+	N/A	17	23	0.2	N/A
D40	N/A	N/A	15	N/A	0.1	N/A
D40	SOX10+	N/A	13	N/A	0.15	N/A
Primed D15	N/A	N/A	19	N/A	0.2	N/A
Primed D15	SOX10+	N/A	13	N/A	0.3	cluster 4 (mesenchymal markers)
D35 T1mel	N/A	N/A	14	N/A	0.2	N/A
D60 T2mel	N/A	N/A	17	N/A	0.2	N/A
T1_T2 merged	N/A	N/A	14	N/A	0.1	N/A
Integrated Primary Datasets	Healthy Melanocytes	MNN	30	N/A	0.1	N/A

Table 2.4 Cluster transcriptional signature used for module scoring

S3 NCC2	S3 NCC3	S4 NCC2	T1 Mel	T2 Mel
ALDOA	NSG1	CD74	PTGDS	LGALS1
P4HA1	BIK	RASL11B	PAEP	S100B
BNIP3	GPNMB	MIA	CAPG	HMG20B
SLC16A3	DCT	COL9A3	DENND2A	UBE2S
PGK1	DUSP10	PTN	SERPINF1	LGALS3
FAM162A	UPP1	APLP1	NMRK2	TUBB3
PGAM1	PHLDA2	LEF1	PTTG1IP	MFSD12
ENO1	ANXA2	PLEKHA4	SPP1	SDF2L1
DDIT4	CD63	POMC	UCHL1	HERPUD1
C4orf3	PTHLH	COL2A1	AKAP12	RPL22L1
LDHA	NPL	CRIP1	MALAT1	PDIA4
ALDOC	S100A11	CST3	SPTBN1	TUBB4B
PFKFB4	MLANA	BGN	RBP1	SLIRP
GAPDH	ECM1	GAPDH	DCT	PPP1R14B
TPI1	CAV2	ALDH1A1	IDH1	RPS21
AK4	PMEL	PRDX2	HTRA3	BCYRN1
SLC44A2	PDLIM3	YWHAQ	MITF	MANF
PPDPF	CAV1	MMP2	ITM2B	MAP2K2
MTFP1	NEAT1	NET1	PMEL	RPS29
ADM	MITF	KLK6	DUSP23	EIF5A
VIM	MFSD12	DANCR	EMP1	CALR
BHLHE40	MAFB	HAPLN1	CTSB	IFITM3
ETFB	GADD45B	S100A10	MLANA	LMNA
MIF	RAB32	SMOC1	RAB38	LRRC59
NAMPT	PCDH7	MAOB	PLP1	SNHG5
WSB1	TUBB2A	SPP1	CTNNB1	UBE2M
STC1	RAB5C	LSR	SMIM1	ANXA2
SLC2A3	CTGF	COL9A2	BNIP3	SRM
PDK1	PHLDA1	HAS2	SEMA5A	HSPA8
GPI	ANXA5	WFIKKN1	TAX1BP1	TSPO
SLC2A1	KLF6	ZFP36L2	TMSB4X	ATOX1
PRELP	SDCBP	OC90	STMN1	RNF145
FKBP4	ATP6V0C	COL12A1	RXRG	CRELD2
C1orf54	ZC3H13	ARL6IP5	VAMP8	TUBA1B
ENO2	ATP6V0B	TMSB4X	APOC1	RPL38
HES7	MYL12A	RGS10	BHLHE41	DUSP4
ANKRD37	ARPC2	TPD52L1	FSTL1	POLR2L
VKORC1	APOE	CBLN1	MAGEH1	NQO1
PRDX6	EIF1	PRSS33	LINC00998	PHLDA2

S3 NCC2	S3 NCC3	S4 NCC2	T1 Mel	T2 Mel
RAB3A	SQSTM1	GCNT1	COL18A1	FTL
H3F3B	VAT1	CUEDC2	GSTP1	DDX39A
HK2	LRPAP1	ODC1	TM7SF2	AHNAK
EFNA3	TUBA1C	PCBP4	PSMB10	NPAS1
RRAGD	LMNA	BMP7	CD68	RPL37A
DUSP15	EMP3	ID3	TTC3	TUBB6
MIR210HG	SOCS6	CXCR4	UGCG	FXYD5
MAD2L2	PSMA7	TFAP2B	ACSL3	PCMT1
SEC61G	MLLT11	C1QTNF4	SERPINB9	ACTB
PDE4C	IRS2	SERPINF1	GAPLINC	RPS26
ERO1A	COX7A2	SERPINE2	APOE	RPSA
CCNG2	TMSB10	NKX2-5	RGCC	LINC00152
STC2	ARHGDIA	EGR2	IVNS1ABP	SLC7A8
UNC119	HMG20B	PLS3	ASAH1	SNHG25
BNIP3L	ACP5	POSTN	TRPM1	HSPA5
PKM	TMSB4X	NOVA1	GYPC	OSGIN1
ESPN	CALM1	TM7SF2	ANXA5	DDX21
SLC29A1	PSAP	ADD3	NME4	MTDH
TSC22D4	SNAI2	GJB1	SERPINE2	MIR4435-2HG
INSIG2	RAB7A	LTBP4	PTGES	NOP16
PCLO	PHACTR1	RXRG	MYH10	RPLP2
POLR2H	MYL6	IGFBP2	C21orf91	DANCR
GUK1	ATP1A1	HMGA2	SEPP1	RPL37
MALAT1	CAPN3	RCN2	AIF1L	RAN
SPAG4	MGAT1	RARRES2	IFI16	TOMM7
VAMP2	STX3	OCIAD2	PLEKHA5	EIF3J
IGFBP2	VIM	MGLL	UQCRB	CD44
NXPH4	TNFRSF12A	HEY2	CST3	TOMM40
EIF4A2	AP1S2	PLD3	ISYNA1	RPSAP58
TET1	CTSC	LINC00173	ZNF106	NHP2
HMGB2	TUBB3	HMGN1	UBL3	NEFL
PLCD1	PAX3	ITPR3	ATP6AP1	PTMS
TUBB2B	MIR22HG	DHCR7	NREP	SERP1
BTG1	UBL3	CPE	MET	RPS27
H1F0	MYC	COL9A1	FCRLA	ZNF593
EMD	S100A10	LRRN3	PTP4A1	HN1
DRAXIN	ABL2	BSG	SEP7	HNRNPM
TRPM4	ATP6V1D	ACTG1	C4orf3	HES1
P4HA2	CLIC1	RCN1	EIF4A2	ADRM1
NUDT16	SH3BGRL3	GJC3	ODC1	NPM3

S3 NCC2	S3 NCC3	S4 NCC2	T1 Mel	T2 Mel
NDUFA4L2	GADD45A	GPX4	NARS2	MMP17
GBE1	PRKCDBP	ISYNA1	PSIP1	BOP1
WDR54	SNCA	MSTN	ST6GALNAC2	MYDGF
NPC2	USMG5	PLEKHB1	DAB2	PGP
DCXR	TUBB4A	KIRREL2	CHST9	NMT1
TXNIP	COX6A1	PGD	CLU	C20orf27
KDM3A	RCAN1	XPNPEP1	RAB13	SRSF2
SLC3A2	LYPD1	COL26A1	BCAN	CCDC85B
PDK3	VGF	LMO3	GABARAPL2	SNRPB
DDX41	ATF3	CAV1	GBAS	BRI3
NEAT1	RAB38	LGALS1	ARRDC4	MRPS12
ATRAID	MID1	TSN	FAM210B	SNHG6
TMEM45A	PFN1	DACH1	PIK3R3	MYC
CIRBP	POMP	MEST	LUM	CFL1
COL11A1	CDKN1A	ARPC1B	NDUFA5	RPL35
DPF1	ATP5B	LITAF	OSBPL8	SNHG9
RNF181	ATP6V1G1	NR2F2	ADAM10	CDKN1A
CIB1	FABP5	GSN	BLOC1S1	NME1
ADGRG1	CYSTM1	ETV4	GCHFR	GIPC1
ARRDC3	FTH1	MEF2C	TBC1D7	HMOX1
NEU1	NRP2	ZEB2	FADS1	RPL36A

Table 2.5 Primers and oligo sequences used in CRISPRi experiments

qPCR Primers	
Oligo Name	**Sequence**
ST3GAL4 qPCR Fwd	GATCACGCTCAAGTCCATGG
ST3GAL4 qPCR Rev	CTTGCCCAGGTCAGAAGGA
GAPDH qPCR Fwd	GTCTCCTCTGACTTCAACAGCG
GAPDH qPCR Rev	ACCACCCTGTTGCTGTAGCCAA
HMG20B qPCR Fwd	CACTCTCCTGAATGGACACAAGG
HMG20B qPCR Rev	GCCACATTCATCTTCCGCAAGC
MMP17 qPCR Fwd	CACCAAGTGGAACAAGAGGAACC
MMP17 qPCR Rev	GCAATGTCGCTCCAGACCTTGA
SNRPB qPCR Fwd	TTGGCACCTTCAAGGCTTTTGAC
SNRPB qPCR Rev	AGACCGAGGACTCGCTTCTCTT
CRISPRi Screen Library Prep	
Oligo Name	**Sequence**
oPool 5' sequence added to protospacer	ATTTTGCCCCTGGTTCTTCCACCTTGTTG
oPool 3' sequence added to protospacer	GTTTAAGAGCTAAGCTGCCAGTTCATTTCTTAGGG
UMI-tag	CTCTTTCCCTACACGACGCTCTTCCGATCTNNNNNNcttg (where NNNNNN is UMI)
PCR Fwd	AATGATACGGCGACCACCGAGATCTacactctttccctacacgacgctc
PCR Rev	CAAGCAGAAGACGGCATACGAGATNNNNNNGTGACTGGAG TTCAGACGTGTGCTCTTCCGATcgactcggtgccacttttc (where NNNNNN is the sample index)
gRNAs for stable knockdown line generation	
Oligo Name	**Sequence**
sgST3GAL4	TCCCTTGGAGAACCACCTTGTTGGGGCGCGACGGCTCGAC TCGGCGTTTAAGAGCTAAGCTGGAAACAGCATAGCAAG
sgNonTargeting	TCCCTTGGAGAACCACCTTGTTGGGCGCCAAACGTGCCCTG ACGGGTTTAAGAGCTAAGCTGGAAACAGCATAGCAAG
HMG20B_-_3573028.23-P1	TCCCTTGGAGAACCACCTTGTTGGGAACTCCGGGCCCTGA GAGGTTTAAGAGCTAAGCTGGAAACAGCATAGCAAG
HMG20B_-_3573204.23-P1	TCCCTTGGAGAACCACCTTGTTGGCTCCGGGCCCGGCATC CCGGTTTAAGAGCTAAGCTGGAAACAGCATAGCAAG
MMP17_-_132312997.23-P1P2	TCCCTTGGAGAACCACCTTGTTGGCTGCGGAACGCGAAGC GGAGTTTAAGAGCTAAGCTGGAAACAGCATAGCAAG
MMP17_-_132313145.23-P1P2	TCCCTTGGAGAACCACCTTGTTGGTGGCGCTGGGGACCCG CGGGTTTAAGAGCTAAGCTGGAAACAGCATAGCAAG
SNRPB_+_2451332.23-P1P2	TCCCTTGGAGAACCACCTTGTTGGGCCATCAGAACCGCCAC CAGTTTAAGAGCTAAGCTGGAAACAGCATAGCAAG
SNRPB_+_2451365.23-P1P2	TCCCTTGGAGAACCACCTTGTTGGGCCTCTGAGGAGGCGA ATCGTTTAAGAGCTAAGCTGGAAACAGCATAGCAAG

2.5 Methods

Maintenance and passaging of human pluripotent stem cells (hPSCs)

The H9 human embryonic stem cell (hESC) line was maintained on Geltrex (Gibco) coated plates in chemically defined media (Essential 8, Gibco) at 37°C 5% CO_2. Stem cell media was changed every other day and stem cell colonies were passaged at ~70% confluency using EDTA (Corning) to dissociate. Stem cell maintenance cultures were tested for mycoplasma contamination once a month.

Maintenance and passaging of melanoma cell lines

MeWo cells were grown in EMEM (Lonza) supplemented with 10% FBS (ScienCell), penicillin and streptomycin (Gibco) and amphotericin B (Gibco). A375 cells were grown in DMEM supplemented with 10% FBS, penicillin, streptomycin and amphotericin B. Media was changed every other day and cultures were passaged at 90% confluency using 0.05% Trypsin (Corning). Cultures were tested for mycoplasma contamination once a month.

Cranial neural crest induction from hPSCs

hESC cultures at ~70% confluence were dissociated using EDTA and replated one to one on Geltrex coated plates in stem cell media (Essential 8) to establish an hESC monolayer. The following day, cranial neural crest induction was initiated (D0) by replacement of the stem cell maintenance media with neural crest induction media A (Essential 6 base medium (Gibco), 600nM CHIR99021 (Biogems), 10uM SB431542 (Selleckchem), and

1ng/ml BMP4 (R&D Systems)). On days 2, 4, 6, 8, and 10 of cranial neural crest induction cultures are fed with neural crest induction media B (Essential 6 base medium, 1.5uM CHIR99021, 10uM SB431542). On day 12, cranial neural crest induction cultures are dissociated with Accutase (Innovative Cell Technologies) for 20min, at 37°C with 5% CO_2, pelleted at 300xg for 2min, resuspended in neural crest maintenance media (NC-C) (Neurobasal base medium (Gibco), 20ul/ml B27 supplement (Gibco), 10ul/ml N2 supplement (Gibco), 10ul/ml Glutagro (Corning), 10ul/ml MEM NEAAs (Corning), 3uM CHIR99021 and 10ng/ml FGF2 (R&D Systems)) and plated in ultra-low-attachment plates (Corning). This culture format selects against contaminating ectodermal lineages that arise during the neural crest induction and maintains neural crest cells in 3D crestospheres. On days 14, 18, 22, and 26 the crestospheres are fed with fresh NC-C media by gently swirling the plate on a flat surface to collect the spheres in the center of the well, aspirating the spent media carefully from the edges of the well without removing the crestospheres and replacing with fresh NC-C. To prevent spontaneous differentiation in the center of the crestopsheres, crestosphere cultures are passaged on days 16, 20, 24 and 28. The crestopsheres are collected and centrifuged at 300xg for 1min and resuspended in Accutase. Incubation time in Accutase starts with 15min on D16 and increases by 5min each dissociation day as neural crest maintenance progresses to achieve full dissociation. Once dissociated, the neural crest cell suspensions are pelleted at 300xg for 2min and resuspended in fresh NC-C and plated in a new ultra-low-attachment plate.

Schwann cell induction from hPSC-derived neural crest

On day 30 of the cranial neural crest cultures, crestopsheres are dissociated with Accutase as described above for 30min at 37°C with 5% CO_2. After centrifugation at 300xg for 2min, the cell pellet is resuspended in serum-free Schwann Cell Medium (SCM, ScienCell) and plated on poly-L-ornithine (PO, Sigma)/Fibronectin (Sigma)/Laminin (R&D Systems) coated plates. During Schwann induction, fresh SCM (serum-free) is fed daily. Starting on day 32 until day 38, SCM is supplemented with 100um cyclic AMP (cAMP, Sigma) to promote Schwann cell differentiation and 10uM SB431542 to prevent off-target differentiation. At day 39, cAMP is no longer added to the medium. Cultures were maintained in serum-free SCM and passaged at 90% confluence using 0.05% Trypsin for 1min at 37°C, with 5% CO_2.

Melanocyte primed neural crest induction and T1 melanocyte differentiation from hPSCs

From Studer and colleagues

hESC cultures at ~70% confluence were dissociated using EDTA and replated one to one on Geltrex coated plates in stem cell media (Essential 8) to establish an hESC monolayer. The following day, cranial melanocyte-primed neural crest induction was initiated (D0) by replacement of the stem cell maintenance media with neural crest induction media A (Essential 6 base medium, 600nM CHIR99021, 10uM SB431542, and 1ng/ml BMP4). On days 2 and 4 cultures are fed with neural crest induction media B (Essential 6 base medium, 1.5uM CHIR99021, 10uM SB431542). On days 6, 8, and 10, cultures are fed with melanocyte priming media (MPM) (media B with 10ng/ml BMP4 and 100ng/ml EDN3

(Sigma)) to bias the cranial NCCs towards a melanocyte fate. On day 12, primed neural crest induction cultures are dissociated with Accutase for 20min at 37°C with 5% CO_2, pelleted at 300xg for 2min, resuspended in neural crest maintenance media (NC-C) (Neurobasal base medium, 20ul/ml B27 supplement 10ul/ml N2 supplement, 10ul/ml Glutagro, 10ul/ml MEM NEAAs, 3uM CHIR99021 and 10ng/ml FGF2) and plated in ultra-low-attachment plates. On day 14 the primed crestospheres are fed with fresh NC-C media by gently swirling the plate on a flat surface to collect the spheres in the center of the well, aspirating the spent media carefully from the edges of the well without removing the crestospheres and replacing with fresh NC-C. On day 15 the primed crestopsheres are collected and centrifuged at 300xg for 1min and resuspended in Accutase for 15min at 37°C with 5% CO_2 to dissociate. Once dissociated, the primed neural crest cell suspensions are pelleted at 300xg for 2min and resuspended in melanocyte induction media (MIM) (50% Neurobasal, 30% Low glucose DMEM/F12 (Gibco), 20% MCDB201 base medium (Sigma), 2% B27 supplement, 1% Glutagro, 0.8% ITS+ (Gibco), 25ng/ml BMP4, 100ng/ml EDN3, 50ng/ml SCF (Peprotech), 4ng/ml FGF2, 50ng/ml Cholera Toxin Beta Protein (Novus), 3uM CHIR99021, 100uM Ascorbic Acid (Sigma), 500uM cAMP, 50nM Dexamethasone (Sigma)) and plated on poly-L-ornithine (PO)/Fibronectin/Laminin coated plates. Cultures are fed with fresh MIM every other day. Cultures are maintained at confluence or passaged for expansion by dissociation with Accutase for 5-10min at 37°C with 5% CO_2.

T2 Melanocyte induction from hPSC-derived schwann cell precursors (SCPs)

Following differentiation to Schwann cell precursors to Day 40, cultures were switched to MIM (used above). Cultures are fed with fresh MIM every other day. Cultures are maintained at confluence or passaged for expansion by dissociation with Accutase for 5-10min at 37°C with 5% CO_2.

2D Immunofluorescence

The adherent culture's media was aspirated, and cells were washed with PBS (Gibco). After washing, cells were fixed with 4% PFA (Santa Cruz) for 30 min at room temperature. After fixation cells were washed 3x with PBS prior to permeabilization using the BD Perm/Wash buffer 1X permeabilization buffer (PB, eBiosciences) for at least 30min at room temperature. Primary antibodies were diluted (Table 2.1) in PB and incubated on cells overnight at 4°C. Cells were washed with PB 3x for 5min each and incubated with secondary antibodies (Invitrogen) diluted 1:1000 in PB for 1hr at room temperature. Cells were again washed with PB 3x for 5min and finally placed in PBS for imaging on an epi-fluorescent microscope (Echo Revolve).

Whole mount Immunofluorescence

Crestospheres were transferred to Eppendorf tubes, centrifuged at 200xg for 1min (same parameters used for all subsequent centrifugation steps) and washed with PBS (all incubations and washes done on orbital rocker). Crestospheres were fixed with 4% PFA for 30minutes at room temperature and then washed with PBS 3x for 5min. Crestospheres were then permeabilized with 0.5% Triton X-100 (Thermo) in PBS for

20min at room temperature and then blocked with blocking buffer (0.1% Triton X-100, 5% donkey serum (Jackson Labs), and 1% BSA (Sigma) in PBS). Primary antibodies were diluted (Table 2.1) in blocking buffer and incubated with crestospheres for 48hrs at 4°C. Crestospheres were washed with blocking buffer 3x for 20min and then incubated with secondary antibodies diluted 1:1000 in blocking buffer for 48hrs at 4°C. Crestospheres were again washed with blocking buffer 3x for 20min and finally placed in PBS in coverslip chamber slides for confocal imaging using the molecular devices imageXpress microscope.

Flow Cytometry

Single cell suspensions were made using the passaging methods listed above depending on the time point being collected. Cells were pelleted by centrifugation at 500xg for 3min (same parameters used for all subsequent centrifugation steps) and washed with PBS. Cells were then fixed using the FOXP3/Transcription Factor staining buffer set 1X fixation/permeabilization buffer (eBiosciences) for 30min at 4°C. Cells were washed with PBS and then resuspended in 1X PB for 30min at room temperature. Primary antibodies were diluted (Table 2.1) in PB and incubated on cells overnight at 4°C. Cells were washed with PB 3x for 5min and incubated with secondary antibodies diluted 1:1000 in PB for 1hr at room temperature. Cells were again washed with PB 3x for 5min and finally resuspended in PBS and transferred to FACS tubes for cytometry analysis using an Attune NxT (Thermo). Population percentage-based analysis was performed using Flowjo (v10). See “melanin quantification” below for side-scatter analysis methods.

Quantitative reverse transcription PCR (RT-qPCR)

RNA was extracted using the PureLink RNA Isolation kit (Thermo). Briefly, cells were dissociated as described above, pelleted and resuspended in lysis buffer. Cell lysis suspensions were vortexed, snap frozen and thawed prior to column purification and elution in water. RNA stock concentrations were quantified by nanodrop. cDNA was generated using qSCRIPT cDNA SuperMix (Quantabio) using 1ug of RNA as input. cDNA was diluted to approximately 10ng/ul and used as input for 10ul qPCR reactions containing 10ng cDNA, 2.5uM primers (Table 2.5) and 50% PowerUp™ SYBR™ Green Master Mix (Thermo). qPCR reaction amplifications were measured using a QuantStudio 6 Real Time PCR system (Thermo).

Transmission electron microscopy sample preparation and imaging

Melanocytes were dissociated as described above and counted using a hemocytometer. Melanocytes were plated 10,000 cells/cm^2 in a PO/Fibronectin/Laminin coated permanox plastic Nunc™ Lab-Tek™ chamber slides (Thermo) in MIM. Melanocytes were cultured in slide chambers for 24hrs before fixation with a modified Karnovsky's fixative (2% formaldehyde, 2.5% glutaraldehyde, and 0.1M sodium phosphate, EMS) for 24hrs at 4C. Cells were washed with 0.1 M sodium phosphate buffer and then incubated in secondary fix (1% osmium tetroxide and 1.5% potassium ferrocyanide in 0.1M sodium phosphate) for 1 hour. Cells were washed with cold ddH2O 3 times before stepwise dehydration through an ethanol gradient at 30%, 50%, 70%, 95%, and 3x100% ethanol for at least 10 minutes each. Ethanol was removed and 100% resin was added and allowed to infiltrate overnight at room temperature. Next, as much resin as possible was removed from the

cells and fresh resin was added (Dodecenyl Succinic Anhydride, Araldite 6005, Epon 812, Dibutyl Phthalate, Benzyldimethylamine). The resin was polymerized overnight at 70C. Resin blocks were sectioned on Leica EM UC6 ultramicrotome at approximately 100nm, collecting sections on copper grids. Grids were dried in an oven at 60C for 20 minutes. Grids were stained with 4% aqueous uranyl acetate and 0.1% lead citrate in 0.1N NaOH. Sections were imaged in a FEI Talos L120C TEM at 80kv.

Melanocyte-Keratinocyte co-culture and melanosome transfer assay

Primary adult human keratinocytes (ATCC) were cultured on PO/Fibronectin/Laminin coated in Keratinocyte SFM (Gibco). At the start of co-culture, keratinocytes were dissociated with 0.05% Trypsin and counted with Trypan blue using a CellDrop FL (Denovix), while melanocytes were dissociated with accutase as described above and counted using a hemocytometer. Melanocytes and keratinocytes were mixed at a ratio of 1:10 to mimic the estimated ratio observed in human skin[294], i.e. keratinocytes were seeded at 150,000 cell/cm^2 and melanocytes at 15,000 cell/cm^2 in the same well, and plated on PO/Fibronectin/Laminin coated plates. Time 0 was considered to be two hours after initial plating to allow for cell attachment. Co-cultures are collected using 0.05% Trypsin to obtain single cell suspensions processed for Flow cytometry as described above at 24hr, 48hr and 72hrs. Additionally Co-cultures were fixed at 72hrs for 2D immunocytochemistry as described above. Flow and immunocytochemistry samples were stained with K14 (Thermo, Table 2.1) to mark keratinocytes and PMEL (Thermo, Table 2.1) as a melanosome incorporated protein. Flowjo was used to analyze

melanosome transfer as the percentage of PMEL+/K14+ keratinocytes versus total keratinocytes.

Bulk quantification of melanin

Melanocytes were dissociated with Accutase as described above and counted using a hemocytometer. Melanocytes were plated at 150,000 cell/cm^2 in a PO/Fibronectin/Laminin coated plate in MIM. Melanocytes were cultured for 72hrs and then lysed with 1X RIPA buffer (Sigma) using the supplier protocol for lysing of adherent cultures. Briefly, ice cold RIPA buffer was added to the wells of the plate and the plate was incubated on ice for 5min. The RIPA solution was pipetted up and down repeatedly in the well to lyse residual cells and then transferred to a microcentrifuge tube. Cell lysates were centrifuged at 14,000xg for 15 minutes at 4°C. This centrifugation step pelleted all melanin while the DNA remained in the supernatant. The supernatant was then transferred to a new microcentrifuge tube and the pellet containing the melanin is further dissolved by incubation in 250ul of 1M NaOH (Sigma) for 40min at 37C. Once fully dissolved, the lysate was transferred to a 96 well plate and the OD475 was measured using a plate reader (Molecular Devices). In parallel, the RIPA lysate was diluted 1:50 in PBS and mixed with propidium iodide (PI, Thermo) in PBS at a final ratio of 1:3000. PI fluorescence intensity, representing DNA abundance/concentration, was measured by excitation at 535nm and emission detection at 615nm, the maximal excitation/emission of PI when bound to DNA, using a plate reader. All lysates were measured in duplicates and averaged per biological replicate. The OD475 of each pellet dissolved in NaOH was normalized to the PI fluorescence intensity of the matching lysate. Normalized OD475

values of T1 and T2 melanocyte populations were statistically compared using an unpaired, two-tailed t-test.

Single cell quantification of melanin

Melanocytes were prepared for Flow cytometric analysis as described above. Side scatter voltage was set using a 1:1 mixture of T1 and T2 melanocytes. The resulting FCS files were analyzed in R, using the flowCore package (v2.8) for data importation. Each file, representing a biological replicate (BR) of the respective differentiation, was “gated” to remove debris events by filtering for events with a FSC-A value greater than 190000 and a SSC-A value greater than 50000. Each BR’s SSC-A values were then merged into a single event-by-BR matrix using the cbind function. The distribution of each BR's SSC-A values was then calculated by creating 512 equally sized SSC-A value bins, based on the minimum and maximum recorded SSC-A values across all BR’s and samples, and recording the number of events greater than or equal to the bin value and less than the next highest bin value for each bin. To account for differences in the number of recorded events per BR, each BR’s SSC-A bin count values were normalized to the maximum count value recorded for that BR. Distributions were visualized as the average normalized count per SSC-A bin with standard deviation ribbons calculated per SSC-A bin and plotted as +/- the average per bin. Distributions were compared statistically using Satterthwaite's method nested t-test.

Migration assay

Low throughput. Melanocytes or melanoma cells were dissociated as described above and were plated at 150,000 cell/cm^2 in a PO/Fibronectin/Laminin coated plate in MIM or tc-treated plate in DMEM 10%FBS, respectively. After 2 hours to allow cells to attach, wells were scratched with a 10ul pipette tip, using a new tip for each well. After scratching, a media change was performed to remove any free floating and/or dead cells and, optionally, to start drug treatments. This media change was considered time 0hr of the assay and representative brightfield images were taken on an echo revolve microscope to establish the average initial scratch width. Scratched plates were cultured for 72hrs and then cells were washed with PBS. After washing, cells were fixed with 4% PFA for 30min at room temperature. After fixation cells were washed with PBS and then incubated in 5ug/ml WGA, Alexa Fluor® 647 (Thermo) conjugate for 10min at room temperature. After incubation with WGA, cells were washed 3x with PBS and then left in PBS to image on an epi-fluorescent echo revolve microscope. Images were processed and analyzed using FIJI. Briefly, brightness and contrast was adjusted to maximize the cell membrane staining signal to background ratio. Next, images were thresholded to include cell membrane staining and exclude background. Then a region of interest (ROI) was drawn around the estimated original scratch area using the polygon tool, ensuring that the width of the ROI was equal to the width of the representative scratch images taken at 0hr and centered along the remaining 72hr scratch area. Migration efficiency into the scratched areas was quantified as the percentage of area covered by cells in the ROI.

High throughput. Melanocytes or melanoma cells were dissociated as described above and were plated at 150,000 cell/cm^2 in Geltrex coated plates in MIM or DMEM 10% FBS, respectively. After 2 hours to allow cells to attach, wells were scratched with an AccuWound 96 Scratch Tool (Agilent). If scratching multiple plates at once, the scratch tool was washed between plates according to the supplier's protocol. After scratching, a media change was performed to remove any free floating and/or dead cells and, optionally, add drug treatments. This media change was considered time 0hr of the assay and brightfield images were taken to establish the average initial scratch area in each well using a molecular devices ImageXpress high-content imaging system. Scratched plates were cultured for 72hrs and then cells were washed with PBS. After washing, cells were fixed with 4% PFA for 30min at room temperature. After fixation cells were washed with PBS and then incubated in 5ug/ml WGA, Alexa Fluor® 647 conjugate for 10min at room temperature. After incubation with WGA, cells were washed 3 times with PBS and then left in PBS to image on a molecular devices ImageXpress high-content imaging system. Images were analyzed using FIJI as described above.

T1 and T2 melanocyte migration was statistically compared using an unpaired, two-tailed t-test. Melanoma lines treated with ilomostat or transduced with a sgRNA were statistically compared using an ordinary one-way ANOVA with a Dunnett's multiple comparisons test against the vehicle or sgCTRL condition, respectively.

Doubling Time Assay

Melanocytes or melanoma cells were dissociated with Accutase as described above and counted using a hemocytometer. Melanocytes were plated at 150,000 cell/cm^2 in a PO/Fibronectin/Laminin coated plate in MIM. Melanoma cells were plated at 150,000 cell/cm^2 in in their respective medias (above). After allowing the cells to attach for two hours, three wells were lysed with 1X RIPA buffer on ice for 5 minutes. The RIPA solution was pipetted up and down repeatedly in the well to lyse residual cells and then transferred to a microcentrifuge tube. Cell lysates were centrifuged at 14,000xg for 15 minutes at 4C. The supernatant was then transferred to a new microcentrifuge tube and diluted 1:50 in PBS and mixed with propidium iodide (PI) in PBS at a final ratio of 1:3000 before transferring to a 96 well plate. PI fluorescence intensity was measured by excitation at 535nm and emission detection at 615nm using a plate reader. The mean of the three wells was calculated to quantify the average DNA concentration per well at time 0hr. The remaining wells were cultured for 72hrs before repeating the RIPA lysis and PI based DNA concentration quantification steps. The growth rate of each well was calculated as (72hr PI a.u. - average 0hr PI a.u.)/average 0hr PI a.u. where the 0hr average was specific to each independent assay and sample. T1 and T2 melanocyte doubling time was statistically compared using an unpaired, two-tailed t-test. Melanoma lines transduced with a sgRNA were statistically compared using a two-way ANOVA with a Šídák's multiple comparisons test against the sgCTRL condition.

Mice

C57BL6/J males and females were mated, where the presence of a vaginal plug was identified as E0.5. Pregnant female mice were euthanized at E12.5 and embryos were dissected. All mouse work was performed under the University of California, San Francisco, Institutional Animal Care and Use Committee guidelines in an approved facility of the Association for Assessment and Accreditation of Laboratory Animal Care International.

Preparation of embryos

E12.5 embryos were dissected in 0.4 % BSA in PBS. Embryos were fixed rocking in 4% PFA overnight at 4°C. After fixation, embryos were washed three times with PBS for 20min each then cryoprotected by immersion in a 10% - 30% stepwise sucrose gradient overnight at 4°C. Embryos were incubated in 1:1 30% sucrose:OCT (Fisher) for 1hr, then embedded transversely in OCT for storage at -80 °C. Embryos were sectioned (20 mm thickness) using a cryostat (Leica).

Mouse tissue immunofluorescence staining and imaging

Transverse embryo sections from cranial, front limb, abdomen, and hind limb regions were washed in PBS followed by permeabilization with 0.4% Triton-X in PBS for 10min. Tissue sections were blocked with 5% donkey serum and % BSA in 0.1 % Triton-X in PBS for 2hr at room temperature. Tissue sections were incubated with MITF, TUBB3, CD44-AF647 primary antibodies diluted (Table 2.1) in blocking buffer overnight at RT. Antibodies were detected by incubating with secondary antibodies diluted 1:200 in

blocking buffer overnight at RT. Samples were tile-imaged by using a white-light Leica TCS SP8 converted confocal microscope with a 25 X water objective, 0.75 X optic zoom, and 1024 x 1024 pixel resolution, and stacks were acquired at system-optimized z steps between optical sections (z step size, 1 um).

Mouse Tissue quantifications

Tissue section tile scans were analyzed using FIJI. Max intensity projections were created and each channel's brightness was manually adjusted. The multi-point tool was used to mark CD44+/- MITF+ nuclei ROIs. MITF and CD44 positivity was determined manually by signal relative to local background. Dorsoventral location of each MITF nuclei was calculated via measurement of the X and Y coordinates of the multipoint ROIs and then scaled to the X and Y coordinates of the most dorsal and most ventral point of each tissue section. Dorsoventral distributions of CD44+ and CD44- melanocyte populations were statistically compared using an unpaired, two-tailed t-test.

Generation of MeWo and A375 CRISPRi lines

A dCas9-KRAB-mCherry lentiviral construct (pHR-UCOE-EF1A-dCas9-HA-2xNLS-XTEN80-KRAB-P2A-mCherry)[281] was used to generate CRISPRi-competent MeWo and A375 cells. HEK293T cells were maintained in DMEM supplemented with 10% FBS, penicillin, streptomycin and amphotericin B, and passaged using 0.05% Trypsin prior to cells reaching 90% confluency. To generate dCas9-KRAB-mCherry lentivirus for transduction of the melanoma cell lines, HEK293T cell were first plated at 175,000 cells/cm2. The dCas9-KRAB-mCherry plasmid was mixed with the pCMV_ΔR8.91 and

pMD2.G packaging vectors at a ratio of 9:8:1 with TransIT®-Lenti Transfection Reagent (Mirus) in optiMEM (Gibco) and used for the HEK293T cell transfection. After 3 days, lentivirus-containing media was harvested and filtered using a .45um filter. The viral supernatant and polybrene (8 ug/ml final concentration, Sigma) was then added to the melanoma cell lines, both of which already contained luciferase reporter constructs for *in vivo* imaging, plated at 500,000 cells per 10cm plate. Transduced cell lines were then expanded and purified using fluorescence activated cell sorting for the mCherry reporter. CRIPSRi activity in each cell line was validated by lentiviral transduction with pCRISPRia-v2 (Addgene #84832) backbones containing either a guide RNA (gRNA) targeting ST3GAL4 or a non-targeting gRNA (Table 2.5) using the above protocol. Following transduction with the guide expression constructs, transduced cells were purified using puromycin (Gibco) selection. Once purified, RNA was extracted using the PureLink RNA kit and knockdown was assessed by qPCR as described above using primers to detect ST3GAL4 expression (Table 2.5). The line was determined efficient if ST3GAL4 expression was reduced by 80%.

gRNA library generation

The gRNA library was designed to contain five gRNAs targeting each transcriptional start site of the top 100 most significantly enriched genes in the T1 and T2 melanocytes when directly compared as well as 50 non-targeting control gRNAs for a total of 1125 gRNAs. gRNA sequences were obtained from the previously described human genome-wide CRISPRi (v2.1) gRNA library[295] and inserted between flanking nucleotide sequences to be used for PCR amplification and ordered as an oPool from IDT (Table 2.5). The PCR-

amplified gRNA pool was then cloned into the pCRISPRia-v2 backbone via the BstXI-Bpu1102I (Thermo) sites and electroporated into competent *E. coli* cells (Thermo). Colony-forming unit (CFU) quantification of the electroporated library was used to assess library coverage (>5000x CFU per library element coverage achieved). The gRNA sequences were PCR-amplified from the library plasmid pool and sequenced on the Illumina MiSeq sequencer to confirm the uniform gRNA representation and distribution.

CRISPRi i*n vivo* screen

gRNA library lentivirus was generated as described above, aliquoted and frozen. Viral titer was approximated by infection of MeWo cells with titrated virus dilutions followed by flow cytometry, determining the percentage of BFP-expressing cells. For the screen, 3 million MeWo cells per replicate were transduced with gRNA library virus at 30% MOI to ensure >500x library coverage in the transduced population. Transduced cultures were puromycin selected and immediately used for the following steps to avoid fitness bias. First, two replicates were collected immediately for genomic DNA extraction to serve as reference for the starting gRNA pool at time 0. Two additional replicates were tail vein injected into NSG (NOD scid gamma, Jackson Labs) mice. Lung colonization was monitored by *in vivo* luciferase activity imaging for 6.5 weeks, the animals were euthanized, lung tissue was collected, roughly mechanically dissociated and fully dissociated by incubation in 1mg/ml liberase (Sigma) in 1:1 DMEM:F12K supplemented with DNase I (Worthington Biochemical), 6.5mg/ml collagenase (Worthington Biochemical), penicillin, streptomycin and amphotericin B at 37°C with shaking. If necessary, red blood cell lysis was performed with ACK buffer (Thermo) before mouse

cells were removed from the dissociated lungs using the mouse cell depletion kit (Miltenyi Biotec) yielding purified MeWo cells that achieved successful lung colonization. In parallel, two replicate cell populations were continued in culture *in vitro* for 17 days to mimic the estimated number of doublings achieved by the injected MeWo cells before genomic DNA extraction. Genomic DNA extraction for all samples was performed with QuickDNA (Zymo) kits. Each genomic DNA sample was digested with BstXI, and tagged by UMI-introducing primer extension (Table 2.5) using Klenow polymerase, exo- (NEB). The tagged gRNA sequences were PCR-amplified and sequenced on Illumina HiSeq 4000 sequencer SE50 run at UCSF Center for Advanced Technology. gRNA sequencing data was analyzed using iAnalyzeR (https://github.com/goodarzilab/iAnalyzer). Briefly, count matrices per gRNA were generated for each sample by alignment to the input gRNA protospacer sequences. gRNA abundances per sample were compared using a univariate analysis. Hits were selected as guides significantly decreased in metastatic samples compared to the input samples but not significantly decreased in *in vitro* samples compared to the input samples.

Generation of MeWo and A375 knockdown cell lines

For each gene (HMG20B, MMP17 and SNRPB), two DNA oligos consisting of the top two predicted targeting protospacer sequences from previously described human genome-wide CRISPRi (v2.1) gRNA library[295] were synthesized (IDT) and Gibson-cloned into pCRISPRia-v2 vector (Table 2.5). Both the MeWo and A375 CRIPSRi/Luciferase cells were transduced with gRNA-expressing lentivirus, produced in HEK293T cells as described above. Each gRNA knockdown cell line was puromycin selected and the

knockdown efficiency was validated by qPCR. For each gene, a delta CT (dCT) value was calculated by subtraction of the samples GAPDH CT value. Delta delta CT (ddCT) values were calculated by subtraction of the biological replicate matched non-targeting guide condition dCT from the KD sample dCT value for the targeted gene. Values were reported as fold changes normalized to non-targeting controls calculated as 2^{-ddCT}. Fold change values were statistically compared using an ordinary one-way ANOVA with a Dunnett's multiple comparisons test against the sgCTRL condition.

Bulk RNA sequencing and spliceoform analysis

RNA from n=2 control and n=2 SNRPB-KD MeWo and A375 samples was collected and isolated as described above. RNA-seq libraries were prepared using SMARTer Stranded Total RNA-Seq Kit v3 - Pico Input Mammalian (Takara) according to manufacturer's recommendations, using 10 ng total RNA as input. The libraries were sequenced on a 2x 35 bp PE run on a NextSeq 550 instrument (Illumina). UMI-tools (v1.0.0) was used to extract UMI's from read 2. Cutadapt (v2.3) was used to trim R1 to an identical length. This is required since MISO expects reads of equal length for both pairs. STAR (v2.7.1a) was then used to align reads to the human genome (hg38) and UMI collapse (1.0.0) was used to remove PCR duplicates (with --two-pass --paired --remove-unpaired --remove-chimeric flags). The resulting deduplicated bam files were sorted by name and converted back to fastq files (samtools v1.7). The deduplicated fastq files were aligned to a curated human transcriptome using bowtie (2.3.5) and bamPEFragmentSize (3.5.1) was used to calculate fragment length distribution parameters (i.e. mean and standard deviation). MISO (0.5.4) was then used to analyze changes in skipped exon inclusions by passing

the deduplicated STAR-aligned bam files along with the fragment size distribution for each sample.

SNRPB CLIP

HEK-293 cells with SNRPB endogenously tagged with split mNeonGreen (Cho et al. Science 2022) were crosslinked with 400mJ/cm2 254nm UV. Crosslinked cells were lysed with ice-cold lysis buffer (1X PBS, 0.1% SDS, 0.5% sodium deoxycholate, 0.5% IGEPAL CA-630) supplemented with 1x halt protease inhibitors (Pierce) and SuperaseIN (Invitrogen). After lysis, samples were treated with DNase I (Promega) at 37degC, shaking at 1000rpm for 5 minutes. Each lysate sample was then split equally, and each portion treated with either a medium or low dilution of a mix of RNase A and RNase I (Thermo; 0.11ng/ul RNase A and 0.03units/ul RNase I, and 0.02 RNase A and 0.03units/ul RNase I, respectively) at 37degC for 5 minutes. Lysate was cleared by centrifuging at 21,000xg 4degC 20 minutes. The clarified lysate was added to pre-washed mNeonGreen-trap magnetic agarose beads (ChromoTek). Immunoprecipitation was performed at 4degC with end-over-end rotation for 2 hours. Beads were then washed 2X with high salt wash buffer (5X PBS, 0.1% SDS, 0.5% sodium deoxycholate, 0.5% IGEPAL CA-630), 2X with lysis buffer (1X PBS, 0.1% SDS, 0.5% sodium deoxycholate, 0.5% IGEPAL CA-630), and 2X with PNK buffer (10mM Tris-HCl pH 7.5, 0.5% IGEPAL CA-630, 10mM MgCl2). The RNA was then end-repaired and poly(A) tailed on-bead by treatment first with T4 PNK (NEB) and then treatment with yeast poly(A) polymerase (Jena Bioscience). The RNA was further 3'-end-labeled with azide-dUTP (TriLink biotechnologies) using yeast poly(A) polymerase (Jena Bioscience). The protein-RNA

complexes were then labelled with IRDye800-DBCO (LiCor). The protein-RNA complexes were then eluted from beads, resolved by running on a 4-12% Bis-Tris NuPAGE gel (Invitrogen), transferred to protran BA85 nitrocellulose (Cytiva), and imaged using an Odyssey Fc instrument (LiCor). The regions of interest were excised from the membrane and the RNA was isolated by Proteinase K (Invitrogen) digestion and subsequent pulldown with oligodT dynabeads (Invitrogen). After eluting from the oligodT beads, the RNA was immediately used for library preparation using the SMARTer smRNA-Seq Kit (Takara), with the following modifications. The poly(A) tailing step was omitted, and reverse transcription was performed with a custom RT primer. The PCR step was performed with indexed forward (i5) primers and a universal reverse (i7) primer. The libraries were PAGE purified and then sequenced on an Illumina HiSeq4000 instrument at the UCSF Center for Advanced Technologies.

Single cell RNA sequencing (scRNAseq) library preparation, sequencing and processing

Adherent or 3D cultures were dissociated using the methods described above specific to each timepoint collected. Single cell suspensions were counted and diluted for GEM generation & barcoding, post GEM-RT cleanup & cDNA amplification, 3’ gene expression library construction, and sequencing on Illumina NovaSeq sequencer according to the 10x Genomics Chromium Next GEM Single Cell 3’ Reagent Kits v2 User Guide. CellRanger v2.1.1 was used to map reads to the human reference hg38 transcriptome and generate gene count matrices.

scRNAseq data analysis

Cell quality assessment and filtration. Each dataset, corresponding to a unique timepoint or differentiation protocol was analyzed independently using Seurat (v4.3). First, several per-cell quality control metrics were calculated such as the percentage of mitochondrial gene reads (percent.mito), the percentage of ribosomal gene reads (percent.ribo) and a gene per umi novelty score calculated as log10(nFeatures) divided by the log10(nCount)(novelty.score). Low quality cells were identified using nCount and nFeature ranges specific to each dataset (Table 2.2) and excluded from further analysis.

Clustering, dimensionality reduction and annotation. Datasets were log normalized using a scale factor of 10,000 using NormalizeData. Variable features were identified using the "vst" method with default parameters of the FindVariableFeatures function. Cell cycle status was predicted using the CellCycleScoring function based on Seurat provided S phase and G2M Phase gene sets. Feature counts were scaled and the calculated S.Score, G2M.Score, percent.ribo and novelty score variables were regressed out using ScaleData. Principal component analysis (PCA) was performed using RunPCA with default parameters. Uniform manifold approximation and projection (UMAP) dimensionality reduction was performed using RunUMAP with PCA as the reduction input. Shared nearest-neighbor (sNN) graphs were constructed using FindNeighbors. Finally, cell clusters were unbiasedly identified using louvain clustering via the FindClusters function. The number of principal components used in RunUMAP and FindNeighbors as well as the resolution used in FindClusters was specific to each dataset (Table 2.3). Differentially expressed genes of each cluster were identified using the

Wilcoxon Rank Sum test with the FindAllMarkers function. Clusters were annotated using known cell-type markers. Gene-dropout correction via count imputation was performed using adaptively-thresholded low rank approximation (ALRA) using the RunALRA function in the SeuratWrappers package (v.3). Imputed gene counts were used for all subsequent analysis unless otherwise specified[296,297].

Transcription factor activity analysis. SCENIC (v1.3) was run independently on each dataset. Imputed count matrices and metadata were extracted from the above analyzed Seurat objects. Human RcisTarget databases were downloaded from resources.aertslab.org. Imputed count matrices filtered to remove genes with total counts less than 3% of the number of cells in the dataset or cells with detected genes fewer than 1% of the number of cells in the dataset. Coexpression networks were identified using runCorrelation and GENIE3 (v1.18) was used to identify transcription factor modules using runGenie3 from the filtered imputed matrix. Gene regulatory networks were then identified and scored using the SCENIC wrapper functions with default parameters. Briefly, runSCENIC_1_coexNetwork2modules was used to create the co expression modules, runSCENIC_2_createRegulons was used to identify regulons using transcription factor motif analysis and finally, regulon activity was calculated using runSCENIC_3_scoreCells.

Pseudotime analysis. Monocle3 (v1) was run independently on each dataset. Imputed count matrices and metadata were extracted from the above analyzed Seurat objects and used to create CellDataSets compatible with monocle3 using new_cell_data_set. The

CellDataSet was preprocessed but not normalized, as the imputed counts matrix was already normalized, using preprocess_cds with norm_method = "none". The number of dimensions used for each dataset during pre-processing was specific to each dataset and can be found in (Table 2.2). Cell cycle effects were removed using the align_cds function based on the cell cycle phases determined by Seurat CellCycleScoring. UMAP dimensionality reduction was performed using reduce_dimension. Clustering was not performed as cell cluster labels were transferred from the Seurat object. Finally, the pseudotime trajectories were predicted using the learn_graph function. A root state was chosen using order_cells based on the most central root point in the unbiased NCC cluster.

Ligand-receptor interaction analysis. CellChat (v1.4) was run independently on each dataset.Imputed count matrices and metadata were extracted from the above analyzed Seurat objects and used to create CellChat objects using createCellChat. All cell-cell communication types were used from the human CellChat database. The subsetData function was used to filter the imputed counts matrix for signaling related genes. Using the filtered maxtrix, overexpressed ligand and receptors are then identified per each specified cell grouping using the identifyOverExpressedGenes functions followed by over expressed ligand receptor interactions using identifyOverExpressedInteractions. The probability of communication between the specified cell groups is then predicted using the computeCommunProb function. The communication probability of whole signaling pathways were then computed based on the individual receptor-ligand probabilities using computeCommunProbPathway.

Module scoring. To identify transcriptionally similar cell populations between datasets, cluster gene signatures were created. First, the differentially expressed genes with a positive log2 fold change for each cluster in the reference dataset were filtered to exclude genes not detected in the query dataset. Of the remaining genes, the top 100 most significantly differentially expressed were used as the cluster's transcriptional signature (Table 2.4). The query dataset's cells were then scored for the expression of the cluster's transcriptional signature using Seurat's AddModuleScore function based on the imputed gene counts.

Similarly weighted non-negative embedding (SWNE) analysis. For the datasets to be compared, the counts matrices were filtered to only include genes detected in both the query and reference dataset. First, the similarly weighted nonnegative embeddings (SWNE) are calculated for the reference dataset using the SWNE (v0.6) package. Briefly, 3000 variable genes are identified from the reference dataset's non-imputed gene counts using FindVariableFeatures and component factors are identified by nonnegative matrix factorization (NMF) using RunNMF from NMF v0.23. The number of factors to be identified (k) was set equal to the number of PCs used during initial analysis with Seurat) (Table 2.2). sNN graphs calculated previously were extracted from the reference seurat object and pruned using PruneSNN based on the reference dataset's previously calculated kNN matrix, specified cell grouping and a Q-value cutoff of 0.001. Finally, Sammon mapping is used for dimensionality reduction of the component factors by calculating factor embeddings using the reference dataset's sNN matrix. This allows for

both cells and genes to be plotted based on their influence by and contribution to the component factors, respectively. To project the query dataset onto the reference SWNE, sNN between the query and reference dataset are first calculated. To do this, the reference dataset's PC loadings are used to calculate PC embeddings of the previously determined 3000 variable gene based on the query dataset's scaled gene counts. The sNN matrix is then calculated from the query dataset's PC embeddings trained on the reference PC embeddings using ProjectSNN. Next, NMF gene loadings for the query dataset are calculated from the reference dataset's factor decomposition results using ProjectSamples. Finally, the query dataset is projected onto the reference SWNE embeddings using ProjectSWNE.

*Transcription factor modules identification**.*** For Stage 2-4 NCC subset datasets, average regulon activity scores per NC subtype were calculated and the subsequent regulon by NC subtype matrices were merged, excluding S4 NCC3 which is not predicted to follow a melanogenic lineage. Regulon modules were identified using specific filtering criteria to identify regulons exhibiting desired trends in activity along the predicted lineage paths. Module 1 consists of regulons detected to be active in all subtypes, where the activity in S2 NCC2 is greater than S2 NCC1, S3 NCC2 is greater than S3 NCC3 by at least 0.05, and S3 NCC2 is greater than S3 NCC1 and all S2 and S4 NCC subtypes. Modules 2 consists of regulons detected to be active only in S2 and S3 subtypes, where the activity in S2 NCC2 is greater than S2 NCC1, S3 NCC2 is greater than S3 NCC3 by at least 0.05, and S3 NCC2 is greater than all S2 subtypes and S3 NCC1. Module 3 consists of

regulons detected to only be active in S3 subtypes, where the activity of S3 NCC2 is greater than S3 NCC3 by at least 0.05, and S3 NCC2 is greater than S3 NCC1. Module 4 consists of regulons detected to only be active in S3 and S4 subtypes, where the activity of S3 NCC3 is greater than S3 NCC1, S3 NCC2 is greater than S3 NCC3 by at least 0.05, and S4 NCC1 is greater than S4 NCC3. Module 5 consists of regulons detected to be active in all subtypes, where the activity of S3 NCC3 is greater than S3 NCC2 and S4 NCC3 is greater than S2 NCC2 by at least 0.05. Module 6 consists of regulons detected to only be active in S3 and S4 subtypes, where the activity of S3 NCC3 is greater than both remaining S3 subtypes, and S4 NCCs is greater than S2 NCC2 by at least 0.05. Module 7 consists of regulons detected to be active only in S4 subtypes, where S4 NCC3 is greater than S4 NCC1 by at least 0.05. Finally, module 8 consists of regulons detected only S2 and S4 subtypes, where S4 NCC3 is greater than S4 NCC1 by at least 0.05 and S2 NCC2 is less than S2 NCC1 by at least 0.05.

Ligand-receptor module identification. For stage 2-4 NCC subset datasets, receptor-ligand signaling scores for each NC subtype were calculated and the subsequent regulon by NC subtype matrices were merged, excluding S4 NCC3 which is not predicted to follow a melanogenic lineage. Raw signaling scores were scaled by a factor of 10^6 and log transformed for comparison and visualization. Ligand-receptor pair (LRP) modules were identified using specific filtering criteria to identify LRPs exhibiting desired trends in activity along the predicted lineage paths. Module 1 consists of LRPs active in S2 NCC1 and S3 NCC2, and the activity of S3 NCC2 is greater than S3 NCC3 by at least .7. Module 2 consists of LRPs active in S3 NCC1 and S3 NCC2, where the activity of S3 NCC2 is

greater than S3 NCC3 by at least .7, and not active in S2 NCC1. Module 3 consists of LRPs active in S3 NCC2, where the activity of S3 NCC2 is greater than S3 NCC3 by at least .7, and not active in S2 NCC1 or S3 NCC1. Module 4 consists of LRPs active in S2 NCC1, S3 NCC3 and S4 NCC3, where both S3 NCC3 and S4 NCC3 are greater than S3 NCC2 by at least .7. Module 5 consists of LRPs active in S3 NCC1, S3 NCC3 and S4 NCC3, where both S3 NCC3 and S4 NCC3 are greater than S3 NCC2 by at least .7, but not active in S2 NCC1. Finally, Module 6 consists of LRPs active in S3 NCC3 and S4 NCC3, where both S3 NCC3 and S4 NCC3 are greater than S3 NCC2 by at least .7, but not active in S2 NCC1 or S3 NCC1.

Analysis of published datasets

Mouse Neural Crest Dataset. QC filtered and processed .h5ad files were obtained from GEO (GSE201257). The reticulate package (v1.28) was used to interface with the python scanpy package to import data into R and was then converted into a Seurat object, preserving the authors original metadata, leiden clustering and UMAP coordinates. Leiden clusters were annotated into cell types using the expression of cell type markers described in the original publication[51].

Human Melanocyte Datasets. Eight single cell RNA seq datasets containing melanocytes from healthy donors were curated from GEO (GSE151091, GSE162054/GSE153760, GSE147424, GSE150672 and GSE130973), the EGA (EGAS00001002927) and the human cell atlas: Developmental (https://developmental.cellatlas.io/) (Developmental cell programs are co-opted in inflammatory skin disease: Human Adult Healthy 10x Data and

Human fetal 10x data). When necessary, datasets were first subsetted to exclude disease samples. All datasets were processed using the Seurat analysis pipeline described above with one modification. In place of running PCA analysis, mutual nearest neighbors (mnn) correction was performed using the FastMNN function from the SeuratWrappers package to perform batch correction of each unique patient sample within the respective dataset. Subsequently, the UMAP and sNN were calculated using the mnn reduction based on 30 dimensions. For datasets where uploaded metadata did not include cell type annotations, the melanocyte cluster was identified by expression of MITF, PMEL, DCT, TYR and MLANA. For each dataset the melanocyte cluster was subsetted and the relevant metadata names and levels were made consistent across datasets. All melanocyte datasets were then merged and processed using the same Seurat pipeline as above, utilizing the FastMNN function to perform batch correction based on the original dataset identifier.

Analysis of datasets from the cancer genome atlas (TCGA)

BulkRNA sequencing datasets of 471 melanoma samples from 469 different patients were curated from the cancer genome atlas and merged into a sample by gene FPKM matrix. Ensembl IDs were converted to gene names using BiomaRt.

Gene set enrichment analysis (GSEA)

Differential gene expression was performed comparing T1 to T2 melanocytes using the Wilcoxon Rank Sum test. T1 and T2 melanocyte transcriptional signatures were constructed consisting of the top 100 most significantly enriched genes in each respective

melanocyte type. To identify melanoma samples that transcriptionally resemble either melanocyte type, gene set enrichment analysis was performed on each melanoma sample for the T1 and T2 melanocyte transcriptional signatures using the fgsea package (v1.22). Melanoma samples were labeled as either enriched or reduced for each transcriptional signature corresponding to a significant positive or significant negative enrichment score, respectively.

Survival analysis

Survival curves were generated using the patient metadata obtained from TCGA using the survival package (v3.5).

Melanoma samples were grouped by melanocyte signature enrichment status (determined by GSEA above) and compared using the Mantel-Cox test. When comparing T1 enriched to T2 enriched melanomas, samples that were significantly enriched for both signatures were discarded from the analysis.

The melanoma TCGA data was used to identify higher confidence hits from the CRISPRi screen. For all hits nominated by the univariate analysis, the full range of expression values was tested as thresholds for grouping samples with an expression value higher or lower than the test threshold and testing the survival difference between the high and low expression groups using the Mantel-Cox test. Genes were considered high confidence hits if an expression threshold for that gene existed where higher expressing samples had significantly lower survival probability than lower expressing samples.

Cox proportional hazard analysis

To further narrow high confidence gene targets, a cox proportional hazard was performed for all genes with significant survival thresholds using coxph. Using the expression threshold determined in the survival analysis a multivariate cox proportional hazard were performed. Univariate tests considered only the samples higher or lower expression than the predetermined threshold, while the multivariate test also considered multiple other criteria from the patient metadata (diagnosis age, metastasis stage, lymph node stage, neoplasm disease stage, tumor stage, neoadjuvant therapy type, adjuvant postoperative pharmaceutical therapy, adjuvant postoperative radiotherapy). Genes were considered high confidence hits if the expression threshold grouping maintained a significant hazard ratio when all variables were considered.

Chapter 3 Concluding Remarks

3.1 Overview of findings

Our study provides a comprehensive temporal map of human NCC lineage specification in a hPSC-derived model. Single cell profiling at early stages of our differentiation revealed cell populations and predicted signaling interactions that mirror that of the developing neural plate. Our transcriptomic profiling of differentiating hPSCs at single cell resolution revealed dynamic and increasing transcriptional heterogeneity within the NCC populations over time. Lineage analysis of NCC subtypes revealed a sustained population of uncommitted NCCs which maintained melanogenic competency and gained a gliogenic hub-like state over time.

Interestingly, the melanogenic progenitors produced by stage 2 and stage 4 NCCs are transcriptionally distinct, which we refer to T1 and T2 progenitors respectively. In the stage 3 NCCs, we captured a transition point where the uncommitted NCCs are competent to produce both melanogenic progenitors prior to becoming restricted to only specifying the T2 progenitors. The kind of melanogenic progenitor produced appears to be tightly linked to the age of the NCCs, as we showed that existing protocols which included exogenous melanogenic signals such as BMP4 and EDN3 prior to stage 2 do not produce another transcriptionally distinct melanogenic progenitor but are rather more efficient at producing the T1 melanogenic progenitors. Inter and intra-dataset lineage

tracing of the sub populations revealed two diverging lineage trajectories between S2-S4 NCCs.

Our comparison of T1 and T2 progenitors identified 114 transcription factors and 70 ligand-receptor pairs with differential activity patterns. Interestingly, many transcription factors were expressed by both melanogenic progenitors but were predicted to be differentially active. Remarkably, T1 and T2 progenitors showed differential expression of genes relevant to their *in vivo* features. For example, T1 progenitors expressed EPHB2 which is necessary for dorsolateral migration of NCCs and melanoblasts, while T2 progenitors expressed CD44, a neuronal cell adhesion molecule utilized by glia for nerve track migration[298,299].

From these progenitors, we show the highly efficient derivation of pigmented melanocytes, establishing a new protocol for SCP-derived melanocytes *in vitro*. Importantly, both types of melanocytes produce mature melanosomes and can transfer the melanosomes to keratinocytes. However, we found that T2 melanocytes appeared morphologically distinct and exhibit higher levels of pigment production. T2 melanocytes also displayed higher migratory ability but slower cell doubling time to T1 melanocytes. While T1 and T2 melanocytes expressed the same canonical markers, they were largely transcriptionally unique, with greater than 1500 differentially expressed genes.

We used these transcriptional signatures to identify T1-like and T2-like melanocytes in published human scRNAseq datasets and mouse fetal tissue, showing that both kinds of

melanocytes persisted into adulthood and their markers are conserved. In mice, consistent with their predicted ventrolateral migration path[54,119], T2-like melanocytes were more ventrally distributed within the fetal skin. Interestingly, T1-like melanocytes were more abundant in posterior regions both in fetal mouse tissue and in adult human skin samples.

Relating T1 and T2 melanocyte transcriptional signatures to melanoma, we found that a T2 signature in melanomas was associated with lower survival probability, possibly due to a higher metastatic potential. Our *in vivo* CRISPRi screen revealed that of the 100 most significantly enriched genes in T2 melanocytes, 25% played a role in metastatic lung colonization in mice. For 9 of these genes, including HMG20B, MMP17 and SNRPB, expression level alone was a significant predictor of melanoma patient survival outcome. Knockdown of these three transcripts in melanoma cells was sufficient to decrease both migration and lung colonization, with SNRPB knockdown resulting in the most substantial reduction of lung colonization. SNRPB is an RNA splicing factor, and alternative splicing events have previously been identified as markers of oncogenic progression in melanoma[300,301]. Splicesome analysis of SNRPB KD melanoma cells revealed alternative splicing events in genes implicated in cell proliferation, adhesion, and migration.

Altogether, our hPSC-derived model of temporal NC patterning enabled the discovery of temporally specific melanocyte subtype specification events and the underlying transcriptional frameworks of these distinct populations. This work establishes a new differentiation protocol which permitted the first comparison of melanocytes derived from

temporally distinct progenitors and found many functional and transcriptional differences. Finally, we implicate and validate SCP-derived melanocyte enriched genes as indicators of high metastasis rate in melanoma. Collectively, this work demonstrates the utility of directed stem cell differentiations as models which can facilitate novel developmental discoveries.

3.2 Perspectives and future directions

Profiling NCCs in high temporal resolution has been challenging to achieve, particularly in humans due to ethical and technical limitations associated with obtaining fetal tissue. Newly advanced hPSC differentiation systems recapitulate the process of embryonic and fetal development with high precision and provide access to transient populations such as NCCs. Using an *in vitro* induction system that mimics the normal developmental environment captures complex aspects of NCC fate specification that replicates *in vivo* conditions. Overall, our results highlight the power of this hPSC-based system in studying aspects of neural crest specification, differentiation, and identity.

Many aspects of neural crest population identity, potency and lineage identity remain unanswered. With stem cell-based models of axially and spatially patterned neural crest populations, we can begin to test reproducible populations of NCCs for their lineage competency by the simple addition of specific growth factor cocktails. Additionally, these populations can be profiled at high resolution using omics techniques to uncover unique

aspects of NC subpopulation identity, such as epigenetic signatures and chromatin landscapes[257].

These unique characteristics must be explored to better understand aspects of NC fate restriction and potency. Indeed, our data suggest that prolonged culture of NCCs sustained by WNT and FGF signaling results in cell intrinsic changes in NC populations. These changes allow for the adoption of a hub-like fate and glial competence in late NC populations. Orthologous time-dependent lineage specification programs exist in the central nervous system where radial glia first give rise to neurons and then glia and astrocytes[302]. It will be interesting to see if the underlying mechanisms of glia fate competency acquisition are similar between the central and peripheral nervous systems[302].

Emergence of our temporally distinct melanogenic NCC is consistent with previous *in vivo* studies that describe two waves of melanogenesis from early NCCs that migrate dorsolaterally through the mesenchyme and late NCCs that migrate ventrolaterally along the developing nerves[54,119]. This highlights the utility of hPSC models for the profiling and characterization of NC development. Parallel omics profiling of the same derivative cell types of these different NC population models, such as NC- and SCP-derived melanocytes or cranial- and trunk-derived melanocytes, will be essential for understanding how spatiotemporal identity effects mature cell type identity. The difference in activity, but not expression, of transcription factors between the unique melanogenic progenitors suggest that epigenetic changes play a substantial role in transcriptional

differences in these lineages. Epigenomic profiling of these progenitors and fully differentiated melanocytes will be essential for understanding how these distinct melanocyte populations arise and mature.

Despite finding many functional differences between NC- and SCP-derived melanocytes, the unique roles of these different populations remain unanswered. The physiological implication of this pigmentation difference and possible links between the distribution of T1 and T2 melanocytes in different skin regions and levels of pigment production should be explored further. Future studies will be required to validate developmental roles specific to T1 or T2 melanocytes which may provide new etiological insights into neurocristopathy syndromes involving pigmentation defects and peripheral neuropathies. For example, T1 melanocytes uniquely expressed NGF and semaphorins, suggesting a role in neurotrophic support and axon guidance.

Although SNRPB was previously identified as an oncogenic candidate in glioblastoma[291], its possible roles in melanoma were not identified. Our data suggest that SNRPB controls the splicing of transcripts involved in the migration and adhesion of melanoma cells. Future work will be necessary to mechanistically understand how the alternatively spliced isoforms regulate these cellular functions. Collectively, these results indicate that melanomas that display the unique signatures of melanocytes from temporally distinct developmental origins constitute different categories of melanoma and likely require personalized therapeutic approaches. Future studies will be necessary to show direct oncogenic transformation of each type of melanocyte and the conservation of these

original transcriptional signatures during the tumorigenesis process. Additionally, comparisons of melanoma single cell datasets to the unique developmental stages of T1 and T2 lineages will be necessary to determine whether trajectory specific identities appear upon melanoma dedifferentiation. Nonetheless, the presence of transcriptionally T1- and T2-like melanocytes into adulthood offer new insight into origins of heterogeneity in melanoma cases.

In conclusion, our findings highlight the utility of directed stem cell differentiations as models of human neural crest development and provide a platform for developing in-depth mechanistic understandings of NC diversification, cell fate decisions, lineage progression and restriction. Furthermore, our new T2 melanocyte differentiation strategy allows for the first comparison of NC- and SCP-derived melanocytes and provides comprehensive *in vitro* melanocyte models necessary for disease modeling and drug discovery. Finally, our work proposes developmental origin as a new source of transcriptional and functional heterogeneity and survival outcomes in melanoma and provides a basis for selection of origin specific gene targets for personalized treatment. As the NC field continues to utilize these stem cell derived models of NC development to complement *in vivo* models, we will develop a more thorough understanding of NC biology in development and disease, ultimately leading to novel treatments of neurocristopathy and NC-derived tumor targeted therapies.

References

1. Bronner ME, LeDouarin NM. Evolution and Development of the Neural Crest: An Overview. *Dev Biol*. 2012;366(1):2-9. doi:10.1016/j.ydbio.2011.12.042

2. Tam PPL, Loebel DAF. Gene function in mouse embryogenesis: get set for gastrulation. *Nat Rev Genet*. 2007;8(5):368-381. doi:10.1038/nrg2084

3. Thawani A, Groves AK. Building the Border: Development of the Chordate Neural Plate Border Region and Its Derivatives. *Front Physiol*. 2020;11. Accessed May 3, 2023. https://www.frontiersin.org/articles/10.3389/fphys.2020.608880

4. Sambasivan R, Steventon B. Neuromesodermal Progenitors: A Basis for Robust Axial Patterning in Development and Evolution. *Front Cell Dev Biol*. 2021;8. Accessed May 3, 2023. https://www.frontiersin.org/articles/10.3389/fcell.2020.607516

5. Aulehla A, Pourquié O. Signaling Gradients during Paraxial Mesoderm Development. *Cold Spring Harb Perspect Biol*. 2010;2(2):a000869. doi:10.1101/cshperspect.a000869

6. Bedois AMH, Parker HJ, Krumlauf R. Retinoic Acid Signaling in Vertebrate Hindbrain Segmentation: Evolution and Diversification. *Diversity*. 2021;13(8):398. doi:10.3390/d13080398

7. Bayha E, Jørgensen MC, Serup P, Grapin-Botton A. Retinoic Acid Signaling Organizes Endodermal Organ Specification along the Entire Antero-Posterior Axis. *PLOS ONE*. 2009;4(6):e5845. doi:10.1371/journal.pone.0005845

8. Nolte C, De Kumar B, Krumlauf R. Hox genes: Downstream “effectors” of retinoic acid signaling in vertebrate embryogenesis. *genesis*. 2019;57(7-8):e23306. doi:10.1002/dvg.23306

9. Afzal Z, Krumlauf R. Transcriptional Regulation and Implications for Controlling Hox Gene Expression. *J Dev Biol*. 2022;10(1):4. doi:10.3390/jdb10010004

10. Rothstein M, Bhattacharya D, Simoes-Costa M. The molecular basis of neural crest axial identity. *Dev Biol*. 2018;444:S170-S180. doi:10.1016/j.ydbio.2018.07.026

11. Cunningham TJ, Duester G. Mechanisms of retinoic acid signalling and its roles in organ and limb development. *Nat Rev Mol Cell Biol*. 2015;16(2):110-123. doi:10.1038/nrm3932

12. Couly GF, Coltey PM, Douarin NML. The triple origin of skull in higher vertebrates: a study in quail-chick chimeras. *Development*. 1993;117(2):409-429. doi:10.1242/dev.117.2.409

13. Köntges G, Lumsden A. Rhombencephalic neural crest segmentation is preserved throughout craniofacial ontogeny. *Development*. 1996;122(10):3229-3242. doi:10.1242/dev.122.10.3229

14. Couly G, Coltey P, Eichmann A, Le Douarin NM. The angiogenic potentials of the cephalic mesoderm and the origin of brain and head blood vessels. *Mech Dev*. 1995;53(1):97-112. doi:10.1016/0925-4773(95)00428-9

15. Lièvre CSL, Douarin NML. Mesenchymal derivatives of the neural crest: analysis of chimaeric quail and chick embryos. *Development*. 1975;34(1):125-154. doi:10.1242/dev.34.1.125

16. Kuo BR, Erickson CA. Regional differences in neural crest morphogenesis. *Cell Adhes Migr*. 2010;4(4):567-585. doi:10.4161/cam.4.4.12890

17. Lumsden A, Sprawson N, Graham A. Segmental origin and migration of neural crest cells in the hindbrain region of the chick embryo. *Development*. 1991;113(4):1281-1291. doi:10.1242/dev.113.4.1281

18. Noden DM. The role of the neural crest in patterning of avian cranial skeletal, connective, and muscle tissues. *Dev Biol*. 1983;96(1):144-165. doi:10.1016/0012-1606(83)90318-4

19. Graham A, Begbie J, McGonnell I. Significance of the cranial neural crest. *Dev Dyn*. 2004;229(1):5-13. doi:10.1002/dvdy.10442

20. Hutchins EJ, Kunttas E, Piacentino ML, Howard AGA, Bronner ME, Uribe RA. Migration and diversification of the vagal neural crest. *Dev Biol*. 2018;444:S98-S109. doi:10.1016/j.ydbio.2018.07.004

21. Kirby ML, Gale TF, Stewart DE. Neural Crest Cells Contribute to Normal Aorticopulmonary Septation. *Science*. 1983;220(4601):1059-1061. doi:10.1126/science.6844926

22. Kirby ML, Stewart DE. Neural crest origin of cardiac ganglion cells in the chick embryo: Identification and extirpation. *Dev Biol*. 1983;97(2):433-443. doi:10.1016/0012-1606(83)90100-8

23. Miyagawa-Tomita S, Waldo K, Tomita H, Kirby ML. Temporospatial study of the migration and distribution of cardiac neural crest in quail-chick chimeras. *Am J Anat*. 1991;192(1):79-88. doi:10.1002/aja.1001920109

24. Yntema CL, Hammond WS. The origin of intrinsic ganglia of trunk viscera from vagal neural crest in the chick embryo. *J Comp Neurol*. 1954;101(2):515-541. doi:10.1002/cne.901010212

25. Douarin NML, Teillet MA. The migration of neural crest cells to the wall of the digestive tract in avian embryo. *Development*. 1973;30(1):31-48. doi:10.1242/dev.30.1.31

26. Epstein ML, Mikawa T, Brown AMC, McFarlin DR. Mapping the origin of the avian enteric nervous system with a retroviral marker. *Dev Dyn*. 1994;201(3):236-244. doi:10.1002/aja.1002010307

27. Reedy MV, Faraco CD, Erickson CA. The Delayed Entry of Thoracic Neural Crest Cells into the Dorsolateral Path Is a Consequence of the Late Emigration of Melanogenic Neural Crest Cells from the Neural Tube. *Dev Biol*. 1998;200(2):234-246. doi:10.1006/dbio.1998.8963

28. Loring JF, Erickson CA. Neural crest cell migratory pathways in the trunk of the chick embryo. *Dev Biol*. 1987;121(1):220-236. doi:10.1016/0012-1606(87)90154-0

29. Debby-Brafman A, Burstyn-Cohen T, Klar A, Kalcheim C. F-Spondin, Expressed in Somite Regions Avoided by Neural Crest Cells, Mediates Inhibition of Distinct Somite Domains to Neural Crest Migration. *Neuron*. 1999;22(3):475-488. doi:10.1016/S0896-6273(00)80703-5

30. Kalcheim C, Teillet MA. Consequences of somite manipulation on the pattern of dorsal root ganglion development. *Development*. 1989;106(1):85-93. doi:10.1242/dev.106.1.85

31. Lallier TE, Bronner-Fraser M. A spatial and temporal analysis of dorsal root and sympathetic ganglion formation in the avian embryo. *Dev Biol*. 1988;127(1):99-112. doi:10.1016/0012-1606(88)90192-3

32. Artinger KB, Bronner-Fraser M. Partial restriction in the developmental potential of late emigrating avian neural crest cells. *Dev Biol*. 1992;149(1):149-157. doi:10.1016/0012-1606(92)90271-H

33. Douarin NL, Kalcheim C. *The Neural Crest*. Cambridge University Press; 1999.

34. Henion PD, Weston JA. Timing and pattern of cell fate restrictions in the neural crest lineage. *Dev Camb Engl*. 1997;124(21):4351-4359. doi:10.1242/dev.124.21.4351

35. Burns AJ, Champeval D, Le Douarin NM. Sacral Neural Crest Cells Colonise Aganglionic Hindgut in Vivo but Fail to Compensate for Lack of Enteric Ganglia. *Dev Biol*. 2000;219(1):30-43. doi:10.1006/dbio.1999.9592

36. Erickson CA, Goins TL. Sacral Neural Crest Cell Migration to the Gut Is Dependent upon the Migratory Environment and Not Cell-Autonomous Migratory Properties. *Dev Biol*. 2000;219(1):79-97. doi:10.1006/dbio.1999.9597

37. Tang W, Jacobs-Li J, Li C, Bronner ME. Single-cell profiling coupled with lineage analysis reveals distinct sacral neural crest contributions to the developing enteric nervous system. Published online May 10, 2022:2022.05.09.491197. doi:10.1101/2022.05.09.491197

38. Baker CVH, Bronner-Fraser M. The origins of the neural crest. Part I: embryonic induction. *Mech Dev*. 1997;69(1):3-11. doi:10.1016/S0925-4773(97)00132-9

39. Betters E, Liu Y, Kjaeldgaard A, Sundström E, García-Castro MI. Analysis of early human neural crest development. *Dev Biol*. 2010;344(2):578-592. doi:10.1016/j.ydbio.2010.05.012

40. Baker CVH, Bronner-Fraser M, Douarin NML, Teillet MA. Early- and late-migrating cranial neural crest cell populations have equivalent developmental potential in vivo. *Development*. 1997;124(16):3077-3087. doi:10.1242/dev.124.16.3077

41. Espinosa-Medina I, Jevans B, Boismoreau F, et al. Dual origin of enteric neurons in vagal Schwann cell precursors and the sympathetic neural crest. *Proc Natl Acad Sci*. 2017;114(45):11980-11985. doi:10.1073/pnas.1710308114

42. Jessen KR, Mirsky R. Schwann cell precursors and their development. *Glia*. 1991;4(2):185-194. doi:10.1002/glia.440040210

43. Kastriti ME, Adameyko I. Specification, plasticity and evolutionary origin of peripheral glial cells. *Curr Opin Neurobiol*. 2017;47:196-202. doi:10.1016/j.conb.2017.11.004

44. Niederländer C, Lumsden A. Late emigrating neural crest cells migrate specifically to the exit points of cranial branchiomotor nerves. *Development*. 1996;122(8):2367-2374. doi:10.1242/dev.122.8.2367

45. Golding JP, Cohen J. Border Controls at the Mammalian Spinal Cord: Late-Surviving Neural Crest Boundary Cap Cells at Dorsal Root Entry Sites May Regulate Sensory Afferent Ingrowth and Entry Zone Morphogenesis. *Mol Cell Neurosci*. 1997;9(5):381-396. doi:10.1006/mcne.1997.0647

46. Vermeren M, Maro GS, Bron R, et al. Integrity of Developing Spinal Motor Columns Is Regulated by Neural Crest Derivatives at Motor Exit Points. *Neuron*. 2003;37(3):403-415. doi:10.1016/S0896-6273(02)01188-1

47. Gresset A, Coulpier F, Gerschenfeld G, et al. Boundary Caps Give Rise to Neurogenic Stem Cells and Terminal Glia in the Skin. *Stem Cell Rep*. 2015;5(2):278-290. doi:10.1016/j.stemcr.2015.06.005

48. Jessen KR, Mirsky R. Schwann cells: early lineage, regulation of proliferation and control of myelin formation. *Curr Opin Neurobiol*. 1992;2(5):575-581. doi:10.1016/0959-4388(92)90021-c

49. Mirsky R, Jessen KR. Schwann cell development, differentiation and myelination. *Curr Opin Neurobiol*. 1996;6(1):89-96. doi:10.1016/S0959-4388(96)80013-4

50. Furlan A, Adameyko I. Schwann cell precursor: a neural crest cell in disguise? *Dev Biol*. 2018;444:S25-S35. doi:10.1016/j.ydbio.2018.02.008

51. Kastriti ME, Faure L, Von Ahsen D, et al. Schwann cell precursors represent a neural crest-like state with biased multipotency. *EMBO J*. 2022;41(17):e108780. doi:10.15252/embj.2021108780

52. Joseph NM, Mukouyama Y suke, Mosher JT, et al. Neural crest stem cells undergo multilineage differentiation in developing peripheral nerves to generate endoneurial fibroblasts in addition to Schwann cells. *Dev Camb Engl*. 2004;131(22):5599-5612. doi:10.1242/dev.01429

53. Dupin E, Le Douarin NM. Development of melanocyte precursors from the vertebrate neural crest. *Oncogene*. 2003;22(20):3016-3023. doi:10.1038/sj.onc.1206460

54. Adameyko I, Lallemend F, Aquino JB, et al. Schwann Cell Precursors from Nerve Innervation Are a Cellular Origin of Melanocytes in Skin. *Cell*. 2009;139(2):366-379. doi:10.1016/j.cell.2009.07.049

55. Huber K, Kalcheim C, Unsicker K. The development of the chromaffin cell lineage from the neural crest. *Auton Neurosci*. 2009;151(1):10-16. doi:10.1016/j.autneu.2009.07.020

56. Furlan A, Dyachuk V, Kastriti ME, et al. Multipotent Peripheral Glial Cells Generate Neuroendocrine Cells of the Adrenal Medulla. *Science*. 2017;357(6346):eaal3753. doi:10.1126/science.aal3753

57. Espinosa-Medina I, Outin E, Picard CA, et al. Neurodevelopment. Parasympathetic ganglia derive from Schwann cell precursors. *Science*. 2014;345(6192):87-90. doi:10.1126/science.1253286

58. Dyachuk V, Furlan A, Shahidi MK, et al. Parasympathetic neurons originate from nerve-associated peripheral glial progenitors. *Science*. 2014;345(6192):82-87. doi:10.1126/science.1253281

59. Uesaka T, Nagashimada M, Enomoto H. Neuronal Differentiation in Schwann Cell Lineage Underlies Postnatal Neurogenesis in the Enteric Nervous System. *J Neurosci*. 2015;35(27):9879-9888. doi:10.1523/JNEUROSCI.1239-15.2015

60. Xie M, Kamenev D, Kaucka M, et al. Schwann cell precursors contribute to skeletal formation during embryonic development in mice and zebrafish. *Proc Natl Acad Sci U S A*. 2019;116(30):15068-15073. doi:10.1073/pnas.1900038116

61. Kaukua N, Shahidi MK, Konstantinidou C, et al. Glial origin of mesenchymal stem cells in a tooth model system. *Nature*. 2014;513(7519):551-554. doi:10.1038/nature13536

62. Tam PP, Trainor PA. Specification and segmentation of the paraxial mesoderm. *Anat Embryol (Berl)*. 1994;189(4):275-305. doi:10.1007/BF00190586

63. Petersen J, Adameyko I. Nerve-associated neural crest: peripheral glial cells generate multiple fates in the body. *Curr Opin Genet Dev*. 2017;45:10-14. doi:10.1016/j.gde.2017.02.006

64. Solovieva T, Bronner M. Schwann cell precursors: where they come from and where they go. *Cells Dev*. 2021;166:203686. doi:10.1016/j.cdev.2021.203686

65. Tang W, Bronner ME. Neural crest lineage analysis: from past to future trajectory. *Development*. 2020;147(20):dev193193. doi:10.1242/dev.193193

66. Cohen AM, Konigsberg IR. A clonal approach to the problem of neural crest determination. *Dev Biol*. 1975;46(2):262-280. doi:10.1016/0012-1606(75)90104-9

67. Sieber-Blum M, Cohen AM. Clonal analysis of quail neural crest cells: They are pluripotent and differentiate in vitro in the absence of noncrest cells. *Dev Biol*. 1980;80(1):96-106. doi:10.1016/0012-1606(80)90501-1

68. Bronner-Fraser M, Sieber-blum M, Cohen AM. Clonal analysis of the avian neural crest: Migration and maturation of mixed neural crest clones injected into host chicken embryos. *J Comp Neurol*. 1980;193(2):423-434. doi:10.1002/cne.901930209

69. Baroffio A, Dupin E, Le Douarin NM. Clone-forming ability and differentiation potential of migratory neural crest cells. *Proc Natl Acad Sci U S A*. 1988;85(14):5325-5329. doi:10.1073/pnas.85.14.5325

70. Ito K, Sieber-Blum M. Pluripotent and Developmentally Restricted Neural-Crest-Derived Cells in Posterior Visceral Arches. *Dev Biol*. 1993;156(1):191-200. doi:10.1006/dbio.1993.1069

71. Stemple DL, Anderson DJ. Isolation of a stem cell for neurons and glia from the mammalian neural crest. *Cell*. 1992;71(6):973-985. doi:10.1016/0092-8674(92)90393-q

72. Ito K, Morita T, Sieber-Blum M. In Vitro Clonal Analysis of Mouse Neural Crest Development. *Dev Biol*. 1993;157(2):517-525. doi:10.1006/dbio.1993.1154

73. Shah NM, Marchionni MA, Isaacs I, Stroobant P, Anderson DJ. Glial growth factor restricts mammalian neural crest stem cells to a glial fate. *Cell*. 1994;77(3):349-360. doi:10.1016/0092-8674(94)90150-3

74. Shah NM, Groves AK, Anderson DJ. Alternative Neural Crest Cell Fates Are Instructively Promoted by TGFβ Superfamily Members. *Cell*. 1996;85(3):331-343. doi:10.1016/S0092-8674(00)81112-5

75. Lahav R, Dupin E, Lecoin L, et al. Endothelin 3 selectively promotes survival and proliferation of neural crest-derived glial and melanocytic precursors in vitro. *Proc Natl Acad Sci*. 1998;95(24):14214-14219. doi:10.1073/pnas.95.24.14214

76. Le Douarin NM, Teillet MAM. Experimental analysis of the migration and differentiation of neuroblasts of the autonomic nervous system and of neurectodermal mesenchymal derivatives, using a biological cell marking technique. *Dev Biol*. 1974;41(1):162-184. doi:10.1016/0012-1606(74)90291-7

77. Le Lievre CS, Schweizer GG, Ziller CM, Le Douarin NM. Restrictions of developmental capabilities in neural crest cell derivatives as tested by in vivo

transplantation experiments. *Dev Biol*. 1980;77(2):362-378. doi:10.1016/0012-1606(80)90481-9

78. Nakamura H, Lievre CSAL. Mesectodermal capabilities of the trunk neural crest of birds. *Development*. 1982;70(1):1-18. doi:10.1242/dev.70.1.1

79. Chibon P. [Nuclear labelling by tritiated thymidine of neural crest derivatives in the amphibian Urodele Pleurodeles waltlii Michah]. *J Embryol Exp Morphol*. 1967;18(3):343-358.

80. Lwigale PY, Conrad GW, Bronner-Fraser M. Graded potential of neural crest to form cornea, sensory neurons and cartilage along the rostrocaudal axis. *Development*. 2004;131(9):1979-1991. doi:10.1242/dev.01106

81. Kirby ML. Plasticity and predetermination of mesencephalic and trunk neural crest transplanted into the region of the cardiac neural crest. *Dev Biol*. 1989;134(2):402-412. doi:10.1016/0012-1606(89)90112-7

82. Serbedzija GN, Burgan S, Fraser SE, Bronner-Fraser M. Vital dye labelling demonstrates a sacral neural crest contribution to the enteric nervous system of chick and mouse embryos. *Development*. 1991;111(4):857-866. doi:10.1242/dev.111.4.857

83. Serbedzija GN, Bronner-Fraser M, Fraser SE. Vital dye analysis of cranial neural crest cell migration in the mouse embryo. *Development*. 1992;116(2):297-307. doi:10.1242/dev.116.2.297

84. Serbedzija GN, Fraser SE, Bronner-Fraser M. Pathways of trunk neural crest cell migration in the mouse embryo as revealed by vital dye labelling. *Development*. 1990;108(4):605-612. doi:10.1242/dev.108.4.605

85. Serbedzija GN, Bronner-Fraser M, Fraser SE. A vital dye analysis of the timing and pathways of avian trunk neural crest cell migration. *Development*. 1989;106(4):809-816. doi:10.1242/dev.106.4.809

86. Lencer E, Prekeris R, Artinger KB. Single-cell RNA analysis identifies pre-migratory neural crest cells expressing markers of differentiated derivatives. Solnica-Krezel L, White RM, eds. *eLife*. 2021;10:e66078. doi:10.7554/eLife.66078

87. Bronner-Fraser M, Fraser S. Developmental potential of avian trunk neural crest cells in situ. *Neuron*. 1989;3(6):755-766. doi:10.1016/0896-6273(89)90244-4

88. Bronner-Fraser M, Fraser SE. Cell lineage analysis reveals multipotency of some avian neural crest cells. *Nature*. 1988;335(6186):161-164. doi:10.1038/335161a0

89. Baggiolini A, Varum S, Mateos JM, et al. Premigratory and migratory neural crest cells are multipotent in vivo. *Cell Stem Cell*. 2015;16(3):314-322. doi:10.1016/j.stem.2015.02.017

90. Yoshida T, Vivatbutsiri P, Morriss-Kay G, Saga Y, Iseki S. Cell lineage in mammalian craniofacial mesenchyme. *Mech Dev*. 2008;125(9):797-808. doi:10.1016/j.mod.2008.06.007

91. Krispin S, Nitzan E, Kassem Y, Kalcheim C. Evidence for a dynamic spatiotemporal fate map and early fate restrictions of premigratory avian neural crest. *Development*. 2010;137(4):585-595. doi:10.1242/dev.041509

92. Soldatov R, Kaucka M, Kastriti ME, et al. Spatiotemporal structure of cell fate decisions in murine neural crest. *Science*. 2019;364(6444):eaas9536. doi:10.1126/science.aas9536

93. Faure L, Wang Y, Kastriti ME, et al. Single cell RNA sequencing identifies early diversity of sensory neurons forming via bi-potential intermediates. *Nat Commun*. 2020;11(1):4175. doi:10.1038/s41467-020-17929-4

94. Morarach K, Mikhailova A, Knoflach V, et al. Diversification of molecularly defined myenteric neuron classes revealed by single-cell RNA sequencing. *Nat Neurosci*. 2021;24(1):34-46. doi:10.1038/s41593-020-00736-x

95. Kelsh RN, Camargo Sosa K, Farjami S, Makeev V, Dawes JHP, Rocco A. Cyclical fate restriction: a new view of neural crest cell fate specification. *Development*. 2021;148(22):dev176057. doi:10.1242/dev.176057

96. Subkhankulova T, Kelsh RN. Fluorescence-Activated Cell Sorting and NanoString Profiling of Single Neural Crest Cells and Pigment Cells. In: Schwarz Q, Wiszniak S, eds. *Neural Crest Cells: Methods and Protocols*. Methods in Molecular Biology. Springer; 2019:185-193. doi:10.1007/978-1-4939-9412-0_14

97. Sakaue-Sawano A, Kurokawa H, Morimura T, et al. Visualizing Spatiotemporal Dynamics of Multicellular Cell-Cycle Progression. *Cell*. 2008;132(3):487-498. doi:10.1016/j.cell.2007.12.033

98. D'Orazio J, Jarrett S, Amaro-Ortiz A, Scott T. UV Radiation and the Skin. *Int J Mol Sci*. 2013;14(6):12222-12248. doi:10.3390/ijms140612222

99. Maranduca MA, Branisteanu D, Serban DN, et al. Synthesis and physiological implications of melanic pigments. *Oncol Lett*. 2019;17(5):4183-4187. doi:10.3892/ol.2019.10071

100. Tsatmali M, Ancans J, Thody AJ. Melanocyte Function and Its Control by Melanocortin Peptides. *J Histochem Cytochem*. 2002;50(2):125-133. doi:10.1177/002215540205000201

101. Yamaguchi Y, Hearing VJ. Melanocytes and Their Diseases. *Cold Spring Harb Perspect Med*. 2014;4(5):a017046. doi:10.1101/cshperspect.a017046

102. Westerhof W. The discovery of the human melanocyte. *Pigment Cell Res*. 2006;19(3):183-193. doi:10.1111/j.1600-0749.2006.00313.x

103. Rawles ME. Origin of Pigment Cells from the Neural Crest in the Mouse Embryo. *Physiol Zool*. 1947;20(3):248-266. doi:10.1086/physzool.20.3.30151958

104. Rawles ME. Origin of melanophores and their rôle in development of color patterns in vertebrates. *Physiol Rev*. 1948;28(4):383-408. doi:10.1152/physrev.1948.28.4.383

105. Erickson CA, Goins TL. Avian neural crest cells can migrate in the dorsolateral path only if they are specified as melanocytes. *Development*. 1995;121(3):915-924. doi:10.1242/dev.121.3.915

106. Mackenzie MAF, Jordan SA, Budd PS, Jackson IJ. Activation of the Receptor Tyrosine Kinase Kit Is Required for the Proliferation of Melanoblasts in the Mouse Embryo. *Dev Biol*. 1997;192(1):99-107. doi:10.1006/dbio.1997.8738

107. Nakayama A, Nguyen MTT, Chen CC, Opdecamp K, Hodgkinson CA, Arnheiter H. Mutations in microphthalmia, the mouse homolog of the human deafness gene MITF, affect neuroepithelial and neural crest-derived melanocytes differently. *Mech Dev*. 1998;70(1):155-166. doi:10.1016/S0925-4773(97)00188-3

108. Baxter LL, Pavan WJ. Pmel17 expression is Mitf-dependent and reveals cranial melanoblast migration during murine development. *Gene Expr Patterns*. 2003;3(6):703-707. doi:10.1016/j.modgep.2003.07.002

109. Erickson CA, Duong TD, Tosney KW. Descriptive and experimental analysis of the dispersion of neural crest cells along the dorsolateral path and their entry into ectoderm in the chick embryo. *Dev Biol*. 1992;151(1):251-272. doi:10.1016/0012-1606(92)90231-5

110. Weston JA. 6 Sequential Segregation and Fate of Developmentally Restricted Intermediate Cell Populations in the Neural Crest Lineage. In: Bode HR, ed. *Current Topics in Developmental Biology*. Vol 25. Academic Press; 1991:133-153. doi:10.1016/S0070-2153(08)60414-7

111. Wehrle-Haller B, Weston JA. Soluble and cell-bound forms of steel factor activity play distinct roles in melanocyte precursor dispersal and survival on the lateral neural crest migration pathway. *Development*. 1995;121(3):731-742. doi:10.1242/dev.121.3.731

112. Lee HO, Levorse JM, Shin MK. The endothelin receptor-B is required for the migration of neural crest-derived melanocyte and enteric neuron precursors. *Dev Biol*. 2003;259(1):162-175. doi:10.1016/S0012-1606(03)00160-X

113. Shin MK, Levorse JM, Ingram RS, Tilghman SM. The temporal requirement for endothelin receptor-B signalling during neural crest development. *Nature*. 1999;402(6761):496-501. doi:10.1038/990040

114. Yoshida H, Kunisada T, Kusakabe M, Nishikawa S, Nishikawa SI. Distinct stages of melanocyte differentiation revealed by analysis of nonuniform pigmentation patterns. *Development*. 1996;122(4):1207-1214. doi:10.1242/dev.122.4.1207

115. Wehrle-Haller B, Meller M, Weston JA. Analysis of Melanocyte Precursors in Nf1 Mutants Reveals That MGF/KIT Signaling Promotes Directed Cell Migration Independent of Its Function in Cell Survival. *Dev Biol*. 2001;232(2):471-483. doi:10.1006/dbio.2001.0167

116. Takeda K, Yasumoto K ichi, Takada R, et al. Induction of Melanocyte-specific Microphthalmia-associated Transcription Factor by Wnt-3a*. *J Biol Chem*. 2000;275(19):14013-14016. doi:10.1074/jbc.C000113200

117. Garnett AT, Square TA, Medeiros DM. BMP, Wnt and FGF signals are integrated through evolutionarily conserved enhancers to achieve robust expression of Pax3 and Zic genes at the zebrafish neural plate border. *Dev Camb Engl*. 2012;139(22):4220-4231. doi:10.1242/dev.081497

118. Adameyko I, Lallemend F, Furlan A, et al. Sox2 and Mitf cross-regulatory interactions consolidate progenitor and melanocyte lineages in the cranial neural crest. *Dev Camb Engl*. 2012;139(2):397-410. doi:10.1242/dev.065581

119. Nitzan E, Pfaltzgraff ER, Labosky PA, Kalcheim C. Neural crest and Schwann cell progenitor-derived melanocytes are two spatially segregated populations similarly regulated by Foxd3. *Proc Natl Acad Sci U S A*. 2013;110(31):12709-12714. doi:10.1073/pnas.1306287110

120. Kaucka M, Szarowska B, Kavkova M, et al. Nerve-associated Schwann cell precursors contribute extracutaneous melanocytes to the heart, inner ear, supraorbital locations and brain meninges. *Cell Mol Life Sci CMLS*. 2021;78(16):6033-6049. doi:10.1007/s00018-021-03885-9

121. Bonnamour G, Soret R, Pilon N. Dhh-expressing Schwann cell precursors contribute to skin and cochlear melanocytes, but not to vestibular melanocytes. *Pigment Cell Melanoma Res*. 2021;34(3):648-654. doi:10.1111/pcmr.12938

122. Balani K, Brito FC, Kos L, Agarwal A. Melanocyte pigmentation stiffens murine cardiac tricuspid valve leaflet. *J R Soc Interface*. 2009;6(40):1097-1102. doi:10.1098/rsif.2009.0174

123. Hwang H, Liu F, Petrenko NB, Huang J, Schillinger KJ, Patel VV. Cardiac melanocytes influence atrial reactive oxygen species involved with electrical and structural remodeling in mice. *Physiol Rep*. 2015;3(9):e12559. doi:10.14814/phy2.12559

124. Levin MD, Lu MM, Petrenko NB, et al. Melanocyte-like cells in the heart and pulmonary veins contribute to atrial arrhythmia triggers. *J Clin Invest*. 2009;119(11):3420-3436. doi:10.1172/JCI39109

125. Tachibana M. Sound Needs Sound Melanocytes to Be Heard. *Pigment Cell Res*. 1999;12(6):344-354. doi:10.1111/j.1600-0749.1999.tb00518.x

126. Steel KP, Barkway C. Another role for melanocytes: their importance for normal stria vascularis development in the mammalian inner ear. *Development*. 1989;107(3):453-463. doi:10.1242/dev.107.3.453

127. Motohashi H, Hozawa K, Oshima T, Takeuchi T, Takasaka T. Dysgenesis of melanocytes and cochlear dysfunction in mutant microphthalmia (mi) mice. *Hear Res*. 1994;80(1):10-20. doi:10.1016/0378-5955(94)90003-5

128. Murillo-Cuesta S, Contreras J, Zurita E, et al. Melanin precursors prevent premature age-related and noise-induced hearing loss in albino mice. *Pigment Cell Melanoma Res*. 2010;23(1):72-83. doi:10.1111/j.1755-148X.2009.00646.x

129. Gudjohnsen SAH, Atacho DAM, Gesbert F, et al. Meningeal Melanocytes in the Mouse: Distribution and Dependence on Mitf. *Front Neuroanat*. 2015;9:149. doi:10.3389/fnana.2015.00149

130. Baxter LL, Moreland RT, Nguyen AD, Wolfsberg TG, Pavan WJ. A curated online resource for SOX10 and pigment cell molecular genetic pathways. *Database*. 2010;2010:baq025. doi:10.1093/database/baq025

131. Steingrímsson E, Copeland NG, Jenkins NA. Melanocytes and the Microphthalmia Transcription Factor Network. *Annu Rev Genet*. 2004;38(1):365-411. doi:10.1146/annurev.genet.38.072902.092717

132. Béjar J, Hong Y, Schartl M. Mitf expression is sufficient to direct differentiation of medaka blastula derived stem cells to melanocytes. *Development*. 2003;130(26):6545-6553. doi:10.1242/dev.00872

133. Tachibana M, Takeda K, Nobukuni Y, et al. Ectopic expression of MITF, a gene for Waardenburg syndrome type 2, converts fibroblasts to cells with melanocyte characteristics. *Nat Genet*. 1996;14(1):50-54. doi:10.1038/ng0996-50

134. Potterf SB, Furumura M, Dunn KJ, Arnheiter H, Pavan WJ. Transcription factor hierarchy in Waardenburg syndrome: regulation of MITF expression by SOX10 and PAX3. *Hum Genet*. 2000;107(1):1-6. doi:10.1007/s004390000328

135. Watanabe K ichi, Takeda K, Yasumoto K ichi, et al. Identification of a Distal Enhancer for the Melanocyte-Specific Promoter of the MITF Gene. *Pigment Cell Res*. 2002;15(3):201-211. doi:10.1034/j.1600-0749.2002.01080.x

136. Bondurand N, Pingault V, Goerich DE, et al. Interaction among SOX10, PAX3 and MITF, three genes altered in Waardenburg syndrome. *Hum Mol Genet*. 2000;9(13):1907-1917. doi:10.1093/hmg/9.13.1907

137. Kos R, Reedy MV, Johnson RL, Erickson CA. The winged-helix transcription factor FoxD3 is important for establishing the neural crest lineage and repressing melanogenesis in avian embryos. *Development*. 2001;128(8):1467-1479. doi:10.1242/dev.128.8.1467

138. Cheli Y, Ohanna M, Ballotti R, Bertolotto C. Fifteen-year quest for microphthalmia-associated transcription factor target genes. *Pigment Cell Melanoma Res*. 2010;23(1):27-40. doi:10.1111/j.1755-148X.2009.00653.x

139. Belote RL, Le D, Maynard A, et al. Human melanocyte development and melanoma dedifferentiation at single-cell resolution. *Nat Cell Biol*. 2021;23(9):1035-1047. doi:10.1038/s41556-021-00740-8

140. Weiss JM, Hunter MV, Cruz NM, et al. Anatomic position determines oncogenic specificity in melanoma. *Nature*. 2022;604(7905):354-361. doi:10.1038/s41586-022-04584-6

141. Baxter LL, Watkins-Chow DE, Pavan WJ, Loftus SK. A curated gene list for expanding the horizons of pigmentation biology. *Pigment Cell Melanoma Res*. 2019;32(3):348-358. doi:10.1111/pcmr.12743

142. Skin Pigment Disorders. Published February 28, 2020. Accessed May 4, 2023. https://www.hopkinsmedicine.org/health/conditions-and-diseases/skin-pigment-disorders

143. Watt B, Tenza D, Lemmon MA, et al. Mutations in or near the Transmembrane Domain Alter PMEL Amyloid Formation from Functional to Pathogenic. *PLoS Genet*. 2011;7(9):e1002286. doi:10.1371/journal.pgen.1002286

144. Dolinska MB, Kovaleva E, Backlund P, Wingfield PT, Brooks BP, Sergeev YV. Albinism-Causing Mutations in Recombinant Human Tyrosinase Alter Intrinsic Enzymatic Activity. *PLoS ONE*. 2014;9(1):e84494. doi:10.1371/journal.pone.0084494

145. Costin GE, Valencia JC, Wakamatsu K, et al. Mutations in dopachrome tautomerase (Dct) affect eumelanin/pheomelanin synthesis, but do not affect intracellular trafficking of the mutant protein. *Biochem J*. 2005;391(Pt 2):249-259. doi:10.1042/BJ20042070

146. James WD, Elston D, Treat JR, Rosenbach MA. *Andrews' Diseases of the Skin: Clinical Dermatology*. Elsevier Health Sciences; 2019.

147. Albinism - Symptoms and causes. Mayo Clinic. Accessed May 4, 2023. https://www.mayoclinic.org/diseases-conditions/albinism/symptoms-causes/syc-20369184

148. Vitiligo - Symptoms and causes. Mayo Clinic. Accessed May 4, 2023. https://www.mayoclinic.org/diseases-conditions/vitiligo/symptoms-causes/syc-20355912

149. Hemminki A, Markie D, Tomlinson I, et al. A serine/threonine kinase gene defective in Peutz–Jeghers syndrome. *Nature*. 1998;391(6663):184-187. doi:10.1038/34432

150. Pingault V, Bondurand N, Kuhlbrodt K, et al. SOX10 mutations in patients with Waardenburg-Hirschsprung disease. *Nat Genet*. 1998;18(2):171-173. doi:10.1038/ng0298-171

151. Tassabehji M, Newton VE, Read AP. Waardenburg syndrome type 2 caused by mutations in the human microphthalmia (MITF) gene. *Nat Genet*. 1994;8(3):251-255. doi:10.1038/ng1194-251

152. Shin MK, Russell LB, Tilghman SM. Molecular characterization of four induced alleles at the Ednrb locus. *Proc Natl Acad Sci*. 1997;94(24):13105-13110. doi:10.1073/pnas.94.24.13105

153. Giebel LB, Spritz RA. Mutation of the KIT (mast/stem cell growth factor receptor) protooncogene in human piebaldism. *Proc Natl Acad Sci*. 1991;88(19):8696-8699. doi:10.1073/pnas.88.19.8696

154. Hosoda K, Hammer RE, Richardson JA, et al. Targeted and natural (piebald-lethal) mutations of endothelin-B receptor gene produce megacolon associated with spotted coat color in mice. *Cell*. 1994;79(7):1267-1276. doi:10.1016/0092-8674(94)90017-5

155. Yamataka A, Kato Y, Tibboel D, et al. A lack of intestinal pacemaker (c-kit) in aganglionic bowel of patients with Hirschsprung's disease. *J Pediatr Surg*. 1995;30(3):441-444. doi:10.1016/0022-3468(95)90051-9

156. Amiel J, Watkin PM, Tassabehji M, Read AP, Winter RM. Mutation of the MITF gene in albinism-deafness syndrome (Tietz syndrome). *Clin Dysmorphol*. 1998;7(1):17-20.

157. Fang W, Yang P. Vogt-Koyanagi-Harada Syndrome. *Curr Eye Res*. 2008;33(7):517-523. doi:10.1080/02713680802233968

158. Andrade A, Pithon M. Alezzandrini Syndrome: Report of a Sixth Clinical Case. *Dermatology*. 2010;222(1):8-9. doi:10.1159/000321714

159. Gupta M, Pande D, Lehl SS, Sachdev A. Alezzandrini syndrome. *Case Rep*. 2011;2011:bcr0420114052. doi:10.1136/bcr.04.2011.4052

160. Gross A, Kunze J, Maier RF, Stoltenburg-Didinger G, Grimmer I, Obladen M. Autosomal-recessive neural crest syndrome with albinism, black lock, cell migration disorder of the neurocytes of the gut, and deafness: ABCD syndrome. *Am J Med Genet*. 1995;56(3):322-326. doi:10.1002/ajmg.1320560322

161. Plensdorf S, Livieratos M, Dada N. Pigmentation Disorders: Diagnosis and Management. *Am Fam Physician*. 2017;96(12):797-804.

162. DailyMed - TRI-LUMA- fluocinolone acetonide, hydroquinone, and tretinoin cream. Accessed May 4, 2023. https://dailymed.nlm.nih.gov/dailymed/drugInfo.cfm?setid=a35fa709-5eb5-4429-b38f-f1e0019bf0ee

163. Banerjee K, Barbhuiya JN, Ghosh AP, Dey SK, Karmakar PR. The efficacy of low-dose oral corticosteroids in the treatment of vitiligo patient. *Indian J Dermatol Venereol Leprol*. 2003;69(2):135-137.

164. BLEEHEN SS. The treatment of vitiligo with topical corticosteroids: LIGHT AND ELECTRONM ICROSCOPI C STUDIES. *Br J Dermatol*. 1976;94(s12):43-50. doi:10.1111/j.1365-2133.1976.tb02268.x

165. Löntz W, Olsson MJ, Moellmann G, Lerner AB. Pigment cell transplantation for treatment of vitiligo: A progress report. *J Am Acad Dermatol*. 1994;30(4):591-597. doi:10.1016/S0190-9622(94)70067-2

166. Varaschin FZ, Ayoub CA, Liezer NF, Luciano METD. Padrão de repigmentação em um paciente com vitiligo após a utilização de células tronco. *Surg Cosmet Dermatol*. 2017;9(3):269-271. doi:10.5935/scd1984-8773.201793923

167. Challa A, Chauhan S, Pangti R, et al. Evaluation of clinical efficacy and laboratory indicators of non-cultured epidermal cell suspension and hair follicle cell suspension in surgical management of stable vitiligo: A randomized comparative trial. *J Cosmet Dermatol*. 2022;21(12):6958-6964. doi:10.1111/jocd.15407

168. Tsao H, Chin L, Garraway LA, Fisher DE. Melanoma: from mutations to medicine. *Genes Dev*. 2012;26(11):1131-1155. doi:10.1101/gad.191999.112

169. Hayward NK, Wilmott JS, Waddell N, et al. Whole-genome landscapes of major melanoma subtypes. *Nature*. 2017;545(7653):175-180. doi:10.1038/nature22071

170. Hawryluk EB, Tsao H. Melanoma: Clinical Features and Genomic Insights. *Cold Spring Harb Perspect Med*. 2014;4(9):a015388. doi:10.1101/cshperspect.a015388

171. Malta TM, Sokolov A, Gentles AJ, et al. Machine Learning Identifies Stemness Features Associated with Oncogenic Dedifferentiation. *Cell*. 2018;173(2):338-354.e15. doi:10.1016/j.cell.2018.03.034

172. White RM, Zon LI. Melanocytes in Development, Regeneration, and Cancer. *Cell Stem Cell*. 2008;3(3):242-252. doi:10.1016/j.stem.2008.08.005

173. Shakhova O. Neural crest stem cells in melanoma development. *Curr Opin Oncol*. 2014;26(2):215. doi:10.1097/CCO.0000000000000046

174. Kaufman CK, Mosimann C, Fan ZP, et al. A zebrafish melanoma model reveals emergence of neural crest identity during melanoma initiation. *Science*. 2016;351(6272):aad2197. doi:10.1126/science.aad2197

175. Franzese C, Stefanini S, Scorsetti M. Radiation Therapy in the Management of Adrenal Metastases. *Semin Radiat Oncol*. 2023;33(2):193-202. doi:10.1016/j.semradonc.2022.11.001

176. Pham JP, Joshua AM, da Silva IP, Dummer R, Goldinger SM. Chemotherapy in Cutaneous Melanoma: Is There Still a Role? *Curr Oncol Rep*. Published online March 29, 2023. doi:10.1007/s11912-023-01385-6

177. Széles Á, Fazekas T, Váncsa S, et al. Pre-treatment soluble PD-L1 as a predictor of overall survival for immune checkpoint inhibitor therapy: a systematic review and

meta-analysis. *Cancer Immunol Immunother*. 2023;72(5):1061-1073. doi:10.1007/s00262-022-03328-9

178. Gouda MA, Subbiah V. Precision oncology for BRAF-mutant cancers with BRAF and MEK inhibitors: from melanoma to tissue-agnostic therapy. *ESMO Open*. 2023;8(2):100788. doi:10.1016/j.esmoop.2023.100788

179. Pham DDM, Guhan S, Tsao H. KIT and Melanoma: Biological Insights and Clinical Implications. *Yonsei Med J*. 2020;61(7):562-571. doi:10.3349/ymj.2020.61.7.562

180. Menzer C, Hassel JC. Targeted Therapy for Melanomas Without BRAF V600 Mutations. *Curr Treat Options Oncol*. 2022;23(6):831-842. doi:10.1007/s11864-022-00946-4

181. Rabbie R, Ferguson P, Molina-Aguilar C, Adams DJ, Robles-Espinoza CD. Melanoma subtypes: genomic profiles, prognostic molecular markers and therapeutic possibilities. *J Pathol*. 2019;247(5):539-551. doi:10.1002/path.5213

182. Grzywa TM, Paskal W, Włodarski PK. Intratumor and Intertumor Heterogeneity in Melanoma. *Transl Oncol*. 2017;10(6):956-975. doi:10.1016/j.tranon.2017.09.007

183. Alexandrov LB, Nik-Zainal S, Wedge DC, et al. Signatures of mutational processes in human cancer. *Nature*. 2013;500(7463):415-421. doi:10.1038/nature12477

184. Akbani R, Akdemir KC, Aksoy BA, et al. Genomic Classification of Cutaneous Melanoma. *Cell*. 2015;161(7):1681-1696. doi:10.1016/j.cell.2015.05.044

185. Müller J, Krijgsman O, Tsoi J, et al. Low MITF/AXL ratio predicts early resistance to multiple targeted drugs in melanoma. *Nat Commun*. 2014;5(1):5712. doi:10.1038/ncomms6712

186. Garraway LA, Widlund HR, Rubin MA, et al. Integrative genomic analyses identify MITF as a lineage survival oncogene amplified in malignant melanoma. *Nature*. 2005;436(7047):117-122. doi:10.1038/nature03664

187. Jönsson G, Busch C, Knappskog S, et al. Gene Expression Profiling–Based Identification of Molecular Subtypes in Stage IV Melanomas with Different Clinical Outcome. *Clin Cancer Res*. 2010;16(13):3356-3367. doi:10.1158/1078-0432.CCR-09-2509

188. Rambow F, Rogiers A, Marin-Bejar O, et al. Toward Minimal Residual Disease-Directed Therapy in Melanoma. *Cell*. 2018;174(4):843-855.e19. doi:10.1016/j.cell.2018.06.025

189. Harbst K, Staaf J, Lauss M, et al. Molecular Profiling Reveals Low- and High-Grade Forms of Primary Melanoma. *Clin Cancer Res*. 2012;18(15):4026-4036. doi:10.1158/1078-0432.CCR-12-0343

190. Lauss M, Nsengimana J, Staaf J, Newton-Bishop J, Jönsson G. Consensus of Melanoma Gene Expression Subtypes Converges on Biological Entities. *J Invest Dermatol*. 2016;136(12):2502-2505. doi:10.1016/j.jid.2016.05.119

191. Gerami P, Cook RW, Russell MC, et al. Gene expression profiling for molecular staging of cutaneous melanoma in patients undergoing sentinel lymph node

biopsy. *J Am Acad Dermatol*. 2015;72(5):780-785.e3. doi:10.1016/j.jaad.2015.01.009

192. Jaeger J, Koczan D, Thiesen HJ, et al. Gene Expression Signatures for Tumor Progression, Tumor Subtype, and Tumor Thickness in Laser-Microdissected Melanoma Tissues. *Clin Cancer Res*. 2007;13(3):806-815. doi:10.1158/1078-0432.CCR-06-1820

193. Scatolini M, Grand MM, Grosso E, et al. Altered molecular pathways in melanocytic lesions. *Int J Cancer*. 2010;126(8):1869-1881. doi:10.1002/ijc.24899

194. Mauerer A, Roesch A, Hafner C, et al. Identification of new genes associated with melanoma. *Exp Dermatol*. 2011;20(6):502-507. doi:10.1111/j.1600-0625.2011.01254.x

195. Bittner M, Meltzer P, Chen Y, et al. Molecular classification of cutaneous malignant melanoma by gene expression profiling. *Nature*. 2000;406(6795):536-540. doi:10.1038/35020115

196. Onken MD, Worley LA, Ehlers JP, Harbour JW. Gene Expression Profiling in Uveal Melanoma Reveals Two Molecular Classes and Predicts Metastatic Death. *Cancer Res*. 2004;64(20):7205-7209. doi:10.1158/0008-5472.CAN-04-1750

197. Haqq C, Nosrati M, Sudilovsky D, et al. The gene expression signatures of melanoma progression. *Proc Natl Acad Sci*. 2005;102(17):6092-6097. doi:10.1073/pnas.0501564102

198. Smith AP, Hoek K, Becker D. Whole-genome expression profiling of the melanoma progression pathway reveals marked molecular differences between nevi/melanoma in situ and advanced-stage melanomas. *Cancer Biol Ther*. 2005;4(9):1018-1029. doi:10.4161/cbt.4.9.2165

199. Long GV, Weber JS, Infante JR, et al. Overall Survival and Durable Responses in Patients With BRAF V600–Mutant Metastatic Melanoma Receiving Dabrafenib Combined With Trametinib. *J Clin Oncol*. 2016;34(8):871-878. doi:10.1200/JCO.2015.62.9345

200. Catalanotti F, Cheng DT, Shoushtari AN, et al. PTEN Loss-of-Function Alterations Are Associated With Intrinsic Resistance to BRAF Inhibitors in Metastatic Melanoma. *JCO Precis Oncol*. 2017;(1):1-15. doi:10.1200/PO.16.00054

201. Smith MP, Ferguson J, Arozarena I, et al. Effect of SMURF2 Targeting on Susceptibility to MEK Inhibitors in Melanoma. *JNCI J Natl Cancer Inst*. 2013;105(1):33-46. doi:10.1093/jnci/djs471

202. Van Allen EM, Wagle N, Sucker A, et al. The Genetic Landscape of Clinical Resistance to RAF Inhibition in Metastatic Melanoma. *Cancer Discov*. 2014;4(1):94-109. doi:10.1158/2159-8290.CD-13-0617

203. Liang WS, Hendricks W, Kiefer J, et al. Integrated genomic analyses reveal frequent TERT aberrations in acral melanoma. *Genome Res*. 2017;27(4):524-532. doi:10.1101/gr.213348.116

204. de Lima Vazquez V, Vicente AL, Carloni A, et al. Molecular profiling, including TERT promoter mutations, of acral lentiginous melanomas. *Melanoma Res*. 2016;26(2):93. doi:10.1097/CMR.0000000000000222

205. Curtin JA, Busam K, Pinkel D, Bastian BC. Somatic Activation of KIT in Distinct Subtypes of Melanoma. *J Clin Oncol*. 2006;24(26):4340-4346. doi:10.1200/JCO.2006.06.2984

206. Kabbarah O, Chin L. Revealing the genomic heterogeneity of melanoma. *Cancer Cell*. 2005;8(6):439-441. doi:10.1016/j.ccr.2005.11.008

207. Moore AR, Ceraudo E, Sher JJ, et al. Recurrent activating mutations of G-protein-coupled receptor CYSLTR2 in uveal melanoma. *Nat Genet*. 2016;48(6):675-680. doi:10.1038/ng.3549

208. Helgadottir H, Höiom V. The genetics of uveal melanoma: current insights. *Appl Clin Genet*. 2016;9:147-155. doi:10.2147/TACG.S69210

209. Robertson AG, Shih J, Yau C, et al. Integrative Analysis Identifies Four Molecular and Clinical Subsets in Uveal Melanoma. *Cancer Cell*. 2017;32(2):204-220.e15. doi:10.1016/j.ccell.2017.07.003

210. Harbour JW, Onken MD, Roberson EDO, et al. Frequent Mutation of BAP1 in Metastasizing Uveal Melanomas. *Science*. 2010;330(6009):1410-1413. doi:10.1126/science.1194472

211. Kalirai H, Dodson A, Faqir S, Damato BE, Coupland SE. Lack of BAP1 protein expression in uveal melanoma is associated with increased metastatic risk and has utility in routine prognostic testing. *Br J Cancer*. 2014;111(7):1373-1380. doi:10.1038/bjc.2014.417

212. Royer-Bertrand B, Torsello M, Rimoldi D, et al. Comprehensive Genetic Landscape of Uveal Melanoma by Whole-Genome Sequencing. *Am J Hum Genet*. 2016;99(5):1190-1198. doi:10.1016/j.ajhg.2016.09.008

213. Decatur CL, Ong E, Garg N, et al. Driver Mutations in Uveal Melanoma: Associations With Gene Expression Profile and Patient Outcomes. *JAMA Ophthalmol*. 2016;134(7):728-733. doi:10.1001/jamaophthalmol.2016.0903

214. Bornfeld N, Prescher G, Becher R, Hirche H, Jöckel KH, Horsthemke B. Prognostic implications of monosomy 3 in uveal melanoma. *The Lancet*. 1996;347(9010):1222-1225. doi:10.1016/S0140-6736(96)90736-9

215. Abdel-Rahman MH, Christopher BN, Faramawi MF, et al. Frequency, molecular pathology and potential clinical significance of partial chromosome 3 aberrations in uveal melanoma. *Mod Pathol*. 2011;24(7):954-962. doi:10.1038/modpathol.2011.51

216. Dogrusöz M, Bagger M, van Duinen SG, et al. The Prognostic Value of AJCC Staging in Uveal Melanoma Is Enhanced by Adding Chromosome 3 and 8q Status. *Invest Ophthalmol Vis Sci*. 2017;58(2):833-842. doi:10.1167/iovs.16-20212

217. Mihajlovic M, Vlajkovic S, Jovanovic P, Stefanovic V. Primary mucosal melanomas: a comprehensive review. *Int J Clin Exp Pathol*. 2012;5(8):739-753.

218. Postow MA, Hamid O, Carvajal RD. Mucosal Melanoma: Pathogenesis, Clinical Behavior, and Management. *Curr Oncol Rep*. 2012;14(5):441-448. doi:10.1007/s11912-012-0244-x

219. Furney SJ, Turajlic S, Stamp G, et al. Genome sequencing of mucosal melanomas reveals that they are driven by distinct mechanisms from cutaneous melanoma. *J Pathol*. 2013;230(3):261-269. doi:10.1002/path.4204

220. Yun J, Lee J, Jang J, et al. KIT amplification and gene mutations in acral/mucosal melanoma in Korea. *APMIS*. 2011;119(6):330-335. doi:10.1111/j.1600-0463.2011.02737.x

221. Kim KB, Alrwas A. Treatment of KIT -mutated metastatic mucosal melanoma. *Chin Clin Oncol*. 2014;3(3):35-35. doi:10.3978/j.issn.2304-3865.2014.08.02

222. Durante MA, Rodriguez DA, Kurtenbach S, et al. Single-cell analysis reveals new evolutionary complexity in uveal melanoma. *Nat Commun*. 2020;11(1):496. doi:10.1038/s41467-019-14256-1

223. Jerby-Arnon L, Shah P, Cuoco MS, et al. A Cancer Cell Program Promotes T Cell Exclusion and Resistance to Checkpoint Blockade. *Cell*. 2018;175(4):984-997.e24. doi:10.1016/j.cell.2018.09.006

224. Tirosh I, Izar B, Prakadan SM, et al. Dissecting the multicellular ecosystem of metastatic melanoma by single-cell RNA-seq. *Science*. 2016;352(6282):189-196. doi:10.1126/science.aad0501

225. Wouters J, Kalender-Atak Z, Minnoye L, et al. Robust gene expression programs underlie recurrent cell states and phenotype switching in melanoma. *Nat Cell Biol*. 2020;22(8):986-998. doi:10.1038/s41556-020-0547-3

226. Smalley I, Chen Z, Phadke M, et al. Single-Cell Characterization of the Immune Microenvironment of Melanoma Brain and Leptomeningeal Metastases. *Clin Cancer Res*. 2021;27(14):4109-4125. doi:10.1158/1078-0432.CCR-21-1694

227. Groves AK, Bronner-Fraser M. 7 Neural Crest Diversification. In: Pedersen RA, Schatten GP, eds. *Current Topics in Developmental Biology*. Vol 43. Academic Press; 1998:221-258. doi:10.1016/S0070-2153(08)60383-X

228. Biology S for D. *The Emergence of Order in Developing Systems*. Academic Press; 1968.

229. Williams RM, Lukoseviciute M, Sauka-Spengler T, Bronner ME. Single-cell atlas of early chick development reveals gradual segregation of neural crest lineage from the neural plate border during neurulation. Tam PP, Cheah KSE, eds. *eLife*. 2022;11:e74464. doi:10.7554/eLife.74464

230. Chen W, Liu X, Li W, et al. Single-cell transcriptomic landscape of cardiac neural crest cell derivatives during development. *EMBO Rep*. 2021;22(11):e52389. doi:10.15252/embr.202152389

231. Fabian P, Tseng KC, Thiruppathy M, et al. Lifelong single-cell profiling of cranial neural crest diversification in zebrafish. *Nat Commun*. 2022;13(1):13. doi:10.1038/s41467-021-27594-w

232. Keuls RA, Oh YS, Patel I, Parchem RJ. Post-transcriptional regulation in cranial neural crest cells expands developmental potential. *Proc Natl Acad Sci*. 2023;120(6):e2212578120. doi:10.1073/pnas.2212578120

233. Bajpai R, Coppola G, Kaul M, et al. Molecular stages of rapid and uniform neuralization of human embryonic stem cells. *Cell Death Differ*. 2009;16(6):807-825. doi:10.1038/cdd.2009.18

234. Perrier AL, Tabar V, Barberi T, et al. Derivation of midbrain dopamine neurons from human embryonic stem cells. *Proc Natl Acad Sci*. 2004;101(34):12543-12548. doi:10.1073/pnas.0404700101

235. Lee G, Kim H, Elkabetz Y, et al. Isolation and directed differentiation of neural crest stem cells derived from human embryonic stem cells. *Nat Biotechnol*. 2007;25(12):1468-1475. doi:10.1038/nbt1365

236. Bajpai R, Chen DA, Rada-Iglesias A, et al. CHD7 cooperates with PBAF to control multipotent neural crest formation. *Nature*. 2010;463(7283):958-962. doi:10.1038/nature08733

237. Chambers SM, Fasano CA, Papapetrou EP, Tomishima M, Sadelain M, Studer L. Highly efficient neural conversion of human ES and iPS cells by dual inhibition of SMAD signaling. *Nat Biotechnol*. 2009;27(3):275-280. doi:10.1038/nbt.1529

238. Mica Y, Lee G, Chambers SM, Tomishima MJ, Studer L. Modeling neural crest induction, melanocyte specification, and disease-related pigmentation defects in hESCs and patient-specific iPSCs. *Cell Rep*. 2013;3(4):1140-1152. doi:10.1016/j.celrep.2013.03.025

239. Chambers SM, Mica Y, Lee G, Studer L, Tomishima MJ. Dual-SMAD Inhibition/WNT Activation-Based Methods to Induce Neural Crest and Derivatives from Human Pluripotent Stem Cells. In: Turksen K, ed. *Human Embryonic Stem Cell Protocols*. Methods in Molecular Biology. Springer; 2016:329-343. doi:10.1007/7651_2013_59

240. Fattahi F, Steinbeck JA, Kriks S, et al. Deriving human ENS lineages for cell therapy and drug discovery in Hirschsprung disease. *Nature*. 2016;531(7592):105-109. doi:10.1038/nature16951

241. Frith TJ, Granata I, Wind M, et al. Human axial progenitors generate trunk neural crest cells in vitro. White RM, Morrison SJ, eds. *eLife*. 2018;7:e35786. doi:10.7554/eLife.35786

242. Fan Y, Hackland J, Baggiolini A, et al. hPSC-derived sacral neural crest enables rescue in a severe model of Hirschsprung's disease. *Cell Stem Cell*. 2023;30(3):264-282.e9. doi:10.1016/j.stem.2023.02.003

243. Nakayama N, Pothiawala A, Lee JY, et al. Human pluripotent stem cell-derived chondroprogenitors for cartilage tissue engineering. *Cell Mol Life Sci*. 2020;77(13):2543-2563. doi:10.1007/s00018-019-03445-2

244. Kidwai F, Mui BWH, Arora D, et al. Lineage-specific differentiation of osteogenic progenitors from pluripotent stem cells reveals the FGF1-RUNX2 association in neural crest-derived osteoprogenitors. *Stem Cells Dayt Ohio*. 2020;38(9):1107-1123. doi:10.1002/stem.3206

245. Kirino K, Nakahata T, Taguchi T, Saito MK. Efficient derivation of sympathetic neurons from human pluripotent stem cells with a defined condition. *Sci Rep*. 2018;8(1):12865. doi:10.1038/s41598-018-31256-1

246. Umehara Y, Toyama S, Tominaga M, et al. Robust induction of neural crest cells to derive peripheral sensory neurons from human induced pluripotent stem cells. *Sci Rep*. 2020;10:4360. doi:10.1038/s41598-020-60036-z

247. Deng T, Jovanovic VM, Tristan CA, et al. Scalable generation of sensory neurons from human pluripotent stem cells. *Stem Cell Rep*. 2023;18(4):1030-1047. doi:10.1016/j.stemcr.2023.03.006

248. Majd H, Amin S, Ghazizadeh Z, et al. Deriving Schwann cells from hPSCs enables disease modeling and drug discovery for diabetic peripheral neuropathy. *Cell Stem Cell*. 2023;30(5):632-647.e10. doi:10.1016/j.stem.2023.04.006

249. Zhang Y, Hu S, Wang J, Xue Z, Wang C, Wang N. Dexamethasone inhibits SARS-CoV-2 spike pseudotyped virus viropexis by binding to ACE2. *Virology*. 2021;554:83-88. doi:10.1016/j.virol.2020.12.001

250. Lu J, Hou Y, Ge S, et al. Screened antipsychotic drugs inhibit SARS-CoV-2 binding with ACE2 in vitro. *Life Sci*. 2021;266:118889. doi:10.1016/j.lfs.2020.118889

251. Wang N, Han S, Liu R, et al. Chloroquine and hydroxychloroquine as ACE2 blockers to inhibit viropexis of 2019-nCoV Spike pseudotyped virus. *Phytomedicine*. 2020;79:153333. doi:10.1016/j.phymed.2020.153333

252. Samuel RM, Majd H, Richter MN, et al. Androgen Signaling Regulates SARS-CoV-2 Receptor Levels and Is Associated with Severe COVID-19 Symptoms in Men. *Cell Stem Cell*. 2020;27(6):876-889.e12. doi:10.1016/j.stem.2020.11.009

253. Fattahi F, Steinbeck JA, Kriks S, et al. Deriving human ENS lineages for cell therapy and drug discovery in Hirschsprung disease. *Nature*. 2016;531(7592):105-109. doi:10.1038/nature16951

254. Barber K, Studer L, Fattahi F. Derivation of enteric neuron lineages from human pluripotent stem cells. *Nat Protoc*. 2019;14(4):1261-1279. doi:10.1038/s41596-019-0141-y

255. Majd H, Samuel RM, Ramirez JT, et al. hPSC-Derived Enteric Ganglioids Model Human ENS Development and Function. Published online January 4, 2022:2022.01.04.474746. doi:10.1101/2022.01.04.474746

256. Richter MN, Farahvashi S, Samuel RM, et al. Inhibition of muscarinic receptor signaling protects human enteric inhibitory neurons against platin chemotherapy toxicity. Published online March 10, 2023:2023.03.08.531806. doi:10.1101/2023.03.08.531806

257. Rada-Iglesias A, Bajpai R, Prescott S, Brugmann SA, Swigut T, Wysocka J. Epigenomic Annotation of Enhancers Predicts Transcriptional Regulators of

Human Neural Crest. *Cell Stem Cell*. 2012;11(5):633-648. doi:10.1016/j.stem.2012.07.006

258. Dupin E, Real C, Glavieux-Pardanaud C, Vaigot P, Douarin NML. Reversal of developmental restrictions in neural crest lineages: Transition from Schwann cells to glial-melanocytic precursors in vitro. *Proc Natl Acad Sci*. 2003;100(9):5229-5233. doi:10.1073/pnas.0831229100

259. McKinney MC, Fukatsu K, Morrison J, McLennan R, Bronner ME, Kulesa PM. Evidence for dynamic rearrangements but lack of fate or position restrictions in premigratory avian trunk neural crest. *Dev Camb Engl*. 2013;140(4):820-830. doi:10.1242/dev.083725

260. Serbedzija GN, Fraser SE, Bronner-Fraser M. Pathways of trunk neural crest cell migration in the mouse embryo as revealed by vital dye labelling. *Dev Camb Engl*. 1990;108(4):605-612. doi:10.1242/dev.108.4.605

261. Krispin S, Nitzan E, Kalcheim C. The dorsal neural tube: A dynamic setting for cell fate decisions. *Dev Neurobiol*. 2010;70(12):796-812. doi:10.1002/dneu.20826

262. Harris ML, Erickson CA. Lineage specification in neural crest cell pathfinding. *Dev Dyn Off Publ Am Assoc Anat*. 2007;236(1):1-19. doi:10.1002/dvdy.20919

263. Mica Y, Lee G, Chambers SM, Tomishima MJ, Studer L. Modeling Neural Crest Induction, Melanocyte Specification, and Disease-Related Pigmentation Defects in hESCs and Patient-Specific iPSCs. *Cell Rep*. 2013;3(4):1140-1152. doi:10.1016/j.celrep.2013.03.025

264. Hackland JOS, Shelar PB, Sandhu N, et al. FGF Modulates the Axial Identity of Trunk hPSC-Derived Neural Crest but Not the Cranial-Trunk Decision. *Stem Cell Rep*. 2019;12(5):920-933. doi:10.1016/j.stemcr.2019.04.015

265. Groves AK, LaBonne C. Setting appropriate boundaries: Fate, patterning and competence at the neural plate border. *Dev Biol*. 2014;389(1):2-12. doi:10.1016/j.ydbio.2013.11.027

266. Jin S, Guerrero-Juarez CF, Zhang L, et al. Inference and analysis of cell-cell communication using CellChat. *Nat Commun*. 2021;12(1):1088. doi:10.1038/s41467-021-21246-9

267. Wu Y, Tamayo P, Zhang K. Visualizing and Interpreting Single-Cell Gene Expression Datasets with Similarity Weighted Nonnegative Embedding. *Cell Syst*. 2018;7(6):656-666.e4. doi:10.1016/j.cels.2018.10.015

268. Aibar S, González-Blas CB, Moerman T, et al. SCENIC: single-cell regulatory network inference and clustering. *Nat Methods*. 2017;14(11):1083-1086. doi:10.1038/nmeth.4463

269. Buac K, Xu M, Cronin J, Weeraratna AT, Hewitt SM, Pavan WJ. NRG1 / ERBB3 signaling in melanocyte development and melanoma: inhibition of differentiation and promotion of proliferation. *Pigment Cell Melanoma Res*. 2009;22(6):773-784. doi:10.1111/j.1755-148X.2009.00616.x

270. Trapnell C, Cacchiarelli D, Grimsby J, et al. The dynamics and regulators of cell fate decisions are revealed by pseudotemporal ordering of single cells. *Nat Biotechnol*. 2014;32(4):381-386. doi:10.1038/nbt.2859

271. Qiu X, Mao Q, Tang Y, et al. Reversed graph embedding resolves complex single-cell trajectories. *Nat Methods*. 2017;14(10):979-982. doi:10.1038/nmeth.4402

272. Cao J, Spielmann M, Qiu X, et al. The single-cell transcriptional landscape of mammalian organogenesis. *Nature*. 2019;566(7745):496-502. doi:10.1038/s41586-019-0969-x

273. Callahan SJ, Mica Y, Studer L. Feeder-free Derivation of Melanocytes from Human Pluripotent Stem Cells. *J Vis Exp JoVE*. 2016;(109):e53806. doi:10.3791/53806

274. Solé-Boldo L, Raddatz G, Schütz S, et al. Single-cell transcriptomes of the human skin reveal age-related loss of fibroblast priming. *Commun Biol*. 2020;3(1):188. doi:10.1038/s42003-020-0922-4

275. Rindler K, Krausgruber T, Thaler FM, et al. Spontaneously Resolved Atopic Dermatitis Shows Melanocyte and Immune Cell Activation Distinct From Healthy Control Skin. *Front Immunol*. 2021;12:630892. doi:10.3389/fimmu.2021.630892

276. Cheng JB, Sedgewick AJ, Finnegan AI, et al. Transcriptional Programming of Normal and Inflamed Human Epidermis at Single-Cell Resolution. *Cell Rep*. 2018;25(4):871-883. doi:10.1016/j.celrep.2018.09.006

277. He H, Suryawanshi H, Morozov P, et al. Single-cell transcriptome analysis of human skin identifies novel fibroblast subpopulation and enrichment of immune subsets in atopic dermatitis. *J Allergy Clin Immunol*. 2020;145(6):1615-1628. doi:10.1016/j.jaci.2020.01.042

278. Reynolds G, Vegh P, Fletcher J, et al. Developmental cell programs are co-opted in inflammatory skin disease. *Science*. 2021;371(6527):eaba6500. doi:10.1126/science.aba6500

279. Popescu DM, Botting RA, Stephenson E, et al. Decoding human fetal liver haematopoiesis. *Nature*. 2019;574(7778):365-371. doi:10.1038/s41586-019-1652-y

280. Hughes TK, Wadsworth MH, Gierahn TM, et al. Second-Strand Synthesis-Based Massively Parallel scRNA-Seq Reveals Cellular States and Molecular Features of Human Inflammatory Skin Pathologies. *Immunity*. 2020;53(4):878-894.e7. doi:10.1016/j.immuni.2020.09.015

281. Replogle JM, Bonnar JL, Pogson AN, et al. Maximizing CRISPRi efficacy and accessibility with dual-sgRNA libraries and optimal effectors. Carette JE, Stainier DY, Calabrese M, eds. *eLife*. 2022;11:e81856. doi:10.7554/eLife.81856

282. Uhlen M, Zhang C, Lee S, et al. A pathology atlas of the human cancer transcriptome. *Science*. 2017;357(6352):eaan2507. doi:10.1126/science.aan2507

283. Rivero S, Ceballos-Chávez M, Bhattacharya SS, Reyes JC. HMG20A is required for SNAI1-mediated epithelial to mesenchymal transition. *Oncogene*. 2015;34(41):5264-5276. doi:10.1038/onc.2014.446

284. Lee M, Daniels MJ, Garnett MJ, Venkitaraman AR. A mitotic function for the high-mobility group protein HMG20b regulated by its interaction with the BRC repeats of the BRCA2 tumor suppressor. *Oncogene*. 2011;30(30):3360-3369. doi:10.1038/onc.2011.55

285. Al-Yhya N, Khan MF, Almeer RS, Alshehri MM, Aldughaim MS, Wadaan MA. Pharmacological inhibition of HDAC1/3-interacting proteins induced morphological changes, and hindered the cell proliferation and migration of hepatocellular carcinoma cells. *Environ Sci Pollut Res Int*. 2021;28(35):49000-49013. doi:10.1007/s11356-021-13668-1

286. Savci-Heijink CD, Halfwerk H, Koster J, Van de Vijver MJ. Association between gene expression profile of the primary tumor and chemotherapy response of metastatic breast cancer. *BMC Cancer*. 2017;17(1):755. doi:10.1186/s12885-017-3691-9

287. Wang T, Zhang Y, Bai J, Xue Y, Peng Q. MMP1 and MMP9 are potential prognostic biomarkers and targets for uveal melanoma. *BMC Cancer*. 2021;21(1):1068. doi:10.1186/s12885-021-08788-3

288. Gonzalez-Avila G, Sommer B, Mendoza-Posada DA, Ramos C, Garcia-Hernandez AA, Falfan-Valencia R. Matrix metalloproteinases participation in the metastatic process and their diagnostic and therapeutic applications in cancer. *Crit Rev Oncol Hematol*. 2019;137:57-83. doi:10.1016/j.critrevonc.2019.02.010

289. Gobin E, Bagwell K, Wagner J, et al. A pan-cancer perspective of matrix metalloproteases (MMP) gene expression profile and their diagnostic/prognostic potential. *BMC Cancer*. 2019;19(1):581. doi:10.1186/s12885-019-5768-0

290. Napoli S, Scuderi C, Gattuso G, et al. Functional Roles of Matrix Metalloproteinases and Their Inhibitors in Melanoma. *Cells*. 2020;9(5):1151. doi:10.3390/cells9051151

291. Correa BR, de Araujo PR, Qiao M, et al. Functional genomics analyses of RNA-binding proteins reveal the splicing regulator SNRPB as an oncogenic candidate in glioblastoma. *Genome Biol*. 2016;17(1):125. doi:10.1186/s13059-016-0990-4

292. Zhu L, Zhang X, Sun Z. SNRPB promotes cervical cancer progression through repressing p53 expression. *Biomed Pharmacother Biomedecine Pharmacother*. 2020;125:109948. doi:10.1016/j.biopha.2020.109948

293. Liu N, Wu Z, Chen A, et al. SNRPB promotes the tumorigenic potential of NSCLC in part by regulating RAB26. *Cell Death Dis*. 2019;10(9):667. doi:10.1038/s41419-019-1929-y

294. Cichorek M, Wachulska M, Stasiewicz A, Tymińska A. Skin melanocytes: biology and development. *Postepy Dermatol Alergol*. 2013;30(1):30-41. doi:10.5114/pdia.2013.33376

295. Horlbeck MA, Gilbert LA, Villalta JE, et al. Compact and highly active next-generation libraries for CRISPR-mediated gene repression and activation. *eLife*. 2016;5:e19760. doi:10.7554/eLife.19760

296. Vieth B, Parekh S, Ziegenhain C, Enard W, Hellmann I. A systematic evaluation of single cell RNA-seq analysis pipelines. *Nat Commun*. 2019;10(1):4667. doi:10.1038/s41467-019-12266-7

297. Linderman GC, Zhao J, Kluger Y. *Zero-Preserving Imputation of ScRNA-Seq Data Using Low-Rank Approximation*.; 2018:397588. doi:10.1101/397588

298. Harris ML, Hall R, Erickson CA. Directing pathfinding along the dorsolateral path - the role of EDNRB2 and EphB2 in overcoming inhibition. *Development*. 2008;135(24):4113-4122. doi:10.1242/dev.023119

299. Dzwonek J, Wilczynski GM. CD44: molecular interactions, signaling and functions in the nervous system. *Front Cell Neurosci*. 2015;9:175. doi:10.3389/fncel.2015.00175

300. Ma FC, He RQ, Lin P, et al. Profiling of prognostic alternative splicing in melanoma. *Oncol Lett*. 2019;18(2):1081-1088. doi:10.3892/ol.2019.10453

301. Wan Q, Sang X, Jin L, Wang Z. Alternative Splicing Events as Indicators for the Prognosis of Uveal Melanoma. *Genes*. 2020;11(2):227. doi:10.3390/genes11020227

302. Beattie R, Hippenmeyer S. Mechanisms of radial glia progenitor cell lineage progression. *Febs Lett*. 2017;591(24):3993-4008. doi:10.1002/1873-3468.12906

Publishing Agreement

It is the policy of the University to encourage open access and broad distribution of all theses, dissertations, and manuscripts. The Graduate Division will facilitate the distribution of UCSF theses, dissertations, and manuscripts to the UCSF Library for open access and distribution. UCSF will make such theses, dissertations, and manuscripts accessible to the public and will take reasonable steps to preserve these works in perpetuity.

I hereby grant the non-exclusive, perpetual right to The Regents of the University of California to reproduce, publicly display, distribute, preserve, and publish copies of my thesis, dissertation, or manuscript in any form or media, now existing or later derived, including access online for teaching, research, and public service purposes.

DocuSigned by:
Ryan Samuel
DBC84296CB884FF...
Author Signature

5/24/2023
Date